UNIVERSITÀ DELLA CALABRIA
Dipartimento di Chimica

School "BERNARDINO TELESIO"
Department of Chemistry
Department of Physics

Dipartimento di Chimica – Facoltà di Scienze Matematiche Fisiche e Naturali

Bernardino Telesio – Scuola di Dottorato di Scienza e Tecnica

Curriculum: Mesofasi e Materiali Molecolari

Settore disciplinare: CHIM02

XXIV ciclo

Shear-induced structural transformations in surfactant systems

Supervisore
Dr. Cesare Oliviero Rossi

Coordinatore
Prof. Carlo Versace

Direttore
Prof. Roberto Bartolino

Candidato
Luigi Gentile

Anno Accademico 2010/2011

PREFAZIONE

La seguente tesi di dottorato è focalizzata sulla formazione di strutture indotte da deformazione meccanica. Le trasformazioni indotte, infatti, sono di grande interesse sia per il mondo scientifico che per quello industriale. Nei processi industriali la formazione di nuove strutture sotto flusso riveste importanza non solo per il cambio di parametri chimico-fisici o in generale di parametri macroscopici (quale ad esempio la vistosità), ma soprattutto perché tali cambiamenti determinano di fatto le proprietà del prodotto finale. Nel campo scientifico l'interesse è rivolto alla comprensione della morfologia delle neostrutture formatesi ed ai meccanismi che governano tali trasformazioni.

La caratterizzazione delle strutture indotte da deformazioni riveste nel mondo dei colloidi un ruolo centrale. Questo è dovuto alla complessità delle trasformazioni ed al vasto impiego di queste strutture nelle diverse discipline scientifiche. Di particolare interesse è la comprensione della formazione di sistemi vescicolari da fasi lamellari classiche. Lo studio di queste nano-strutture necessita l'utilizzo di diverse tecniche chimico fisiche d'avanguardia che spesso devono essere implementate per ottenere le informazioni strutturali sotto flusso di deformazione. Le principali tecniche utilizzate sono state la Risonanza Magnetica Nucleare e lo Scattering Neutronico e in Luce visibile, equipaggiate con accessorio reologico.

In questo studio sono stati analizzati diversi sistemi liotropici la maggior parte dei quali costituiti dalla categoria di tensioattivi non-ionici a base ossido di etilene. Dunque è stato possibile correlare la formazione di vescicole multi-lamellari con i parametri strutturali delle lamelle planari. Durante queste investigazioni sono state evidenziate oscillazioni strutturali stazionarie e fenomeni di shear banding. La correlazione tra le proprietà reologiche (viscosità) e i cambi strutturali in flusso solo un elemento di novità nella scienza dei colloidi.

UNIVERSITÀ DELLA CALABRIA
Dipartimento di Chimica

School "BERNARDINO TELESIO"
Department of Chemistry
Department of Physics

Bernardino Telesio - Doctorate School of Science and Technique

Curriculum: Mesophases and Molecular Materials - CHIM02

XXIV cycle

Shear-induced structural transformations in surfactant systems

Submitted in partial fulfilment of the requirements for the Degree of Doctor of Philosophy in Science and Technique.

Supervisor
Dr. Cesare Oliviero Rossi

Coordinator
Prof. Carlo Versace

Chairman
Prof. Roberto Bartolino

Candidate
Luigi Gentile

Academic Year 2010/2011

Shear-induced structural transformations in surfactant systems

Luigi Gentile

PhD Dissertation

Laboratory: “PC_SM Mario Terenzi”
Department of Chemistry
University of Calabria
Via P. Bucci, 12C
87036 – Rende (CS)
Italy

ABSTRACT

The present doctoral thesis deals with structural transformations of mesophases subjected to shear flow. Multilamellar vesicles are closed concentric bilayer structures that can appear when planar lamellae are under shear flow. The lamellar-to-multilamellar vesicle transformation was observed in ionic (ammonium perfluorononanoate) and nonionic (poly-oxy-ethylene ethers) surfactant/water systems. Additionally the lamellar-to-sponge phase transition and its reverse have been studied. On the other hand this work also investigates flow instabilities, since they are related to shear induced structures.

Rheology, rheo-Nuclear Magnetic Resonance, rheo-Small Angle Light Scattering and rheo-Small Angle Neutron Scattering were used to investigate the systems. The transitions have been followed by time resolved experiments.

LIST OF PAPERS

1. Gentile, L.; Oliviero Rossi, C.; Olsson, U. Rheological and rheo-SALS investigation of the multi-lamellar vesicle formation in the $C_{12}E_3/D_2O$ system. *J. Colloid Interface Sci.* **2011**, doi:10.1016/j.jcis.2011.10.057.

2. Gentile, L.; Oliviero Rossi, C.; Olsson, U.; Ranieri, G. A. Effect of Shear Rates on the MLV Formation and MLV Stability Region in the $C_{12}E_5/D_2O$ System: Rheology and Rheo-NMR and Rheo-SANS Experiments. *Langmuir* **2011**, *27*, 2088-2092.

3. Gentile, L.; Mortensen, K.; Oliviero Rossi, C.; Olsson, U.; Ranieri, G. A. Multi-lamellar vesicle formation in a long-chain nonionic surfactant: $C_{16}E_4/D_2O$ system. *J. Colloid Interface Sci.* **2011**, *362*, 1-4.

4. Gentile, L.; Silva, B.F.B.; Balog, S.; Mortensen, K.; Olsson, U. Structural Transitions Induced by Shear Flow and Temperature variation in a Nonionic Surfactant/Water System submitted to *J. Colloid Interface Sci.*

5. Coppola, L.; Gentile, L.; Nicotera, I.; Oliviero Rossi, C.; Ranieri, G. A. Evidence of Formation of Ammonium Perfluorononanoate/^2H_2O Multilamellar Vesicles: Morphological Analysis by Rheology and Rheo-^{2}H NMR Experiments. *Langmuir* **2010**, *26*, 19060-19065.

Papers not included in this thesis

6. Antunes, F.; Gentile, L.; Tavano, L.; Oliviero Rossi, C. Rheological characterization of the thermal gelation of poly(N-isopropylacrylamide) and poly(N-isopropylacrylamide) co-Acrylic Acid. *Applied Rheology* **2009**, *19*, 42064-42069.

7. Youssry, M.; Asaro, F.; Coppola, L.; Gentile, L.; Nicotera, I. Solution microstructures of the micellar phase of Pluronic L64/SDS/water system. *J. Colloid Interface Sci.* **2010**, *342*, 348-353.

8. Antunes, F.; Gentile, L.; Oliviero Rossi, C.; Tavano, L.; , Ranieri, G. A. Gels of Pluronic F127 and nonionic surfactants from rheological characterization to controlled drug permeation. *Colloids and Surfaces B* **2011**, *87*, 42-48.

9. Gentile, L.; De Luca, G.; Antunes, F.; Oliviero Rossi, C.; Ranieri, G. A. Thermogelation Analysis Of F127-Water Mixtures By Physical Chemistry Techniques. *Applied Rheology* **2010**, *20*, 52081-52089.

10. Coppola, L.; Youssry, M.; Nicotera, I.; Gentile, L. Rheological investigation of thermal transitions in vesicular dispersion. *J. Colloid Interface Sci.* **2009**, *338*, 550-557.

CONTENTS

1 INTRODUCTION

Shear-induced transformations and ordering in complex fluids are interesting and important topics in science. The influence of shear on the structure of complex fluids has attracted a lot of interest [1-38, 63-89].

The general aim of this thesis is to investigate the structural changes of mesophases under shear flow. In particular one of the issues of this doctoral thesis is the shear-induced lamellar-to-MLV transition. Multilamellar vesicles (MLV), closed concentric bilayer structures, which can appear when lamellar phases are under shear [3-10], can be useful to encapsulate drugs, proteins and DNA or for other applications [11]. Although steady state structures of the lamellar phase under shear are very well characterized [12, 13], and despite the large number of studies in this field, the morphological lamellar–to–MLV dynamic transition under shear is not fully understood. There are two main lines of research going on: (1) understanding the details of MLV mechanism formation; (2) discovering new MLV phases induced by shear.

Another important issue is the viscosity oscillations under shear flow. The oscillations in the viscosity are usually associated with the formation of shear-induced structures in the form of highly birefringent state of the material and they are named as shear bands [14-24]. These shear bands are observed in both the dilute and semidilute concentration regime of the surfactant solutions and are characterized by means of different experimental techniques like, direct flow visualization [24, 25], ultrasound velocimetry [26], NMR velocimetry [27, 30], flow birefringence [31, 32], and scattering techniques like small angle light and neutron scattering [33-36]. We investigated viscosity oscillations in a surfactant concentrated system. The viscosity oscillation is not a common phenomenon, particularly for concentrated systems.

Moreover we studied the mechanical instability in a wormlike micellar system based on lecithin. This purely mechanical instability is responsible for shear banding in semi-dilute solutions of wormlike micelles. In more concentrated systems the appearance of a banded flow is related to a first-order phase transition induced by the flow, such as an isotropic-to-nematic transition [37]. The wormlike micelles have a complex rheological behavior like

shear banding and chaotic response, which are connected to the thinning behaviour of these systems [38]. It is therefore important to understand the microscopic mechanism underlying the very strong shear-thinning behaviour of wormlike micelles.

The present PhD-thesis focused mainly on non-ionic surfactant systems C_nE_m such as: Triethylene glycol monododecyl ether ($C_{12}E_3$)/^2H_2O; Pentaethylene glycol monododecyl ether ($C_{12}E_5$) /^2H_2O; Tetraethylene glycol monohexadecyl ether ($C_{16}E_4$)/^2H_2O. We also investigated the following systems: Ammonium Perfluorononanoate (APFN)/^2H_2O and Lecithin/Cyclohexane/H_2O.

The deep rheological analyses have been performed by means of strain and stress controlled instruments. ^2H Rheo-Nuclear Magnetic Resonance, Rheo-Small Neutron Angle Scattering and Rheo-Small Angle Light Scatterings have been used to investigate the MLV formation and the oscillations viscosity.

2 MATERIALS

2.1 SURFACTANTS

Surfactants are amphiphilic molecules consisting of a hydrophilic polar head group and a hydrophobic nonpolar tail. The word amphiphilic has a Greek origin, where amphi means both. Surfactants can be divided into four classes, depending on the nature of the head group. These classes of surfactants are: nonionic, cationic, anionic and zwitterionic. The hydrophobic tail normally consists of hydrocarbon chains.

The significance of the increased knowledge of surfactants behavior and their self-assembly in solutions lies in their great potential applications, as a component in detergents, emulsifiers, foaming agents, anti-foaming agents, cosmetics and in drug delivery systems. They are also useful to understand many processes, naturally occurring in all living organism, for instance, cell membrane fusion [39]. They are used in detergents and soaps because the hydrophobic part binds the dirt and the hydrophilic part makes it possible to rinse with water [40]. A well-known group of surfactants are biological lipids (phospholipids and others) that are present in all living organisms. They are the main component of all biological membranes, from cell walls to the membranes of many important organelles.

Several surfactants when dissolved in a specific solvent may self-assembly to form lyotropic liquid crystals, due to their amphiphilic behavior.

2.1.1 SELF-ASSEMBLY AND HYDROPHOBIC EFFECT

The molecular self-assembly is a fascinating and fundamental prerequisite of life and the basis of many applications. Although at low surfactant concentration the molecules are arranged at the air-water interface and dissolved as unimers in the bulk, at higher concentrations the surfactants start to self-associate. This is due to the hydrophobic tendency to avoid water-exposure, minimizing the energy cost of hydrophobic hydration. Any

amphiphilic molecule has a natural tendency to aggregate in aqueous solution [40]. This phenomenon is explained by the "hydrophobic effect", described by Hartley [41] and Tanford [40]. They stated that the process is entropically driven: the free energy of transfer of a non-polar compound from some reference state, such as a polymer aliphatic chain or surfactant tail, into water, dG_{trans}, is given by an enthalpy, dH, and an entropy, $-TdS$, term.

$$dG_{trans} = dH - TdS \qquad (2.1.1)$$

At room temperature, the interaction enthalpies are practically negligible. The entropy, however, is negative. Pure water molecules adopt a structure which maximizes entropy. A hydrophobic molecule will disrupt this structure and decrease entropy, to create a "cavity" as it is unable to interact electrostatically with the water molecules. When more than one "cavity" is present, the surface area of disruptions is large, meaning that there are fewer free water molecules. To maximize the amount of free water and thus the entropy, the water molecules push the hydrophobic molecules together and form a "cage" structure around them which will have a smaller surface area than the total surface area of the cavities [42]. The concentration for the onset of self-assembly is well defined and the first surfactant aggregates are called micelles. Micelles are approximately spherical in shape; in aqueous solutions the hydrophobic tails are situated inside the aggregate and the headgroup points towards the water. Micelles start to form at the Critical Micelle Concentration, denoted as CMC. Above the CMC, the number of micelles increases, while the concentration of free surfactant molecules is constant. The CMC is an important characteristic of a surfactant and has extremely practical importance. At the CMC, many chemical-physics properties show a marked change: (1) the surface tension of aqueous solution decreases with surfactant concentration and abruptly breaks above the CMC; (2) the turbidity increases strongly above the CMC.

The CMC is influenced by many factors, such as the chemical structure of the surfactant, temperature and addition of co-solutes [43]. CMC decreases strongly with increasing alkyl chain length of the surfactant. Non-ionic surfactants show much lower CMC than ionics (typically 2 orders of magnitude), due to lower electrostatic repulsion of the non-ionic headgroups. The increase of the non-ionics headgroup size makes the CMC higher.

Cationics typically have slightly higher CMCs than anionics. Counterion valency is also significant; substitution of a monovalent by a divalent counterion reduces the CMC by a factor of 4. Pressure has no important influence on the CMC, even up to high values. Addition of cosolutes also has effects on CMC. Addition of 1:1 inert electrolyte to an ionic monovalent surfactant solution leads to a dramatic lowering of the CMC (around 1 order of magnitude). On the other hand non-ionic surfactants are not importantly affected by salt addition [43]. The effects of the temperature on the CMC have been found to be quite complex. Nonionic and zwitterionic surfactants are not quite so predictable [44].

Surfactant molecules in water, form organized structures of various shapes, whose topology cannot be explained by the only hydrophobic effect. Therefore, the determination of aggregate shapes is mainly governed by headgroup repulsion, molecule geometry and system variables, such as the surfactant concentration, temperature and the eventual presence of salts. For a given molecular shape there should be an optimal aggregate structure, i.e, an aggregate topology leading to a minimization of the free-energy per surfactant molecule. The geometry of the surfactant, or critical packing parameter (CPP), is defined by [45]:

$$CPP = \frac{v}{l_c a_0} \tag{2.1.2}$$

where ν and l_c are the volume and length of the hydrocarbon chain, respectively, and a_0 is the optimal area occupied by the headgroup in the polar/nonpolar interface, and depends on both electrolyte and surfactant concentration. The volume parameter, ν, (in nm^3) is given by

$$v \approx 0.029 + 0.027 n_c \tag{2.1.3}$$

where n_c is the number of carbon atoms in the chain. The length of the alkyl chain (in nm) is

$$l_c \approx 0.154 + 0.127 n_c \tag{2.1.4}$$

A small value of CPP means that the head group is large and the preferred aggregates are highly curved (spherical micelles). A relatively high value of CPP means that the aggregates go from spheres to rod-like micelles

and to vesicular or lamellar structures. At even higher CPP (>1), reversed structures take place, Figure 2.1.1. CPP contributes to expect the trend in aggregation behavior. It is still helpful when factors as surfactant concentration, ionic strength, temperature, pH, addition of cosolutes vary. This is because these parameters directly affect the optimal headgroup area or the volume of the hydrocarbon chain.

The concept of mean curvature of the surfactant film, H, is an alternative way to evaluate surfactant aggregate shape. A mean curvature H on a surface is defined as:

$$H = \frac{1}{2}\left(\frac{1}{R_1} + \frac{1}{R_2}\right) \qquad (2.1.5)$$

where R_1 and R_2 are the radii of curvature in two perpendicular directions. For a spherical micelle, $R_1 = R_2 = R$ and $H = 1/R$ while for a planar bilayer, $H = 0$. For reversed structures, H is negative.

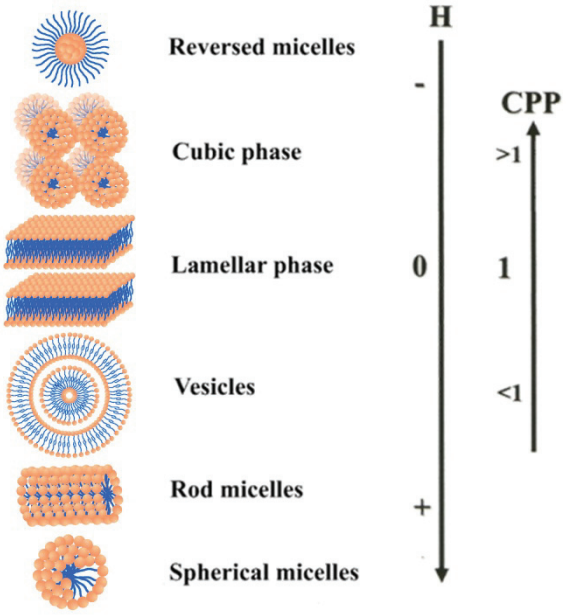

Figure 2.1.1: Dependence of surfactant aggregate type with CPP and H.

According to Eq. 2.1.2 an infinite number of phases is possible due to a continuously variable ratio on the Tanford's hypothesis. However, the maximum number of canonic phases is 9. There are several commonly used classifications based on empirical, structural or other considerations [46]. Table 2.1.1 shows the Tiddy's classification [47].

Phase Names	Symbol	Characteristics
Micellar	L_1	isotropic solution
Nematic	N	anisotropic (uniaxial)
Cubic (spheroid)	I_1	isotropic
Hexagonal	H_1	anisotropic
Cubic (ellipsoid)	V_1	isotropic
Lamellar	L_α	anisotropic
Cubic (discoid)	V_2	isotropic
Inverse Hexagonal	H_2	anisotropic
Cubic (inverse spheroid)	I_2	isotropic
Inverse micellar	L_2	isotropic solution
Sponge	L_3	isotropic

Table 2.1.1: Phase names and relative symbols using the Tiddy's classification. Moreover two isotropic micellar solutions are listed.

In 1967 Lawson and Flautt [48] described the first lyotropic nematic liquid crystal phase. The nematic phase have been identified as uniaxial. The first biaxial nematic has been observed by Photinos, Yu and Saupe [49] in a ternary mixture of potassium laureate, decanol and water. The mixture decylammoniumchloride/ammoniumchloride/water which presents a phase described as having disk-like micelles with uniaxial symmetry, N_D [49].

In a lamellar phase the amphiphilic molecules are arranged in bilayers separated by water layers, Figure 2.1.2. The layers extend over large distances, usually of the order of microns or more. Usually, the thickness of the layers (δ) is about twice the length of the main amphiphilic molecule. However, this δ can increase due to the addition of a non-polar solvent. The thickness also depends on the temperature of the sample [50]. The length of a carbon chain in a trans configuration (unfolded state) can be obtained from the empirical Eq. 2.1.4. If the layers are flat and the paraffinic chains are in a liquid-like state, the phase is called L_α. Usually, lamellar mesophases only exist below 50 wt% of surfactant. When the surfactant is above 50 wt%, transition from lamellar to hexagonal phase (H) or an isotropic micellar solution may occur. However, in certain particular cases, lyotropic lamellar phase is exhibited in

extremely dilute solutions. The interlamellar spacing distance (d) depends on the surfactant concentration.

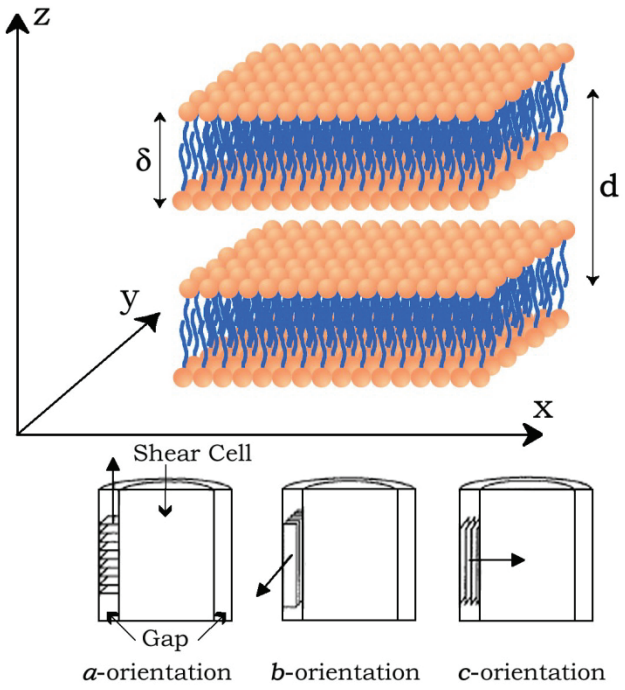

Figure 2.1.2: Schematic representation of a lamellar phase, d represents the interlamellar spacing and δ is the membrane thickness. Considering the L_α inside a shear cell, the "y" direction corresponds to the velocity gradient, while shear flow and vorticity directions are respectively x and z axis.

In lamellar phases the parallel layers slide may easily orient during the shear flow and hence lamellar phases are less viscous than the hexagonal lyotropic phases. In order to classify the different orientations under shear of the lamellar phase, it is possible to use the notation "*a*", "*b*" and "*c*". This notation is referred to the orientation of the director (or layer normal) respect to the shear frame as reported by reference [51], Figure 2.1.2. If the normal of the lamellar phase is parallel to the vorticity direction (or neutral), the orientation is denoted with "*a*"; when the normal is parallel to the shear flow direction, we have the *b*-orientation; when the normal is parallel to velocity gradient, we have the *c*-orientation.

When the micelles form cylindrical aggregates arranged on a long-ranged hexagonal lattice, the lyotropic liquid crystalline phase is known as the 'hexagonal phase'. Cubic arrangement of molecular aggregates is the characteristic of the well-known cubic phase. The cubic phases are extremely viscous; even more viscous than hexagonal phases. They are optical isotropic and so are often called the viscous isotropic phases.

The Sponge phase (L_3) is optical isotropic and shows no sign of long range positional order. Experimental investigations by means of scattering techniques [52] have shown that L_3 phase has a bicontinuous structure, where an amphiphilic membrane separates the three-dimensional space in two connected solvent domains, resembling the topological structure of a sponge [53]. From a microscopic point of view, the sponge phase sets in when the spontaneous curvature of the amphiphilic interface is progressively reduced from positive (corresponding to micellar solution) to zero (corresponding to the L_α phase) to slightly negative.

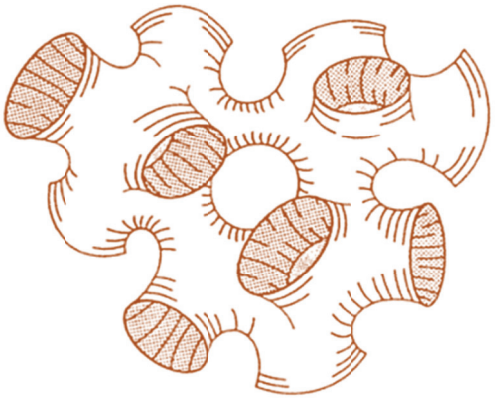

Figure 2.1.3: Schematic representation of a sponge phase [53].

2.2 THE CURVATURE FREE ENERGY CONCEPT

The Helfrich curvature free energy concept [54] has proven to be very useful to describe the free energy of an aggregate and the change of the energy when one aggregate structure transforms into another. The curvature free energy concept is also known as the flexible surface model [54]. The surface of an aggregate, that is, its bilayer or monolayer, is considered as a geometrical surface. For each configuration of the surface, a local curvature free energy density, g_c, is defined as the energy in each point on the surface [55];

$$g_c = 2\kappa\left(H - H_0\right)^2 + \bar{\kappa}K \tag{2.2.1}$$

where κ is the bending rigidity, $\bar{\kappa}$ is the saddle-splay modulus, H and H_0 are the mean and spontaneous curvature, respectively, and $K=1/(R_1R_2)$ is the Gaussian curvature. The total curvature free energy is then obtained by integration of the local curvature free energy density, g_c, over the whole area of the aggregate.

$$G_c = \int \mathrm{g_c}\, dA \tag{2.2.2}$$

The bending rigidity κ is a quantity that describes how much energy we have to use to bend a surfactant film. The typical values lie between 1 and 20 k_bT. Parameters that increase the flexibility of the film include for example shorter chains, large number of unsaturated bonds with cis configuration in the hydrocarbon tail, two tails with unequal chains, presence of surfactants and higher oil penetration. The saddle-splay modulus describes the preferred topology of the surfactant film.

Two main structural properties influence dramatically the bending rigidity κ in the model of Würger [56]: the hydrophobic chain and the polar head surface area of the surfactant. κ is expressed by

$$\kappa = \left(k_BT\right)\left\{\frac{(id_m)^2}{a} + \frac{(id_m)^3}{24ad_m}\frac{\varepsilon}{k_BT}\left[\left(\frac{\rho_0}{\sigma}\right)^2 - 1\right]^{-1} \cdot \left[\frac{156}{5}\left(1 - \left(\frac{\sigma}{\rho_0}\right)^{10}\right) - 42\left(1 - \left(\frac{\sigma}{\rho_0}\right)^4\right)\right]\right\} \tag{2.2.3}$$

where d_m is the length of a methyl group (1.27 Å), i is the number of methyl groups; a = (2M)/(ρδ) where M is the molecular weight, ρ the surfactant density and δ is the membrane thickness; $\rho_0^2 = (2/\sqrt{3})a$ is the neighbor distance between surfactants. ε and σ are the Lennard-Jones parameters of a surfactant methyl group that are, ε = 4.3 meV and σ = 3.9 Å [57].

For nonionic surfactants, the surface curvature properties are strongly dependent on temperature [58-61]. For instance, when temperature is increased, water becomes a worst solvent for polyoxyethylene headgroup. In this case, interactions between the headgroups are stronger than the attractive interactions between a headgroup and water, leading to the deswelling of the chains and curvature towards water. When the temperature is decreased, water becomes a better solvent for poly(oxy)ethylene headgroup, leading to the curvature towards oily part. This temperature dependence of the spontaneous curvature is described by

$$H_0(T) = \left.\frac{dH_0}{dT}\right|_{T_0} (T_0 - T) + \ldots = -\beta(T - T_0) \qquad (2.2.4)$$

where β is the system specific coefficient, independent from temperature, and T_0 is the phase inversion temperature (PIT or balance temperature) where the surfactant film neither prefers to curve towards water nor towards oil [62].

2.3 SHEAR-INDUCED STRUCTURES

The influence of shear flow on complex fluids has attracted considerable attention in the scientific literature [1-38, 63-67]. The study of the interrelation between flow and structure has received attention, because the organization of the complex fluids may be affected by the flow field. This, in turn, may alter their rheological properties. Structural changes induced by shear in supramolecular aggregates, have been reported in a number of self-assembled surfactant systems [1-38, 63-89]. While a decrease in viscosity (a shear-thinning phenomenon) can be simply achieved by the alignment of anisotropic particles in the flow direction, shear-thickening usually involves the formation of new structures (so called shear-induced structures). The different rheological behavior and the relative rheological terms are better explained in the Paragraph 3.1.

Surfactant lamellar phases have a wide range of flow induced behaviour including shear thickening [5, 90], shear thinning [1, 90], shear-induced structures [5, 67, 90] and shear-induced phase separation [5, 9, 90-92]. Usually, a defective lamellar phase aligns in the *c*-orientation at low shear stress. This orientation becomes unstable at higher shear stress and the membranes reorient to the *a*-orientation (see Figure 2.1.2). However, over a limited range of composition, at constant applied shear rate, the *c*-orientation lamellar organization undergoes a complex, thixotropic evolution. Indeed the lamellar phase “rolls” into a cylindrical morphology aligned along the flow direction (so-called multilamellar cylinders MLCs) [7, 9], which then further evolves, with increasing applied strain, into multilamellar vesicles MLVs or “onions". This is one of the most spectacular transitions, discovered for the first time by Diat and Roux [1, 67], Figure 2.3.1.

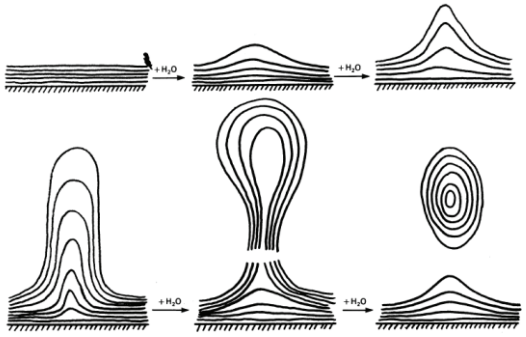

Figure 2.3.1: Scheme of MLV formation proposed by Diat [1].

In many surfactant systems (especially based on poly(oxy)ethylene ether) the shear-thickening phenomenon is due to the shear-induced formation of multilamellar vesicles (MLVs) from planar lamellae [6-9, 72-76].

Another effect of the flow on lyotropic phases can be the banding phenomenon. “Banded structures” of macroscopic dimensions can be induced by simple the shear flow in many different types of soft matter systems. Depending on whether these bands extend along the gradient or vorticity direction, the banding transition is referred to as “gradient banding” or “vorticity banding,” respectively. In case of gradient banding in a Couette cell, the stationary state is the one where two bands coexist, which extend in the gradient direction. A top view of such a banded state is schematically depicted in Figure 2.3.2, left figure.

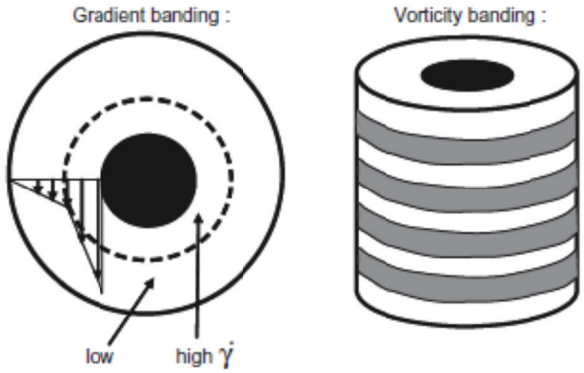

Figure 2.3.2: Schematic representation of gradient banding (left figure), where the inner cylinder is supposed to rotate, and vorticity banding (right figure) in a Couette geometry [86].

The shear rate within each of the two bands is spatially constant, and the two bands are connected by a sharp “interface.” In case of vorticity banding, regular bands are formed that are stacked in the vorticity direction, as depicted in Figure 2.3.2 (right). Depending on the system, these bands are visible because the two types of bands have a different turbidity or because they are both birefringent but with somewhat different orientations of their optical axes.

Gradient banding is sometimes observed in glassy- and gel-like systems, as well as in shear-thickening systems. Possible mechanisms that could be at the origin of gradient-band formation in such systems are discussed. Gradient banding can also occur in strongly entangled polymeric systems. The most intensely studied systems that exhibit gradient banding are worm-like micellar systems (WMs) [18, 19, 28, 30, 93-100].

Vorticity banding has been observed in surfactant systems forming multilamellar vesicles [81,83], crystallizing colloids [101], surfactant solutions 88, dispersions of semirigid, rod-like colloids [102, 103], and nanotube suspensions where flow-induced, highly elastic clusters are formed [104]. It should be mentioned that band formation in this case is not related to a Taylor–Couette instability, see Paragraph 3.1.6. Vorticity banding has been observed by Bonn et al. [105] for worm-like micellar systems (this system exhibits probably both gradient and vorticity banding).

2.4 NONIONIC C_NE_M SURFACTANTS

This thesis focuses on nonionic surfactant systems based on poly(oxy)ethylene ether. The polar head is made of oxy-ethylene segments and the tail of one hydrocarbon chain. The poly(oxy)ethylene ether based surfactants are often denoted as C_nE_m, where n in the number of carbon atoms in the hydrocarbon chain (tail) and m is the number of the oxy-ethylene segments.

Nonionic surfactants do not ionize in aqueous solution, because their hydrophilic group is of a nondissociable type, such as alcohol, phenol, ether, ester, or amide. A large portion of these nonionic surfactants are hydrophilic due to the presence of a polyethylene glycol chain, obtained by the polycondensation of ethylene oxide. They are called polyethoxylated nonionics. Generally, water becomes a worst solvent for a polyethylene oxide segments as temperature is increased. This is due to a dehydration of headgroup caused by change in conformation of polyethylene oxide chain [58]. Surface tension of a solution tends to decrease with decreasing the number of ethylene oxide segments.

Phase diagrams of C_nE_m nonionic surfactants present a great variety of structures, depending on temperature and concentration [106-110]. For concentrated surfactant solutions, in which bilayer phases are preferentially formed, two topologically different organizations of the bilayers are possible: the lamellar, or L_α and the “sponge”, or L_3 [111, 112]. Often the structure of the lamellar phase does not consist of stacks of planar layers but of spherulites or multilamellar vesicles (MLVs), which are referred to as onions and may be observed by optical microscopy [113].

A phase diagram shown in Figure 2.4.1 presents the general phase behavior [114, 115] of an arbitrary nonionic surfactant (C_nE_m) in water system, where the values on x-axis depend on the surfactant concentration. The solubility of poly(oxy)ethylene ether based surfactants depends both on the alkyl chain length and the number of the ethylene oxide segments. At low temperature, they are usually soluble in water. By increasing temperature, the solution becomes turbid (cloudy) and the temperature at which this occurs is denoted as the cloud point or lower consolute temperature or critical temperature T_c. The T_c is defined as the minimum of the cloud point curve and

is specific for every surfactant. In a homologous series, increase in polyethylene oxide chain length causes both an increase in T_c and the narrowing of the concentration range of the cloud point curve. Opposite is true for alkyl chain length (l); at a given polyethylene oxide chain length, the increasing of l makes T_c lowered and it widens out the concentration range. Above the critical point, a phase separation into a diluted and a concentrated micelle phase occurs [116]. These are denoted as $L_1' + L_1''$ in the phase diagram. This phase separation is due to change in the interactions between micelles, from repulsive to attractive interactions [117]. In the phase diagram, Figure 2.4.1, there are other common phases found in surfactant systems. At low temperatures and concentrations, a micelle phase, denoted by L_1, exists. Increasing concentration, birefrengent lamellar phase (L_α) is present. This phase consists of two dimensional sheets, built up of surfactant bilayers. Before lamellar phase, at slightly lower concentrations, micelles can pack in hexagonal or cubic lattice (denoted by hexagonal H_1, and cubic V_1 phase). At high concentration, inverted phases, such as inverted micelles (L_2) are present. At high temperatures, sponge or L_3 phase, made by interconnected bilayers exists.

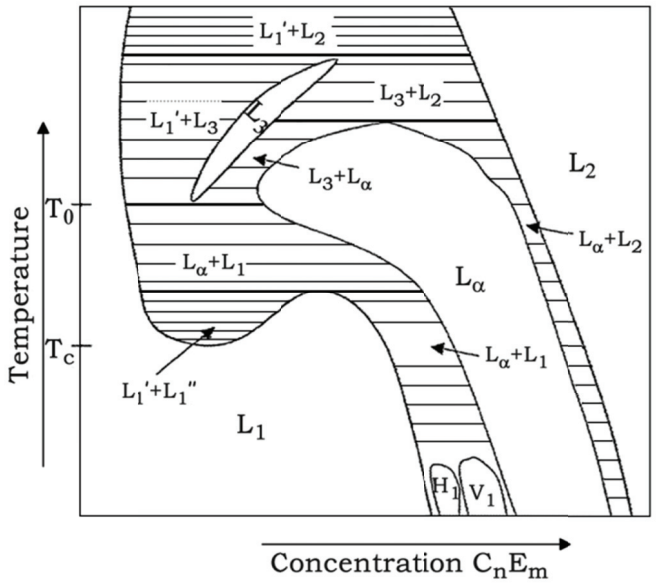

Figure 2.4.1: A general phase diagram for C_nE_m nonionic surfactants. (The symbols are listed in Table 1.1 with the corresponding phases).

2.4.1 $C_{12}E_3$/WATER SYSTEM

Ali and Mulley have reported [108], the phase diagram for dodecyl triethylene glycol ether ($C_{12}E_3$)-water system, over the range 20-33°C showing the W/L_α/L_2 phase sequence. Mitchel et al. [106] have shown that this sequence persists down to 0°C. Above ca. 33°C a narrow L_3 region occurs at the water-rich boundary of the L_α phase, so the sequence is L_1+L_3/L_3/L_α/L_2. The phase diagram reported in Figure 2.4.2 is adapted from the reference [107].

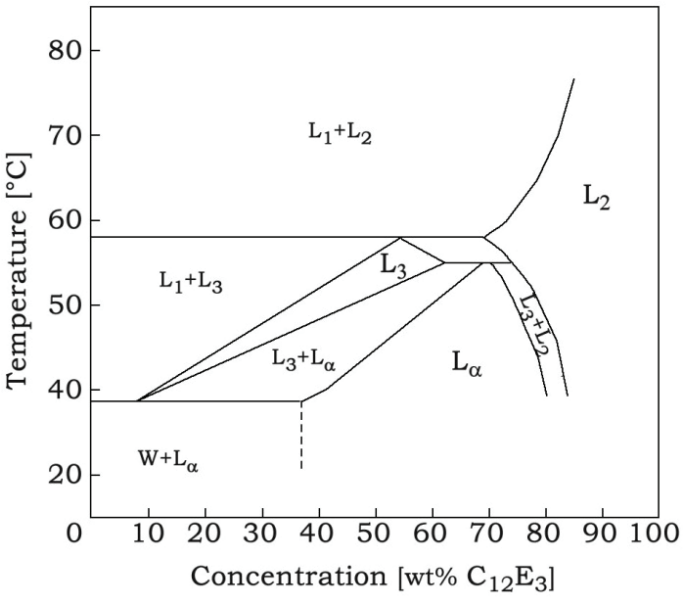

Figure 2.4.2: Phase diagram of the $C_{12}E_3$/water system over the temperature range 0-90°C, reproduced from reference [107].

2.4.2 $C_{12}E_5$/WATER SYSTEM

In the dodecyl pentaethylene glycol ether ($C_{12}E_5$)-water system [115] the cloud point is a function of surfactant concentration. At temperatures well above the cloud point, the L_α phase and also another liquid phase L_3, are seen in this system for relatively low surfactant concentrations. As the particles of a liquid crystal do not coalesce as readily as liquid drops, the dispersions of L_α are frequently less turbid than those of L_3. This property can be used to locate

phase transition temperatures [109]. The Figure 2.4.3 shows the phase diagram of the $C_{12}E_5$-water system [106].

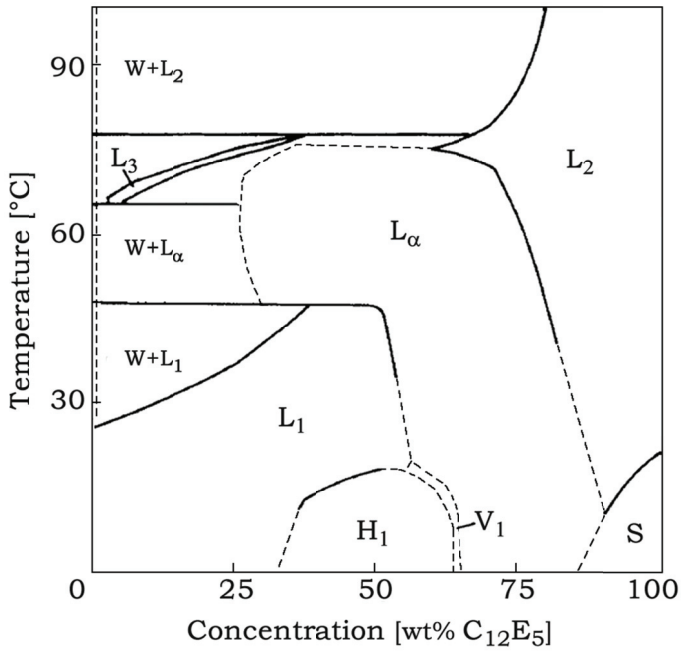

Figure 2.4.3: Phase diagram of the $C_{12}E_5$/water system over the temperature range 0-100°C, reproduced from reference [106] (S indicates the presence of solid surfactant).

2.4.3 $C_{16}E_4$/WATER SYSTEM

In hexadecyl tetraethylene glycol ether ($C_{16}E_4$)-water system the L_α phase shows a very complex behaviour, see Figure 2.4.4. A cubic region (V_2) in equilibrium with water is formed. Mitchel et al. [106] report two V_2 phases that are indicated by the observation of a refractive-index discontinuity within this region during a penetration experiment. At temperatures above the L_3 region, where V_2 + W co-existence occurs, water droplets form within the V_2 region. This is good evidence that the water-rich V_2 phase [118] has an extended structure, rather than consisting of discrete micelles.

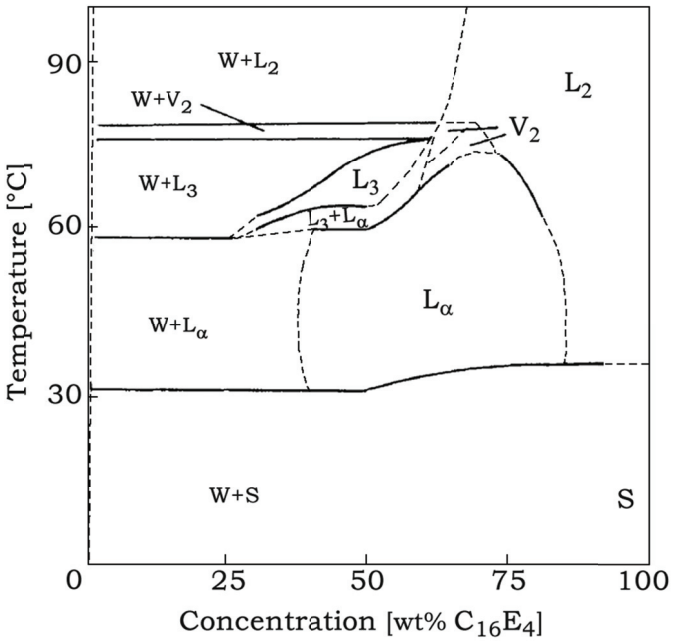

Figure 2.4.4: Phase diagram of the $C_{16}E_4$/water system over the temperature range 0-100°C, reproduce from [106] (V_2, reversed 'bicontinuous' cubic phase).

2.5 ANIONIC SURFACTANTS

Anionic Surfactants are dissociated in water in an amphiphilic anion, and a cation, which is in general an alcaline metal (Na^+, K^+) or a quaternary ammonium [13, 43]. In solution, the polar head is negatively charged. The hydrocarbon part of the surfactant can be a straight-chain aliphatic radical, as in the case of sodium dodecyl sulphate, as well as a branched-chain, unsaturated radical. For ionic surfactant, the spontaneous curvature is strongly influenced by salt concentration of the aqueous phase. If the salt concentration is increased, the effective charge of the head group will be shielded and the surfactant heads repel each other. This can lead to a change from H > 0 → H < 0. The temperature dependence of H for an ionic surfactant film is opposite to the salt dependence (H < 0 → H > 0), since the Debye screening length is given by

$$\frac{1}{\kappa_D} = \sqrt{\frac{\varepsilon RT}{2F^2 I}} \qquad (2.5.1)$$

where ε is the permittivity, F the Faraday constant and I the ionic strength of the aqueous phase. For nonionic and ionic surfactants, the addition of alcohols with more than four C-atoms stabilizes structures which are curved toward water. Ionic surfactant with a strong polar head group, such as sodium dodecylsulfate (SDS), can only be brought into their balanced state (or even curved toward water) if salt and long chain alcohol are added. On the other hand, films made of a double tailed ionic surfactants, such as sodium di(2-ethylhexyl)sulfosuccinate (AOT), are close to their balanced state.

2.5.1 APFN/WATER SYSTEM

Perfluorinated surfactants are a specialty class of chemicals employed for a variety of applications, including lubricants, paints, cosmetics, and fire-fighting foams [119-121]. In general, perfluorinated surfactants are classified

into one of four categories: anionic, cationic, nonionic, and amphoteric, with anionic surfactants being the most significant class [120].

Ammonium perfluorononanoate (APFN) is an anionic surfactant that in water forms liquid crystalline phases. The phase diagram of APFN/H_2O system is delineated by the presence of a lamellar phase and a nematic phase with a wide isotropic solution, Figure 2.5.1. The aggregates of the nematic phase have a positive and diamagnetic anisotropy. In the presence of a magnetic field, the aggregates align parallel to the field direction. The phase transition from lamellar to nematic has been ascribed to the order-disorder transitions.

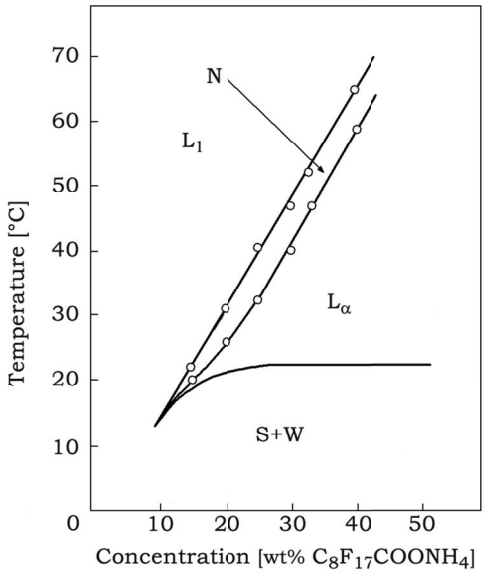

Figure 2.5.1: Phase diagram of the APFN/water system over the temperature range 0-70°C, reproduce from reference [122].

2.6 LECITHIN

The term lecithin connotes two meanings that are somewhat related but are not used in the same sense. (i) Lecithin is used like a generic term to designate any group of yellow-brownish fatty substances occurring in animal and plant tissues, and in egg yolk, composed of phosphoric acid, choline, fatty acids, glycerol, glycolipids, triglycerides, and phospholipids. (ii) Lecithin can be used as a synonym for phosphatidyl choline (PC), which is the major component of a phosphatide fraction.

Lecithin can easily be extracted chemically (using hexane) or mechanically from readily available sources such as soy beans. It has low solubility in water. In aqueous solution its phospholipids can form either liposomes, bilayer sheets, micelles, or lamellar structures, depending on hydration and temperature. This results in a type of surfactant that is usually classified as amphipathic. Lecithin is sold as a food supplement and for medical uses. In cooking, it is sometimes used as an emulsifier and to prevent sticking, for example in non-stick cooking spray.

2.6.1 LECITHIN/CYCLOHEXANE/WATER

Ternary surfactant solutions made of soybean phosphatidylcholine (Lecithin Epikuron 200 from Degussa Bioactives A.G., with a purity of 95% and average molecular weight of 772 Da.), water and cyclohexane, show an isotropic phase (I) where the micelles are highly entangled in a transient network, followed by a thin bi-phasic region (I+N) and then a nematic (N) phase. The N phase is stable in the micellar volume fraction range of 0.35-0.45. Figure 2.6.1 shows The lecithin/cyclohexane/water phase diagram [123].

The isotropic phase of the ternary system lecithin/cyclohexane/water, has been studied for more than ten years. It is now well established that the micelles have a general tendency to increase in size and become anisotropic

(cylindrical) with increasing water content and concentration [124]. When these elongated micelles exceed a certain persistence length, they become flexible. If the micelles are much longer than the persistence length ("wormlike micelles"), they assume very complex configurations resembling polymers in solution. They are often referred as to "living polymers" due to the fact that the micellar length is not chemically fixed, but rather fluctuates around an equilibrium length depending on the thermodynamical parameters. Above a certain concentration, the micelles begin to touch and become entangled.

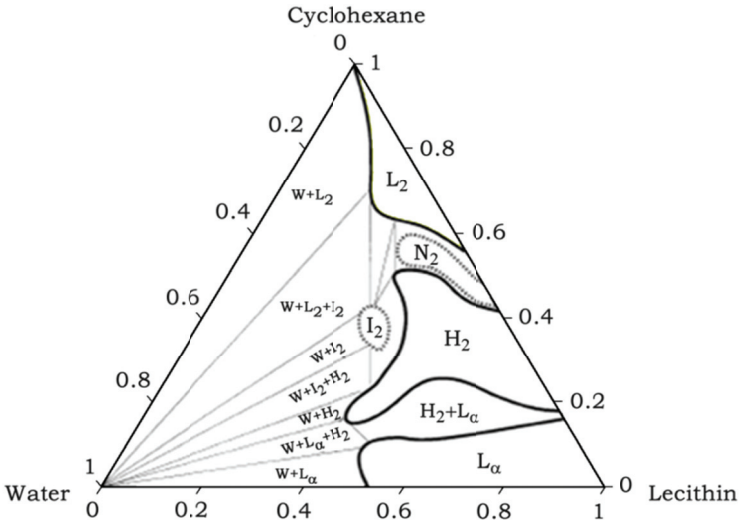

Figure 2.6.1: Phase diagram of the APFN/water system over the temperature range 0-70°C, reproduce from [123].

The preparation of the lecithin/cyclohexane/water samples has been conducted using the following smart equation

$$V_{gel}\,\Phi_{mic} = g_{LEC}\left(0.9806 + 0.023286\,W_0\right) \qquad (2.6.1)$$

V_{gel} is the final volume of the gel g_{LEC} is the quantity of lecithin (in grams), while Φ_{mic} is the micellar volume fraction and W_0 is the water-lecithin mole ratio. The cyclohexane volume has been calculated using $V_c = V_{gel}\left(1-\Phi_{mic}\right)$.

3 EXPERIMENTAL TECHNIQUES

3.1 RHEOLOGY

The flow properties of liquids play an important part in our daily lives either deliberately or accidentally. Rheology (from the greek word “rein”, to flow) is the science of deformation and flow of matter. No one is really an absolute beginner when it comes to rheology.

Fluid-like behavior is associated with flow: matter being deformed continually with time. Fundamental rheological variables can be defined by referring to an imaginary purely fluid sample confined between two parallel plates (Figure 3.1.1). The plates are separated by a distance h that is small if compared to the linear dimensions of the plates. The bottom plate is held stationary, while parallel to the top plate a certain force (F) per unit area (A) is applied (shear stress, σ). When the force is applied as shown in Figure 3.1.1, the upper plate responds immediately by moving a distance, y, from left to right. The shear strain (γ) is then defined as y/h and it is dimensionless. The fluid in contact with the upper plate moves equally fast, with velocity v.

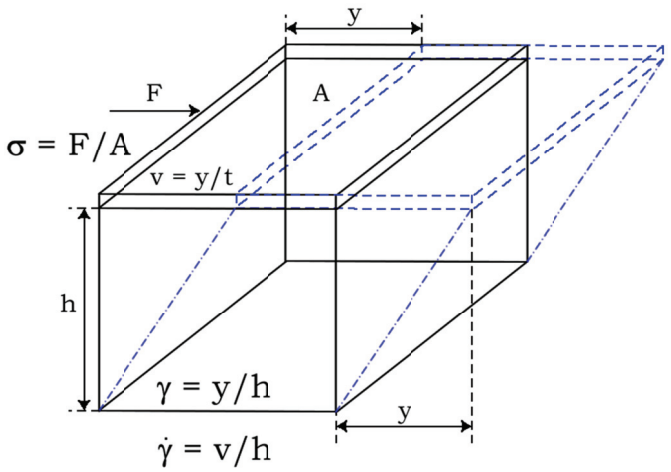

Figure 3.1.1: Simple shear experiment: definitions of stress, strain and shear rate.

For laminar and ideal-viscous flow, the difference in velocity between neighboring layers (Figure 3.1.2) shows the same value (dv = const.) since the velocity v(h) decreases linearly in the shear gap between the plates. All the layers are assumed to have the same thickness (dh = const.). Therefore, the shear rate is showing a constant value everywhere between the plates since shear rate $\dot{\gamma} = dv / dh = const / const = const = v / h$ [127, 128].

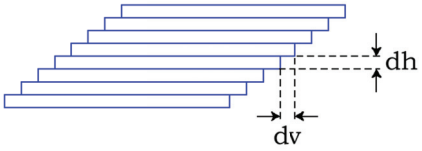

Figure 3.1.2: Laminar flow in the form of fluid layers.

The discussion above is very much simplified because of the stress, strain and shear rate are all tensor quantities.

3.1.1 SOLID, LIQUID AND VISCOELASTIC MATERIALS

Consider a small solid cube having sides of length ℓ and one face area A = ℓ^2. Suppose that the bottom surface is held in place, and that we apply a shear force F parallel to plane of the top surface. The shear stress σ is the shear force divided by the surface area. In response to the applied shear force, the solid cube will deform by an amount $d\ell$. The shear strain γ is the relative deformation, given by $\gamma = d\ell / \ell$. For a perfectly elastic solid, Hooke's Law tells us that stress and strain are linearly proportional, that is

$$\sigma = G'\gamma \qquad (3.1.1)$$

where the elastic modulus G′ is a measure of the elastic energy stored in the material when it is deformed. Hooke's Law implies reversibility, which means that the deformation immediately returns to zero when the shear stress is removed.

If we apply the same shear stress to a cubic element of a Newtonian fluid, the material flows continuously and the strain continues to increase meanwhile that the stress is applied. Newton's law of viscosity states that

$$\sigma = \eta\dot{\gamma} \qquad (3.1.2)$$

Here the shear rate is proportional to the stress. This equation defines the viscosity η, which is related to the dissipation energy in the flow; η describes the tendency of a material to resist flow.

In general, the response of soft matter systems or complex fluids to an applied deformation or stress is time-dependent – they typically behave as

solids on short time scales or at high frequencies and as viscous liquids over long times or at low frequencies. For example in the simplest case, when a viscoelastic material is subjected to a step increase in strain by an amount γ_0, the stress σ in the material undergoes a step change followed by an exponential relaxation. For small strains, one can define a relaxation modulus $G(t)=\sigma(t)/\gamma_0$, which is independent of γ_0, so that

$$d\sigma = G(t)\,d\gamma \tag{3.1.3}$$

Analogously, in a creep experiment, the stress is suddenly increased from zero to some value σ_0. In this case, the strain will initially rapidly change, then it continues to evolve slowly as a function of time. The creep compliance is defined as $J(t)=\gamma(t)/\sigma_0$, and it is conceptually equivalent to the reciprocal of the relaxation modulus G(t). The range of strains in which stress and strain are linearly related is called the linear viscoelastic regime. In this regime, the strain is small enough to not disrupt any structure in the material, thus one can probe the response of the material to small perturbations in its equilibrium configuration. At higher strains, the structure is disrupted and the response of the material change. In particular, the material properties become functions of strain or shear rate, and often function of time as well. The simplest model of a viscoelastic material is originally due to Maxwell [129] and it is mechanically equivalent to a spring in series with a viscous damper (dashpot), as in Figure 3.1.3. If we stretch this combined system by a displacement x, a force F is developed that obeys the differential equation

$$F + \frac{\mu}{k}\frac{dF}{dt} = \mu\frac{dx}{dt} \tag{3.1.4}$$

There are three primary types of measurements that one can perform with a rheometer: dynamic shear (oscillatory), steady shear and transient measurements.

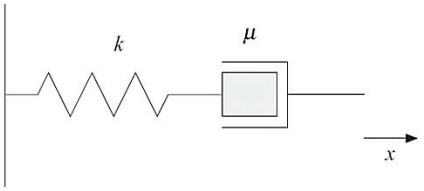

Figure 3.1.3: The spring-dashpot representation of the Maxwell model for a viscoelastic medium. The viscous and elastic elements are combined in series and stretched by a distance x, from reference [128].

3.1.2 DYNAMIC SHEAR EXPERIMENTS

Small-amplitude dynamic shear measurements are used primarily to determine the elastic (storage) and viscous (loss) moduli. When a material is subjected to a small sinusoidal strain – small enough for the material to remain in the linear viscoelastic regime – the resulting stress oscillates sinusoidally at the same frequency, but in general with a phase shift ϕ with respect to the strain. Thus if γ is given by

$$\gamma = \gamma_0 \sin \omega t \tag{3.1.5}$$

The resulting stress is

$$\sigma = \sigma_0 \sin\left(\omega t + \phi\right) \tag{3.1.6}$$

The stress in Equation 3.1.6 can be decomposed into a component in phase with the strain and another 90° out of phase component:

$$\sigma = \sigma' + \sigma'' = \sigma_0' \sin \omega t + \sigma_0'' \cos \omega t \tag{3.1.7}$$

The in-phase component is the elastic part of the response, with the elastic modulus defined as

$$G' = \frac{\sigma_0'}{\gamma_0} \tag{3.1.8}$$

While the out-of-phase component is the viscous part, with the viscous modulus given by

$$G'' = \frac{\sigma_0''}{\gamma_0} \tag{3.1.9}$$

The viscous response is out of phase with the strain, but in phase with the shear rate $\dot{\gamma}$. It is common to define a complex modulus G* as

$$G^* = G' + iG'' \tag{3.1.10}$$

G′ is a measure of the elastic energy stored per unit volume per cycle, while G″ is a measure of the dissipated energy per unit volume per cycle [130]. G′ and G″ are not independent quantities, but satisfy the Kramers-Kronig relations [131]; similarly, both are related to the relaxation modulus G(t) [127].

For a Maxwell model with a single relaxation time φ, it is straightforward to show that G′ and G″ depend on the frequency of oscillation (ω) as

$$G'(\omega) = G_0 \frac{\omega^2 \varphi^2}{1+\omega^2 \varphi^2} \tag{3.1.11}$$

$$G''(\omega) = G_0 \frac{\omega \varphi}{1+\omega^2 \varphi^2} \tag{3.1.12}$$

The frequency dependence of the elastic and viscous moduli reflects the time dependence of the small-scale dynamics of the material.

3.1.3 STEADY FLOW EXPERIMENTS

In steady shear experiment, a series of constant shear rates is applied once the system has reached a steady state and the stress is measured at each rate. Such experiments are inherently nonlinear, since the strain increases steadily with time along the time of the experiment. The material typically exhibits a transient stress response as its microscopic structure is driven out from its equilibrium state, then settles to a constant stress once the microstructure has reached a new nonequilibrium configuration, which depends on the shear rate. The result of such a measurement is a plot of stress versus shear rate, commonly called flow curve. Shear stress is related to the viscosity, in fact from steady shear experiments, we have

$$\eta(\dot{\gamma}) = \frac{\sigma}{\dot{\gamma}} \tag{3.1.13}$$

Qualitative flow curves on linear scale for three types of fluid behavior are shown in Figure 3.1.4. The linear relation typical of Newtonian fluids is also included.

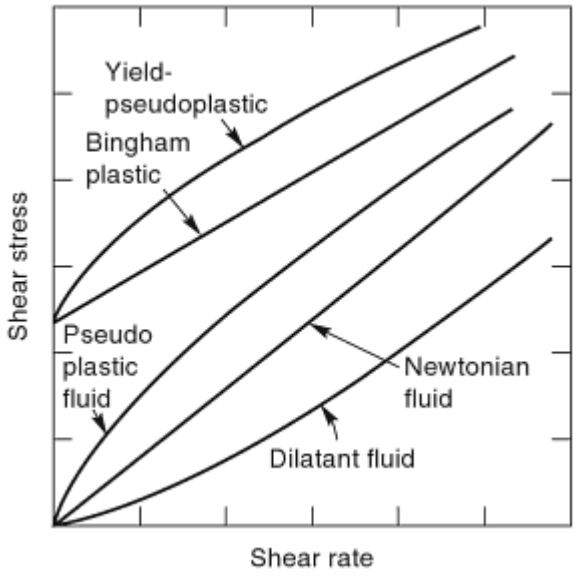

Figure 3.1.4: Flow curves, overview.

These fluids may be further subdivided into three types: a) shear thinning or pseudoplastic; b) viscoplastic; c) shear-thickening or dilatant.

The most common type of time-independent non-Newtonian fluid behavior is pseudoplasticity or shear-thinning, characterized by an apparent viscosity which decreases with increasing shear rate. The viscoplastic fluid behavior is characterized by the existence of a yield stress which must be exceeded before the fluid deforms or flows. Conversely, such a material will deform elastically when the externally applied stress is smaller than the yield stress. Dilatant fluids are similar to pseudoplastic systems because their (apparent) viscosity increases with increasing shear rate but they do not show yield stress; thus this behavior is called shear thickening [132].

3.1.4 Transient experiments

In a transient measurement, a step strain is applied, and the resulting stress recorded as it relaxes. Similarly, a step stress can be applied and the strain measured as a function of time. The former is a stress relaxation experiment, and the latter a creep experiment. One can also apply shear at a fixed shear rate and record the stress transient discussed above. A Newtonian

fluid dissipates – but does not store – energy, and so it responds instantaneously to an applied stress or strain. The presence of a transient response is thus an indication of elastic effects, and consequently measurements of stress relaxation or other transient effects are useful as probes of the elastic behavior of a material. In particular, stress relaxation is a fairly direct method of determining the relaxation times of a material. In the simple Maxwell model, φ is described by equation

$$\sigma + \varphi \frac{d\sigma}{dt} = \eta \frac{d\gamma}{dt} \qquad (3.1.14)$$

The flow curve (previously described) can be also obtained with a set of transient flow experiments. Each point on the flow curve can be determined after stabilization of the transient response from the previous steady state when a new shear rate (higher or lower) is applied.

3.1.5 Instruments and Geometries

There are two main types of rheometers, namely stress and strain controlled. In order to understand the differences between the two rheometers, we consider a fluid between two parallel plates separated by a gap *h*. In a strain-controlled rheometer one plate (the upper plate) is moved at a constant speed, while the other plate is fixed. The no-slip boundary condition ensure that the flow velocity is v = 0 at the bottom plate, while v = v_0 at the top plate. As a result, a uniform shear is set up in the fluid, and the shear rate within the fluid layer is $\dot{\gamma} = \delta v / \delta y = v_0 / h$. The horizontal (shear) force required to hold the lower plate fixed in position is measured by a transducer and the corresponding shear stress is calculated from the geometry of the experiment. In a stress-controlled rheometer the lower plate is also fixed. A known force applied to the upper plate causes it to move, and its displacement and velocity are measured.

Several different tool geometries can be used for the rheometer setup, which contains and deforms the sample to be studied. Three commonly used geometries are illustrated in Figure 3.1.5. Figure 3.1.5(A) shows a cone-and-

plate tool. The bottom part of the tool is a horizontal plate, while the other part is a truncated cone. The gap between the cone and plate is set such that the extrapolated tip of the cone would just touch the surface of the plate. The angle between the surface of the cone and the plate is small, typically a few degrees so that the small-angle approximation is valid.

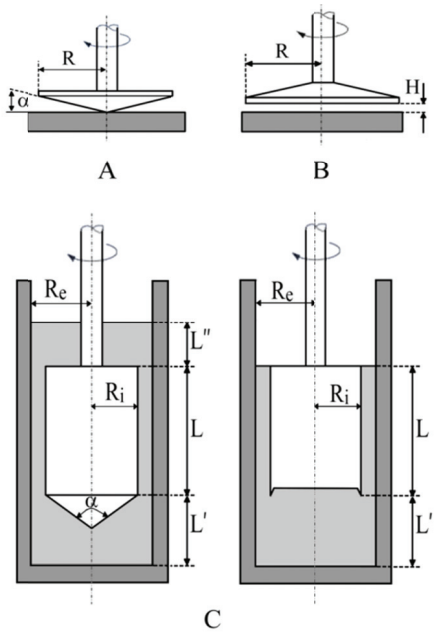

Figure 3.1.5: Three commonly used rheometer tool geometries. (a) Cone-and-plate; (b) parallel plates; (c) the Couette, or concentric cylinder, geometries. In all cases, one part of the tool is fixed and the other rotates around its axis (dashed-lines in figure).

The sample fills the gap between the two parts of the tool, remaining confined by surface tension. A parallel-plate tool is shown in Figure 3.1.5(B). In this case, both parts of the tool are planar, and the sample again fills the gap between them. The separation between the two parts of the tool can be varied. The Couette geometries, shown in Figure 3.1.5(C), consist of an outer cylinder (cup) of radius R_e and a coaxial inner cylinder (bob) of radius R_i and length L. The fluid sample fills the annular gap between the two cylinders, as well as the volume below the inner cylinder, L′ in Figure 3.1.5(C). The shape and depth of L′ volume should be designed to minimize its effects on the measurements. The Couette geometry on the left in Figure 3.1.5(C) is used in stress-controlled rheometers, while the Couette on the right is used in strain-controlled rheometers.

In practice, loading the sample into the rheometer tool cannot be done without causing some disruption to its structure. As an example, to load the

cone-and-plate tool, the upper cone is raised well above the lower plate, an appropriate amount of the sample is placed on the plate, and the cone is then lowered to reach the correct gap. As the cone is lowered, the sample is squeezed between the two parts of the tool. This clearly shears the sample in a some uncontrolled way. This can be avoided either by giving the sample adequate time to recover its equilibrium structure before measuring, or by subjecting it to a controlled "pre-shear" to prepare it in a reproducible initial state before starting measurements.

In all cases, the flow within the material under study must be steady and laminar, and no secondary flows due to hydrodynamic instabilities (such as Taylor vortices in the Couette geometry) should be present [133]. Some high-viscosity materials are subject to elastically driven "edge failure" at the free surface of the sample, and some materials exhibit instabilities that cause the sample to be expelled from the open edge of the tool at higher shear rates [130]. These phenomena limit the range of shear rates over which measurements can be made for particular materials. Some materials, particularly thixotropic (that is, history dependent) yield-stress materials, are prone to shear localization [134], both in the inner of the sample (shear banding) or at the interface between the sample and the rheometer tool (wall slip). This will also affect the accuracy of rheological measurements. Using the cone-plate and parallel-plate geometries, care must be taken to avoid evaporation at the free surface.

The relationship between the shear stress, which is the rheological quantity of interest, and the torque, which is the quantity actually measured (or applied), depends on the geometry of the tool. In the cone-plate geometry, Figure 3.1.5(A), simple shear flow is produced in the azimuthal direction when the plate is rotated at a constant angular velocity Ω, and, as long as the cone angle α is small, the shear rate is the same everywhere in the sample. It is given by

$$\dot{\gamma} = -\frac{\Omega}{\alpha} \tag{3.1.15}$$

If the plate is rotating, the torque M on the cone is

$$M = \int_0^{2\pi} \int_0^R \sigma r^2 d\phi dr \tag{3.1.16}$$

where σ is the shear stress on the surface of the cone, and the integral is over that surface. Since the shear rate is constant, the shear stress is also constant and can be removed from the integral, in which case it is straightforward to show that

$$\sigma = \frac{3M}{2\pi R^3}. \tag{3.1.17}$$

Because the deformation of the sample is homogeneous and the shear rate and stress are independent of position, the cone-plate is the most commonly used geometry to study soft materials.

In the parallel-plate geometry of Figure 3.1.5(B), the shear rate is simply given by

$$\dot{\gamma} = -\frac{\Omega r}{H} \tag{3.1.18}$$

where H is the spacing between the plates and r the radial coordinate. H can be varied and should be small if compared to the radius R of the plates and large if compared to the scale of any structure in the material (for example, the size of any suspended particles). In this geometry, the deformation is not uniform: Equation 3.1.18 shows that the shear rate depends on r. The shear stress can be calculated in terms of the torque

$$\sigma = \frac{M}{2\pi R^3}\left(3 + \frac{d\ln M}{d\ln \dot{\gamma}_R}\right) \tag{3.1.19}$$

where $\dot{\gamma}_R$ is the shear rate on the edge of the plate [130]. Note that in principle the derivative in Equation 3.1.19 has to be measured to permit an accurate determination of the stress [135], while rheometer software typically calculates an effective stress based on the approximation to Eq. 3.1.19 which assumes a particular value for $d\ln M/d\ln \dot{\gamma}_R$ [130]. The parallel-plate tools are simple to use, and when H is small, it can be used for measurements at high shear rates. Measurements at different values of H can also be used to check and correct the eventual slipping at the surfaces of the tool [136].

In the Couette geometry where the inner cylinder is fixed and the outer is rotating at a constant angular velocity, the velocity field in the fluid is purely

azimuthal. In this case, the shear stress σ on the inner cylinder at r = R_i can straightforwardly be shown to be [130]

$$\sigma = \frac{M}{2\pi R_i^2 L}, \tag{3.1.20}$$

where R_i is the radius of the inner cylinder and L its length. If the gap between the cylinders is small, that is, if $R_e - R_i << R_i$, then the shear rate in the gap is uniform and is given by

$$\dot{\gamma} = \frac{\bar{R}\Omega}{R_e - R_i}, \tag{3.1.21}$$

where R_e is the radius of the outer cylinder, and $\bar{R} = R_e + R_i/2$. If the gap is not small (as is usually the case in practice), the shear rate varies through the gap and the analysis becomes more complex. As with the parallel-plate geometry, the shear rate then involves a derivative, in this case $d\ln M/d\ln\Omega_i$. In principle, this must be measured, but in practice an approximation is often used. The Couette geometry is well-suited for measurements on low viscosity fluids because of the large surface area of the tool. Also measurements at high shear rate can be performed, as the fluid cannot easily be expelled from the gap between the cylinders.

3.1.6 Flow instabilities in a Couette geometry

Secondary flow effects may occur when measuring low-viscosity liquids at high shear rates. This can lead to turbulences, and as a consequence, to uncontrolled increasing flow resistance.

Taylor number and Taylor vortex flow in the Couette geometry [137-139].

For liquids flowing in the gap of a Couette geometry there is a critical upper limit between laminar and turbulent flow behavior at which flow instabilities occur if the bob is rotating and the cup is stationary. This is due to centrifugal forces and inertial effects caused by the mass of the fluid. The Taylor instabilities do not occur for Couette with a rotating cup and a stationary bob

(usually used in strain-controlled rheometers). It is possible to determine the corresponding limit value via the *Taylor number* (Ta) which depends on the rotational speed (angular velocity ω in rad/s) and the radius R_i (m) of the bob, the density ρ (kg/m^3) and the viscosity η (Pas) of the fluid, and the ratio of the radii δ_c (shear gap). Calculation of Ta number has been defined by the German standards body, Deutsches Institut für Normung (German Institute for Standardization) DIN 53018 / DIN 53019:

$$Ta = \frac{\omega_c \rho R_i^2 \left(\delta_c - 1\right)^{3/2}}{\eta} \geq 41.2 \qquad (3.1.22)$$

According to the DIN standard, the above formula to calculate the Ta number is only valid for $1 < \delta_c < 1.04$ as stated in ISO 3219. For higher value of δ_c a more complex formula should be used. However the difference between the two methods is not more than 5%.

Using the Equation 3.1.22, the stability criterion for the critical angular velocity ω_c (where Ta vortices are occurring) is

$$\omega_c = \frac{\left(41.2\eta\right)}{\left[\rho R_i^2 \left(\delta_c - 1\right)^{3/2}\right]} \qquad (3.1.23)$$

Reynolds number in the Couette geometry [139-141].

Turbulent flow behavior also occurs when the critical Reynolds number (Re) is reached. The Re number characterizes the ratio of the forces caused by the mass inertia over those of the flow resistance of the fluid. Calculation of the *Re number* in its general form:

$$\mathrm{Re} = \frac{\left(v_m L \rho\right)}{\eta} \qquad (3.1.24)$$

where v_m (m/s) is the mean velocity of the fluid, L is the geometrical dimension (the Couette gap R_e-R_i in meter), ρ (Kg/m^3) is the density, and η (Pas) is the viscosity of the fluid. Using "representative values" according to ISO 3219: $v_m = \omega R_{rep}$ with $R_{rep} = \left(R_e + R_i\right)/2$. Therefore

$$\mathrm{Re} = \frac{\left[\omega \rho R_i^2 \left(\delta_c^2 - 1\right)\right]}{\left(2\eta\right)} \qquad (3.1.25)$$

There are two critical Re numbers existing: 1) Re_{c1} = 1, occurrence of "end effects" (causing flow instabilities around the edges of the upper and lower end of the cylindrical part of the bob); 2) 1000 < Re_{c2} < 10000, occurrence of turbulence in the circular gap itself. Therefore the critical angular velocities ω_{c2} and ω_{c1} (rad/s) are reached if

$$\omega_{c2} = \frac{\left(2\eta \,\mathrm{Re}_{c2}\right)}{\left[\rho R_i^2 \left(\delta_c^2 - 1\right)\right]} \tag{3.1.26}$$

$$\omega_{c1} = 0.001\omega_{c2}\,. \tag{3.1.27}$$

3.2 NUCLEAR MAGNETIC RESONANCE (NMR)

Nuclear magnetic resonance (NMR) spectroscopy is a powerful technique that exploits the magnetic properties of certain atomic nuclei to determine physical and chemical properties of atoms or the molecules in which they are contained. It can provide detailed information about the structure, dynamics, reaction state, and chemical environment of molecules. In principle, NMR is applicable to any nucleus possessing spin. The spin is an intrinsic angular momentum of the magnetic nuclei, whose magnitude is $\left[I\left(I+1\right)\right]^{1/2}\hbar$. The spin quantum numbers (I) of some commonly occurring nuclei are given in Table 3.2.1.

I	***Nuclei***
0	^{12}C, ^{16}O
1/2	^{1}H, ^{13}C, ^{15}N, ^{19}F, ^{29}Si, ^{31}P
1	^{2}H, ^{14}N
3/2	^{11}B, ^{23}Na, ^{35}Cl, ^{37}Cl
5/2	^{17}O, ^{27}Al
3	^{10}B

Table 3.2.1: Some commonly nuclear spin quantum numbers.

It is worthy to note that ^{12}C and ^{16}O have I = 0, i.e. there is no angular momentum, no magnetic moment and consequently no NMR spectra. The angular moment ***I*** of a spin-I nucleus has just $2I$+1 projections onto an arbitrarily chosen axis, say the z axis. That is, the z component of ***I***, denoted by I_z is quantized:

$$I_z = m\hbar \qquad (3.2.1)$$

where m, the magnetic quantum number, has $2I$+1 values in integral steps between $+I$ and $-I$, $m = I, I-1, I-2, \ldots -I+1, -I$. In the case of I = ½ (for example ^{1}H), the angular momentum has two permitted directions, $I_z = \pm\frac{1}{2}\hbar$, while a nucleus with I = 1 (for example ^{2}H) has three possible state, $I_z = 0, \pm \hbar$. The magnetic moment **μ** of a nucleus is directly proportional to ***I***:

$$\boldsymbol{\mu} = \gamma \boldsymbol{I} \qquad (3.2.2)$$

where γ is the gyromagnetic ratio. γ is equal to $\hbar^{-1}g\mu_N$ where μ_N is the nuclear magneton, and g is the g-factor of the nucleon or nucleus in question.

When nuclei with non-zero spin, and hence non-zero magnetic moments, are placed into a static magnetic field, $\mathbf{B_0}$, they are subject to various interactions described by the total spin Hamiltonian,

$$\hat{H}_S = \hat{H}_z + \hat{H}_Q + \hat{H}_{rf} + \hat{H}_D + \hat{H}_{CS} + \hat{H}_J \qquad (3.2.3)$$

$\hat{H}_z$ is the Zeeman interaction and it is the interaction between magnetic moment $\boldsymbol{\mu}$ and magnetic field $\mathbf{B_0}$:

$$\hat{H}_z = -\boldsymbol{\mu}\cdot\mathbf{B_0} = -\gamma \boldsymbol{I}\cdot\mathbf{B_0} = -\gamma\left(I_x B_{0x} + I_y B_{0y} + I_z B_{0z}\right) \qquad (3.2.4)$$

If the magnetic field is in the z direction the Zeeman Hamiltonian can be written:

$$\hat{H}_z = -\gamma I_z B_0 \qquad (3.2.5)$$

Solving the Schrödinger equation $\hat{H}_z|m\rangle = E|m\rangle$, where $|m\rangle$ are the nuclear spin levels functions, these levels are distinguished by a different quantum number m, then we obtain $2I+1$ values of energy:

$$E = -m\hbar\gamma B_0 \qquad (3.2.6)$$

The $2I+1$ states for a spin-I nucleus are equally spaced, with energy gap $\hbar\gamma B$ (Figure 3.2.1).

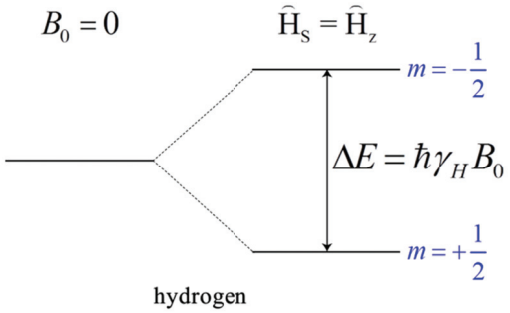

Figure 3.2.1: Energy levels for hydrogen nucleus in a magnetic field B_0 considering the Zeeman interaction.

In the Eq. 3.2.3 $\hat{H}_Q$ is the quadrupolar interaction Hamiltonian, $\hat{H}_{rf}$ is the Hamiltonian describing the interaction of radio frequency radiation with the nuclear spins, $\hat{H}_D$ represent the dipolar coupling, $\hat{H}_{CS}$ the chemical shift and $\hat{H}_J$ the indirect coupling. All of this interactions are weaker than the Zeeman interaction. Nuclei with a spin I = ½ have a spherical charge distribution and therefore, do not exhibit an electric quadrupole moment **Q**.

Assuming that an oscillating magnetic field (i.e. rf) $2\mathbf{B_1}\cos(2\pi\upsilon_1 t)$ is along the x-direction (with radio frequency, υ_1) perpendicular to the static magnetic field $\mathbf{B_0}$:

$$\hat{H}_1(t) = h\gamma B_1 I_x \cos(2\pi\upsilon_1 t) \qquad (3.2.7)$$

This hamiltonian of interaction make known to transitions between the energy levels of spin that have been separated by the Hamiltonian $\hat{H}_S$. The frequency associated to the transition from the lower energy state to the higher energy state is given by:

$$\upsilon_0 = \frac{\Delta E}{h} = \frac{\gamma B_0}{2\pi} \qquad (3.2.8)$$

The relative angular frequency is $\omega_0 = 2\pi\upsilon_0$ and it is known as the Larmor Frequency. The magnetic field, $\mathbf{B_1}$, influences (move) the net magnetization, $\mathbf{M} = \sum_i \boldsymbol{\mu}_i$ of the overall sample due to changes in occupancy in the spin state. In other words **M** reflects the difference of population between the upper and lower spin levels (for I = ½ nuclei system).

The return of magnetization, **M**, to its equilibrium state is known as relaxation. There are three factors that influence the decay of M: magnetic field inhomogeneity, spin-lattice (longitudinal) T_1 relaxation and spin-spin (transverse) T_2 relaxation. T_1 relaxation is the mechanism by which the z component of the magnetization vector **M** comes into thermodynamic equilibrium with its surroundings (the "lattice"). T_2 relaxation is the mechanism by which M_{xy}, the transverse component of the magnetization vector, exponentially decays towards its equilibrium value of zero.

A more complete discussion of nuclear interactions may be found in some NMR text such as Abragam [142], Levitt [143].

3.2.1 ^{2}H-NMR AND LIQUID CRYSTALLINE SYSTEMS

Nuclei with a spin I > ½ have a non-spherical charge distribution and therefore, exhibit an electric quadrupole moment, **Q**. The **Q** moment can interact with the local electric field gradient, arising from the electron shell. Considering Zeeman and the quadrupolar the only interactions taken into account, the total spin Hamiltonian of the system has just two components:

$$\hat{H}_S = \hat{H}_z + \hat{H}_Q \qquad (3.2.9)$$

It is possible to demonstrate that for a system of nuclei with I = 1, in an axially symmetric field, the $\hat{H}_Q$ takes the following form [142]

$$\hat{H}_Q = \frac{e^2qQ}{8}\left(3I_z^2 - 2\right)\left(3\cos^2\theta - 1\right) \qquad (3.2.10)$$

where the product e^2qQ is the motionally average quadrupolar constant (δ) and θ is the polar angle. Solving the Schrödinger equation $\hat{H}_{zQ}|m\rangle = E|m\rangle$ we obtain

$$E = m\gamma B_0 + \left(3m^2 - 2\right)\frac{e^2qQ}{8}\left(3\cos^2\theta - 1\right) \qquad (3.2.11)$$

For spin I = 1, i.e. deuterium, the magnetic quantum number can be -1, 0 and 1. The energy levels for such a system are illustrated in Figure 3.2.2. From Eq. 3.2.11 it can be seen that we obtain two resonance lines at $\omega_0 \pm \omega'$ where $\omega' = (3e^2qQ/8)(3\cos^2\theta - 1)$ making the splitting, $\Delta\upsilon_Q = 2\omega'$, equal to

$$\Delta\upsilon_Q = \frac{3}{4}\delta\left(3\cos^2\theta - 1\right) \qquad (3.2.12)$$

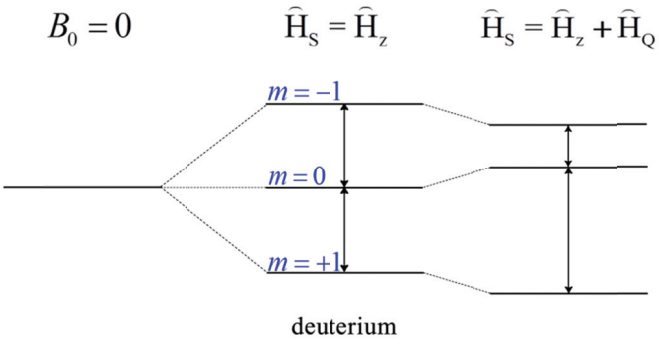

Figure 3.2.2: Energy levels for deuterium nucleus in a magnetic field $\mathbf{B}_0$ considering the Zeeman and the quadrupolar interaction.

^{2}H-NMR spectroscopy turns out to be a very convenient technique that has the ability to probe structure even in partially ordered system and molecular dynamics in solid and semi-solids [144]. The orientation-dependent splitting of peaks yields a clue on how a X^{2}H vector of a molecule under consideration is oriented to the applied magnetic field when crystalline, mechanically, or magnetically oriented samples are utilized. However most of the samples are not homogeneously oriented respect to $\mathbf{B_0}$, but are randomly distributed as in microcrystalline samples. The "powder pattern", so called

"Pake doublet" with two "horns", is formed as a result of inhomogeneously broadened peaks, Figure 3.2.3.

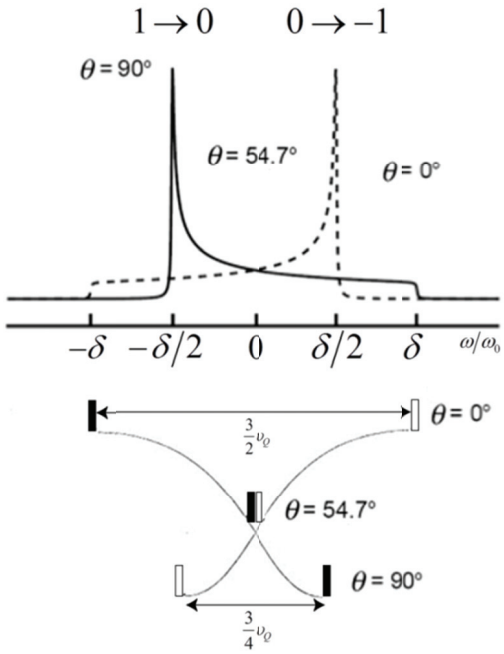

Figure 3.2.3: The shape of the Pake doublet is due to the fact that there are different possible values of θ.

The ^2H NMR is a useful technique in the study of lyotropic liquid crystals. The ^2H NMR spectrum of a liquid crystalline anisotropic phase containing ^2H_2O confined in a layer, i.e. lamellar phase L_α, (see Paragraph 2.2.1) exhibits a quadrupolar splitting characteristic of the residual couplings that arise from the anisotropy of the rotational motions of the water molecules. Despite the rapid tumbling motion of water molecules a small degree of orientational order remains enforced by the orientation of the anisotropic liquid crystalline phase. Thus, the quadrupolar interaction has a nonzero average, leading to a splitting of the resonance. In the case of uniaxial symmetry, as for the L_α, the ^2H spectrum consists of a doublet with a frequency separation given by Eq. 3.2.12. Moreover, according to referred equation, the deuterium NMR line shape depends on the distribution of the director orientation θ, which is the angle between the director (the symmetry axis of the phase) and the magnetic field, $\mathbf{B_0}$. A simple doublet is observed only if the lamellar phase has been well aligned along a given direction, for instance by the action of the magnetic field or by the application of a shear flow. A disordered lamellar phase, consisting of many domains of extended flat layers whose orientations are isotropically

distributed in space, gives rise to the characteristic line shape of a polycrystalline sample (Pake doublet). On the other hand ^{2}H NMR spectra of isotropic phase, as cubic liquid crystalline or a random multi-connected sponge, exhibit zero splitting. The quadrupolar interaction is averaged to zero due to the rapid (faster than the inverse of the quadrupolar interaction) averaging of θ.

As long as the lamellae are planar, the diffusive motion of the probe molecule has no extra rotational component besides the anisotropic local tumbling and the characteristic quadrupole coupling of the lamellar phase is not affected. However, when the layers are curved, diffusion along the layers is connected to a rotation and therefore leads to an additional motional narrowing of the spectrum. This results in a decrease and eventually a collapse of the quadrupolar splitting. For MLVs with a typical radius of a few micrometers, a distribution of averaged quadrupole coupling is expected: while diffusion in the inner shells leads to isotropic averaging, diffusion in the outer shells covers only part of the sphere, in the NMR time scale, resulting in a residual coupling. Thus the result is a superposition of spectra with different couplings yielding the observed relatively broad but featureless lines. When the two morphologies of the lamellar phase (aligned planar lamellae and MLVs) coexist, the spectrum consists of a superposition of a central singlet originating from MLVs and a Pake doublet arising from the aligned lamellar phase. The Figure 3.2.4 shows the ^{2}H NMR line shapes for an isotropic sponge phase, an oriented lamellar phase and an MLV system.

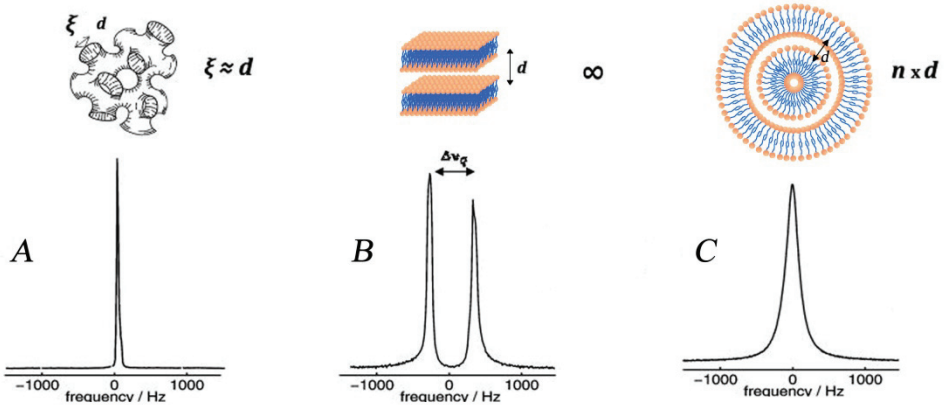

Figure 3.2.4: Experimental ^{2}H NMR line shapes for three different lamellar topologies: (a) a sponge phase; (b) an aligned lamellar phase; (c) Multilamellar vesicles. A schematic picture of each structure is shown.

3.2.2 RHEO-^{2}H NMR

Traditionally, rheology was a subject concerned principally with mechanical properties as described in the Paragraph 3.1. Attention has focused on trying to determine the molecular basis of complex mechanical properties. The interest in the molecular-mechanical link has led to the amalgamation of a number of spectroscopic and rheological techniques in which a flow or deformation cell is incorporated within the spectrometer detection system. Rheo-NMR, has provided a number of new and valuable features. In this thesis the rheo-NMR experiments have been carried out using a cylindrical Couette cell (9 mm inner radius, and 1 mm gap). This cell is integrated into an NMR probe with a diameter of 25 mm for a wide-bore superconducting magnet. A schematic representation of the rheo-NMR cell is given in Figure 3.2.5.

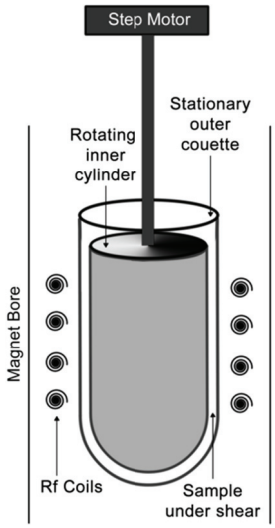

Figure 3.2.5: The Rheo-NMR tool is designed by a cylindrical Couette cell. This cell is integrated into an NMR microimaging probe (25 mm) for a wide-bore superconducting magnet. The axis of the shear cell is aligned parallely to the external magnetic field. Shear is applied by rotating the outer cylinder which is connected to a stepper-motor.

Rheo-NMR spectroscopy on some lamellar phase systems under shear flow has revealed interesting details. The doublet of the planar lamellae turns into a broad single peak when MLVs are formed by shaking or shearing the sample [73, 145-148]. In the references [73] is developed a simple model to determine the MLVs dimensions assuming the slow exchange of water molecules between adjacent layers and motional narrowing conditions which

implies that the ^{2}H NMR line shape is simply given by a sum of Lorentzians functions.

$$L(\upsilon) = \sum_{n=1}^{N} f_n \frac{2T_{2,n}}{1 + 4\pi^2 (\upsilon - \upsilon_0)^2 T_{2,n}^2} \qquad (3.2.13)$$

Any Lorentzian function corresponds to individual water layer n. $T_{2,n}$ is the spin-spin relaxation time associated with the layer number n, υ_0 is the resonance frequency and υ the absolute frequency. The Lorentzian will have different line width, because the layers have different radii, R_n, and they will have different weight, f_n, in the sum because the layers contain different number of water molecules, depending on their radius. The sum runs up to n = N, where N is the total number of layers. Assuming a constant bilayer spacing d, the MLV radius is given by R_{MLV} = Nd, and, $f_n \sim R_n^2 = n^2 d^2$.

The molecular motions responsible for the relaxation are the fast local reorientation motions that on the average are slightly anisotropic because of the presence of the bilayer interface and the slow isotropic reorientation associated with the diffusion of water molecules within the spherical water layer. This separation of timescales was recognized by Wennerström and co-workers, who developed the so-called two-step model of NMR relaxation [149-151]. The residual anisotropy remaining after partial averaging by the fast motions is quantified by an order parameter, S, that can be obtained from the quadrupolar splitting in the lamellar phase [149]

$$\Delta\upsilon_Q = \frac{3}{4}|\chi S| \qquad (3.2.14)$$

Here, χ is the quadrupolar coupling constant. The ^{2}H line width in the MLV state is much larger than in the sponge phase. This tells us that the transverse relaxation is mainly due to the slow motion and that it is sufficient to consider the zero-frequency spectral density of the slow motion, $j_s(0)$, in the expression for T_2 so that

$$\frac{1}{T_2} = \frac{9\pi^2}{40}|\chi S|^2 j_s(0) \qquad (3.2.15)$$

If the slow reorientation of water molecules is due to diffusion within a spherical shell of radius R, then we have $j_s(0) = R^2/3D$ where D is the diffusion coefficient. In conclusion it is possible to write a simple expression for $T_{2,n}$

$$\frac{1}{T_{2,n}} = \frac{2\Delta\upsilon_Q^2 d^2}{15D} n^2 + \frac{1}{T_{2,in\,\mathrm{hom}}} \qquad (3.2.16)$$

Here, we have also introduced a constant term, $1/T_{2,\mathrm{inhom}} = \pi\Delta\nu_{1/2,\mathrm{inhom}}$, to take into account the effect of magnetic field inhomogeneity on the line shape.

3.2.3 IMAGING NMR

NMR imaging is a technique to investigate material properties and structural changes, moreover it is a noninvasive analytical technique, which is capable of producing images of arbitrarily oriented slices through optically nontransparent objects. Biological tissue, plants, foodstuffs and many synthetic materials can be penetrated by rf waves, and the signal is hardly attenuated by absorption and emission of rf energy at the resonance frequencies of the nuclear spins. In this sense, the objects appear transparent to radio waves, while they are nontransparent to electromagnetic waves at optical frequencies, or exhibit different absorption properties at higher frequency irradiation, for instance, as provided by X-rays and electron beams [152].

NMR imaging can be perceived as a particular form of multi-dimensional spectroscopy, where the frequency axes have been converted to space axes by application of inhomogeneous magnetic fields. For convenience, space-invariant or constant magnetic-field gradients are generally used. A field gradient is the spatial derivative of the field. A constant gradient denotes a linear variation of the field with space.

In a space-dependent magnetic field, the Larmor frequency depends on position. A sufficiently weak space dependence of the magnetic field can be expanded into a Taylor series. For example, a variation along the x coordinate is described by

$$B_z(x) = B\big|_{x=0} + \left.\frac{\partial B_z}{\partial x}\right|_{x=0} x + \frac{1}{2}\left.\frac{\partial^2 B_z}{\partial x^2}\right|_{x=0} x^2 + \ldots \qquad (3.2.17)$$

In most imaging experiments, the second and higher order derivatives in this expansion are small and negligible. However, this is not a necessity to

obtain spatial resolution in NMR. In imaging experiments, the space variation of the external field must be made strong enough to override the spread in chemical shift or linewidth. In this case

$$\omega_0 = (1-\sigma)\omega - \gamma\left[G_x\big|_{x=0}\, x + \frac{1}{2}\frac{\partial^2 B_z}{\partial x^2}\bigg|_{x=0} x^2 + \ldots\right] \qquad (3.2.18)$$

ω is the NMR frequency without shielding. The quantity σ measures the degree of magnetic shielding. Magnetic shielding and chemical shift are used synonymously.

The linear relationship between NMR frequency and space coordinate is obtained by restricting the space dependence of the magnetic field to the field gradient $G_x = \partial B_z/\partial x$ in Eq. 3.2.18 and by neglecting chemical shift. In this case, each point along the x-axis of the sample is characterized by a different resonance frequency. The total signal intensity is proportional to the number of nuclei with a given NMR frequency. It is obtained by integration of the sample magnetization along the y- and z-coordinates and is thus given by the projection of the signal onto the x-axis. From a set of projections acquired with magnetic field gradients pointing in different directions, an image of the object can be reconstructed.

For a linear space dependence of the Larmor frequency, the spatial resolution $1/\Delta x$ is related to the width of the NMR absorption line or the spread $\Delta\upsilon = \Delta\omega_0/2\pi$ in Larmor frequencies ω_0, according to Eq. 3.2.18, is

$$\frac{1}{|\Delta x|} = \left|\frac{\gamma G_x}{2\pi\Delta\upsilon}\right| \qquad (3.2.19)$$

This expression applies to direct detection of the NMR signal in the presence of a magnetic field gradient G_x, also called frequency encoding of the space information. It states that the larger the linewidth, Δυ, the worse the spatial resolution $1/\Delta x$.

A phenomenological expression for the single-pulse response in NMR can be derived from Eq. 3.2.18 in terms of an attenuated precession of the transverse magnetization around the direction of the magnetic field in a given volume cell, or voxel, in the 3D case, or a picture cell, or pixel, in the 2D case,

$$M^+(t) = M_z(t=0)\, e^{\left\{-\frac{t}{T_2} + i\int_0^t \omega_0(t')dt'\right\}} \qquad (3.2.20)$$

The Larmor frequency is taken to be time dependent in order to account for effects of slow molecular motion as well as for the effects of time-dependent magnetic field gradients. The initial magnetization before the 90° excitation pulse at t = 0 is taken to be M_z which can be different from the thermodynamic equilibrium value M_0 as a result of incomplete relaxation or the use of a filter for longitudinal magnetization.

The time dependence of the Larmor frequency can be introduced by three sources: (i) The first term, the NMR frequency, may be modulated because of slow molecular rotation in solids, where the Larmor frequency depends on the orientation of the molecule with respect to the applied magnetic field; (ii) Another source is molecular translational motion. Then the space coordinate x and the respective powers of x are time dependent. This modulation is a sample property like rotational molecular motion in solids; (iii) The third source may be the time dependence of the field inhomogeneity expressed by the gradient G_x and higher-order spatial derivatives $\partial B_z^n \big/ (\partial x)^n$ of the magnetic field. If generated separately from the homogeneous field, the inhomogeneous field may be pulsed. In fact, pulsing of magnetic field gradients is a standard technology in NMR imaging. But even as an integral part of the polarization field, the time dependence of the inhomogeneous field effective for the spin precession can be manipulated through the application of rf pulses. Thus, rf pulses and pulsed magnetic-field gradients are used to interrogate rotational and translational molecular motion.

To understand where in this picture NMR imaging comes in, the time dependence of the position coordinates is expanded into a Taylor series, where the expansion coefficients at t = 0 denote the starting position x_0, the starting velocity v_{x0} in x-direction, the starting acceleration a_{x0} in x-direction, etc.:

$$x(t) = x_0 + v_{x0}t + \frac{1}{2}a_{x0}t^2 + \ldots \qquad (3.2.21)$$

and

$$x^2(t) = x_0^2 + 2x_0v_{x0}t + \left(v_{x0}^2 + x_0a_{x0}\right)t^2 + \ldots \qquad (3.2.22)$$

Combination of Eq. 3.2.20 and 3.2.21 with 3.2.18 provides the following expansion for the NMR signal:

$$M^{+}(t) = M_{z0} \prod_{k} \prod_{l} M_{kl} \tag{3.2.23}$$

The term M_{00} defines NMR spectroscopy including relaxometry [153]. It forms a subject in itself [142, 154, 155. The term M_{01} describes the contribution of the voxel position x_0 to the signal phase. The term is most important in NMR imaging, because it reveals how to obtain spatial resolution: The time integral of the gradient has to be varied over a sufficient range of values, and for each value a single data point is acquired. Fourier transformation with respect to the gradient integrals directly produces a signal amplitude as a function of position x_0, that is, a projection of the object onto the x-axis. Following the term M_{01}, the Fourier-conjugate variable to the position vector **r** is defined as

$$\boldsymbol{k} = -\gamma \int_{0}^{t} \boldsymbol{G}(t')\, dt' \tag{3.2.24}$$

Where the gradient vector is given by

$$\boldsymbol{G} = \left(\frac{\partial B_z}{\partial x}, \frac{\partial B_z}{\partial y}, \frac{\partial B_z}{\partial z} \right)^{t} \tag{3.2.25}$$

The quantity ***k*** is called the wave vector, and one component of it is a wave number. As the phase of the precessing magnetization increases with time under the influence of the magnetic-field gradient, the magnitude of the ***k*** vector changes accordingly. The alignment of ***k*** is parallel to ***G***, and the sign of ***k*** depends on the time dependence of ***G***. Thus, measurements of the NMR signal as a function of time t in the presence of the gradient ***G*** or as a function of ***G*** for fixed time intervals t, provide the image information in ***k*** space. Therefore, the NMR imaging methods are designed in such a way that information about all points in ***k*** space is acquired, so that the actual image is retrieved by simple Fourier transformation of the ***k***-space signal [156, 157].

Returning to the matrix 3.2.23 of phase terms, the quantities M_{11} and M_{21} describe the phase contributions from translational motion of nuclear spins from constant flow velocity v_{x0} and constant acceleration a_{x0} in space-invariant field gradients. This type of NMR is usually not considered to be part of spectroscopy, but has important applications in chemical engineering [158], [159] for imaging of flow profiles. This contribution to the signal phase,

therefore, forms part of the contrast resources to be exploited in NMR imaging. The phase terms M_{11} and M_{21} are manipulated in the experiment by suitable time-modulation of the gradient wave form $\boldsymbol{G}(t)$. The important parameters for encoding molecular transport properties in the signal phase are the gradient moments

$$\boldsymbol{m}_k = \int_0^t \boldsymbol{G}(t')t'^k dt' \qquad (3.2.26)$$

Clearly, the wave vector $\boldsymbol{k}$ and $\mathbf{m}_0$ are related by $\boldsymbol{k} = -\gamma\mathbf{m}_0$. The phase terms M_{k2} refers to quadratic field profiles. Such a profile is encountered in good approximation in single-sided NMR.

Consideration of the impulse response in a magnetic-field gradient immediately leads to a description and classification of imaging methods in reciprocal space or $\boldsymbol{k}$ space [160, 161]. This is the space obtained by Fourier transformation over space coordinates $\boldsymbol{r} = (x, y, z)$. A close relationship exists to the reciprocal space investigated in X-ray and neutron scattering experiments. Here the displacement space $\boldsymbol{R} = (\Delta x, \Delta y, \Delta z)$ is investigated. This space can, in fact, be probed by NMR as well as when measuring the effects of particle diffusion [162, 163]. The Fourier space conjugate to displacement space is referred to as $\boldsymbol{q}$ space. Because such $\boldsymbol{q}$-space measurements are associated with particle motion, $\boldsymbol{q}$ may also be interpreted as the Fourier-conjugate variable to velocity. The $\boldsymbol{q}$ space can be investigated with spatial resolution for use of diffusion constants and velocity components as contrast criteria in NMR images [158].

It is possible to use different methods (or sequences) in order to obtain different information. The "*Gefi ortho*" pulse sequence acquires gradient echo 2D data sets. The method is used for fast experiments using small flip angle excitations. This allows fast imaging acquisitions without running into saturation problems, but it is sensitive to local susceptibility changes in the sample, which can reduce image resolution. Larger flip angles may result in improved T_1 contrast on heterogeneous objects. The sequence is shown in Figure 3.2.6.

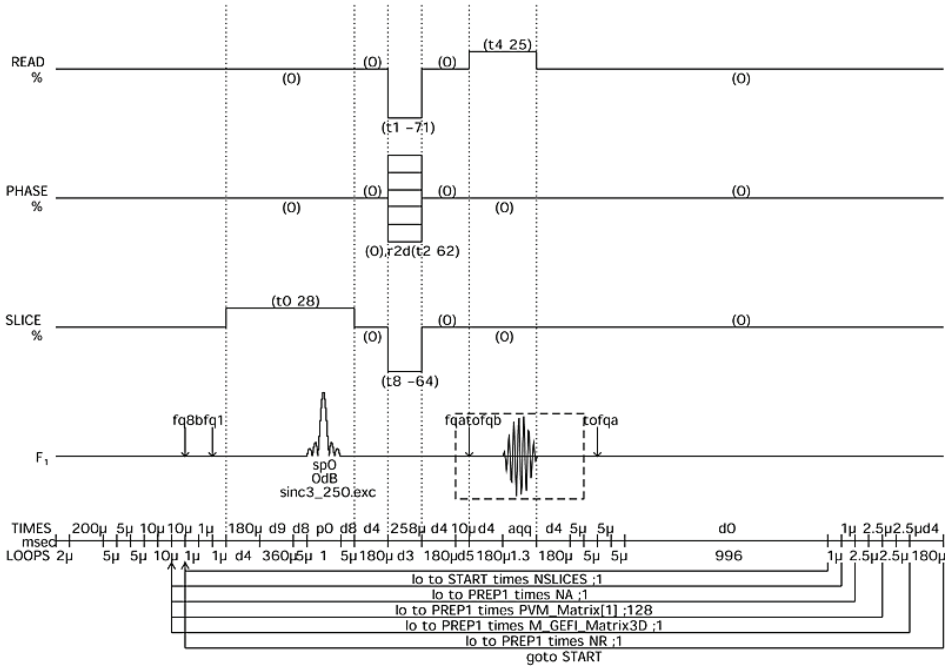

Figure 3.2.6: "*Gefi ortho*" sequence from Bruker Biospin MicroImaging Manual.

3.2.4 RHEO-IMAGING NMR

The imaging capability of NMR means that it can be used to measure local velocity profiles and molecular densities directly. The wide-ranging spectroscopic tools available to NMR also make it possible to measure molecular order and dynamics.

In this thesis the rheo-imaging NMR experiments have been carried out using a cylindrical Couette cell (9 mm inner radius, and 1 mm gap). This cell is integrated into an NMR microimaging probe for a wide-bore superconducting magnet. A schematic representation of the rheo-NMR cell inside the micro-imaging probe is given in Figure 3.2.7.

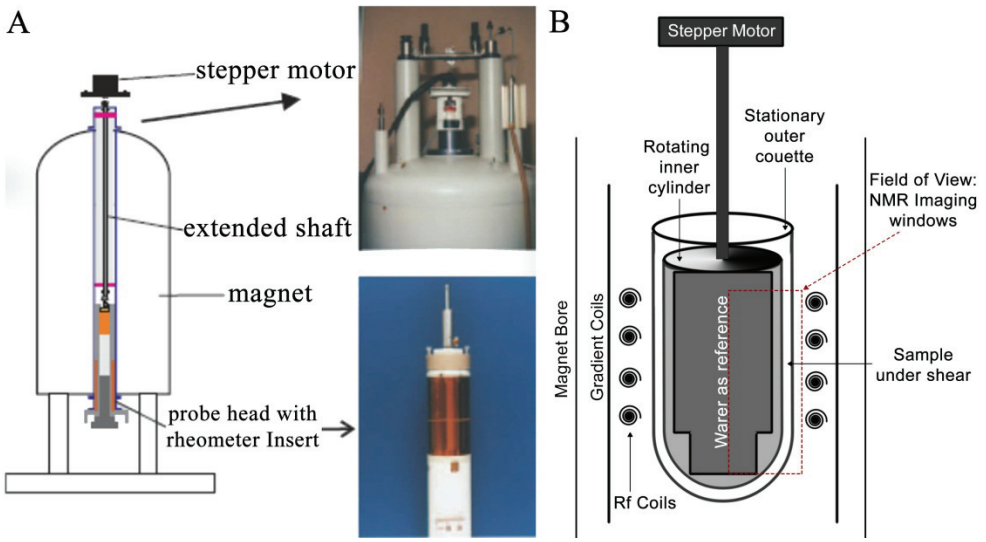

Figure 3.2.7: (A) A standard superconducting wide-bore magnet is shown with motor, driving shalt, rheometric device and Bruker microimaging probehead. (B) Schematic arrangements of the vertical cylindrical Couette cell.

The axis of the shear cell is aligned parallel to the magnetic field $\mathbf{B_0}$. Shear is applied by rotating the inner cylinder with an external stepper-motor gearbox assembly mounted on top of the NMR magnet. "*Gefi ortho*" images have been acquired (using the NMR sequence shown in Figure 3.2.6) under shear flow. In particular special sequence called flow compensated also has been used. By this sequence it is possible to avoid artifact due to the steady flow. This sequence is obtained by applying the pulsed field gradients to the normal "*Gefi ortho*" sequence. It is worthy to note that for our experimental conditions both sequences ("*Gefi ortho*" and flow compensated "*Gefi ortho*") lead to similar results such as images lacking artifacts.

3.3 SCATTERING TECHNIQUES

Scattering in general is a powerful non-invasive tool to prove the microscopic structure and dynamics of materials. In soft matter, X-ray, neutron and light scattering are widely used. An important advantage is that the measured quantities (dynamics, size, shape, molecular weight, specific volume or surface area etc.) are averaged over the whole sample. These quantities can be extracted from the scattering with almost no approximation or model [164]. The mathematical description is generally very similar for the different types of radiation.

Considering a radiation wave

$$\Phi_i(r,t) \equiv Ae^{\left[i(\mathbf{k_i}\cdot\mathbf{r}-\omega t)\right]} \qquad (3.3.1)$$

polarised perpendicular to the scattering plane, which is incident on a region of scattering medium; $\mathbf{k_i}$ is the propagation of the incident radiation, having magnitude $k_i \equiv |\mathbf{k_i}|=k=2\pi/\lambda$ where λ is the wavelength of the radiation in the medium; ω is the angular frequency. Radiation of the same polarization is scattered at angle θ to a detector in the far field.

We assume that the scattering is weak so that: (i) most particles radiation through the sample are undeviated, a few are scattered once, and the probability of double and higher-order scattering is negligible; (ii) the incident beam is not distorted significantly by the medium (first Born approximation). We also assume that the scattering process is "quasielastic", implying only a very small change in frequency. Thus the magnitude k_s of the propagation vector $\mathbf{k_s}$ of the scattering radiation is also $2\pi/\lambda$.

In order to compare results from experiments with different wavelength the scattering vector $\mathbf{q}$ is introduced. The scattering vector $\mathbf{q}$ describes the momentum transfer from the incident to the scattered radiation, i.e.

$$|\boldsymbol{q}| \equiv |\boldsymbol{k_s} - \boldsymbol{k_i}| = \frac{4\pi n}{\lambda_0}\cdot\sin\left(\frac{\theta}{2}\right) \qquad (3.3.2)$$

where $\mathbf{k_i}$ and $\mathbf{k_s}$ are the wave vectors of the incident and the scattered beam, respectively, n is the optical density (for scattering with light this is the refractive index) and λ_0 the vacuum wavelength of the incident radiation. For

elastic scattering $k_i = k_s = 2\pi n/\lambda_0$. In the case of neutron and X-ray scattering n becomes unitary. From Equation 3.3.2 it is obvious, that **q** is an inverse length and thus the length scales that are studied in a scattering experiment are inversely proportional to **q**.

Small-angle scattering (SAS) is a scattering technique based on the deflection of a beam away from the straight trajectory after it interacts with structures that are much larger than the wavelength of the radiation. The deflection is small (0.1-10°) hence the name small-angle. Small-angle scattering by particles can be used to determine the particle shape or their size distribution. A small-angle scattering pattern can be fitted with intensities calculated from different model shapes when the size distribution is known. If the shape is known, a size distribution may be fitted to the intensity.

We consider an experimental setup as sketched in Figure 3.3.1. A well collimated beam of radiation (light. neutrons, X-rays) with wavelength λ and intensity I_i is incident on a sample of thickness d. Most of the incident radiation is transmitted through the sample without any further interaction. Only a certain fraction of the incident beam is interacting with the sample and scattered at an angle θ > 0. In general, there is also an energy transfer between the sample and the incident beam (ΔE ≠ 0). A scattering experiment is thus observing the scattered intensity I as a function of scattering angle θ and energy E at a distance L away from the sample by using a convenient detection device. The measured 'scattering curve' I = f(θ, E) contains the complete information on the structural and dynamics of the sample.

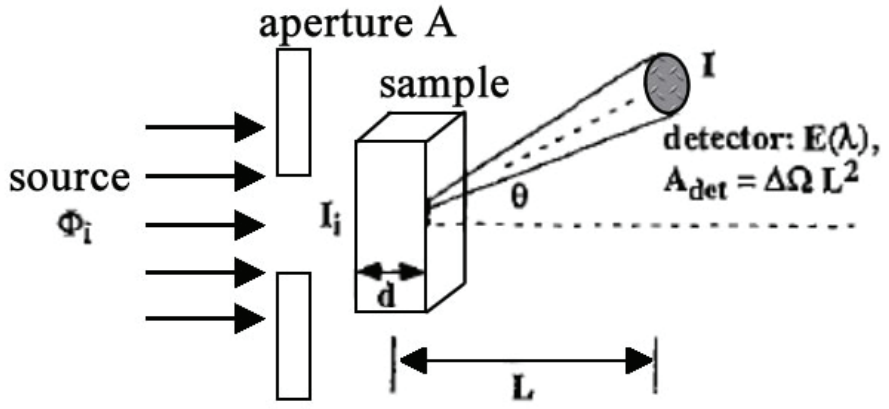

Figure 3.3.l: General layout of a scattering experiment. Radiation source with incident flux ϕ_i and wavelength λ_i, while sample aperture area is A.

A physical quantity needs to be defined in order to relate the intensity I = f(θ) measured in a scattering experiment to the sample's structure: the experiment consists in comparing the incident intensity I_i with the scattered intensity I, measured at an angle θ and a distance L on a detector with area $A_{det} = \Delta\Omega L^2$ (Figure 3.3.1). The incident intensity is attenuated on its way through the sample (thickness d) due to scattering and absorption (the sample's transmission T_s is then defined as the ratio of the outgoing over the incoming intensity at scattering angle θ = 0).

We call the ratio of the intensities as the differential scattering cross-section of the sample per unit solid angle, dσ/dΩ:

$$IL/I_i = d\sigma/d\Omega\left(cm^2\right) \qquad (3.3.3)$$

Normalization to unit sample volume V (cm^3) yields the differential scattering cross-section per unit sample volume, a quantity in units of (cm^{-1})

$$\frac{d\sum}{d\Omega} = \left(\frac{1}{V}\right)\frac{d\sigma}{d\Omega} \qquad (3.3.4)$$

$d\sum/d\Omega$ represents the probability of a particle of the incident beam of being scattered out from the unit sample volume into the solid angle ΔΩ; it is identical to the 'Rayleigh ratio' used in light scattering. $d\sum/d\Omega$ is the quantitative representation of the interaction radiation-sample and it contains all information on the structure of the sample. Its evaluation in absolute units of (cm^{-1}) should be the first step of data reduction, before any further interpretation of the experiment.

It can be shown that the local measured differential scattering cross-section of a sample (for instance a solution of polymers in a solvent) can be decomposed into two terms

$$\frac{d\sum}{d\Omega} = \left(\frac{d\sum}{d\Omega}\right)_{coherent} + \left(\frac{d\sum}{d\Omega}\right)_{incoherent} \qquad (3.3.5)$$

The first term is **q** dependent and represents the interference of scattered waves at different nuclei. It thus contains the information on the structure in the system studied. The second term does not depend on **q** and it is considered as a (flat) background originating from the solvent and from the incoherent scattering of the substance. The part of the incoherent contribution

from the substance must be measured for some cases and subtracted before the coherent differential scattering cross-section (structure) is further analyzed [164, 165]. For the case of a dilute mixture of a deuterated species in a hydrogenous solvent, the small amount of incoherent scattering from ^2H is negligible. It is sufficient to subtract the solvent scattering. For the inverse case of a dilute mixture of protonated species in a deuterated solvent, we can distinguish several methods, for instance: (a) the level of incoherent scattering can be estimated by measuring the sample at highest possible scattering angles, because the coherent sample scattering becomes negligible at highest **q**. If the scattering curve levels off to a constant asymptotic value this can be used as a good approximation for the sample's internal background; (b) the measurement of a reference sample with no structure is another method to determine the internal background. The reference sample (e.g. a H_2O/D_2O mixture) should contain a mixture of ^1H and ^2H corresponding to the volume fractions Φ^1_H and Φ^2_H in the sample. This method requires precise chemical skills.

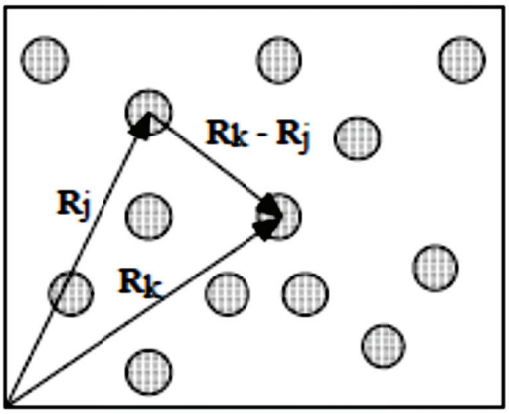

Figure 3.3.2: Co-ordinates for discrete scatters. Relative to an arbitrary origin, R_j is the position of the centre of mass of particle j.

Considering Figure 3.3.2 one can write for the small-angle scattering intensity:

$$\left\langle I(\boldsymbol{q})\right\rangle \simeq \left(\frac{d\Sigma}{d\Omega}\right)_{coherent} = \sum_{j=1}^{N}\sum_{k=1}^{N}\left\langle b_j(\boldsymbol{q})\,b_k^*(\boldsymbol{q})\,e^{\left[-i\,\boldsymbol{q}\left(R_j - R_k\right)\right]}\right\rangle \qquad (3.3.6)$$

where $\mathbf{R_j}$ is the position vector of the centre of mass of particle j in the scattering volume V_j, while $b_j(\mathbf{q})$ is the "scattering length" of particle. Assuming the particles as identical homogeneous spheres $b_j(\mathbf{q}) = b(q)$:

$$\left\langle I(q)\right\rangle = b^2(q)\sum_{j=1}^{N}\sum_{k=1}^{N}\left\langle e^{\left[-i\boldsymbol{q}\left(R_j - R_k\right)\right]}\right\rangle = Nb^2(0)P(q)S(q) \qquad (3.3.7)$$

P(q) is called the "form factor" of the particle. It is defined so that P(q) → 1 as q → 0 and provides information on the structure of the individual particles. Clearly, in a dilute system where particle positions are uncorrelated, hence cross terms i ≠ j, and S(q) = 1. S(q) is the static structure factor. The average intensities scattered by identical particles are the same, so that

$$\left\langle I(q)\right\rangle = N\left\langle\left|b(\boldsymbol{q})\right|^2\right\rangle = N\left\langle\left|b(0)\right|^2\right\rangle P(q) \qquad (3.3.8)$$

then

$$P(q) = \frac{\left\langle\left|b(\boldsymbol{q})\right|^2\right\rangle}{\left\langle\left|b(0)\right|^2\right\rangle} \qquad (3.3.9)$$

For a homogeneous spherical particle, the distribution of scattering material is uniform throughout the sphere, which means that the form factor for a sphere can be written

$$P(q) = \left[\frac{3}{(qR)^3}\left(\sin qR - qR\cos qR\right)\right]^2 \qquad (3.3.10)$$

where R is the sphere radius.

In the case of concentrated system

$$S(q) \equiv \frac{1}{N}\sum_{j=1}^{N}\sum_{k=1}^{N}\left\langle e^{\left[-i\boldsymbol{q}\left(R_j - R_k\right)\right]}\right\rangle \qquad (3.3.11)$$

The spatial correlations, or structure, in a concentrated system are usefully described in terms of the "radial distribution function", g(R), related to the probability of finding the centre of any particle at a distance R from the centre of a given particle.

$$S(q) = 1 + 4\pi\frac{N}{V}\int_0^{\infty}\left[g(R) - 1\right]R^2\frac{\sin qR}{qR}dR \qquad (3.3.12)$$

The strategy for measuring the structure factor is obtained from Eq. 3.3.6. Firstly one measures the intensity scattered by a sample dilute enough so that S(q) = 1. Then one measures the intensity scattered by the

concentrated sample of interest. The structure factor is then obtained from the ratio of these two measurements:

$$S(q) = \frac{\langle I(q) \rangle_{conc}}{\langle I(q) \rangle_{dil}} \frac{N_{dil}}{N_{conc}} \qquad (3.3.13)$$

The S(q) peak can be considered to be a "Brag reflection" from planes of particles separated by distances equal to the mean nearest-neighbour separation. Thus one finds that the positions R_{max} and q_{max} of the main peaks in g(R) and S(q) are related by an approximate "Brag condition" $q_{max}R_{max} \approx \pi$. For this reason it is often said that a scattering experiment, operating at scattering vector q, measures structure on a spatial scale $2\pi/q$. This is a useful rule, but it should not be taken too literally. In fact the value or S(q) at a particular scattering vector q is determined by the values of g(R) at all R.

3.3.1 Rheo-Small Angle Light Scattering (SALS)

Small-Angle Light Scattering (SALS) is a widely used technique for investigations of structures on a micrometer scale. The resulting scattering can be described by the formalisms presented in the Paragraph 3.3. Using polarized light offers the possibility to characterize anisotropic structures and the orientation with respect to the polarization plane of the incident beam. If polarization elements are used, two configurations are possible [164-167]: (1) Polarizer and analyzer are perpendicular (crossed polarizers). This so-called depolarized scattering is sensitive to orientation fluctuations, Figure 3.3.3A; (2) Polarizer and analyzer are parallel (parallel polarizers). This so-called polarized scattering is sensitive to concentration and orientation fluctuations, Figure 3.3.3B.

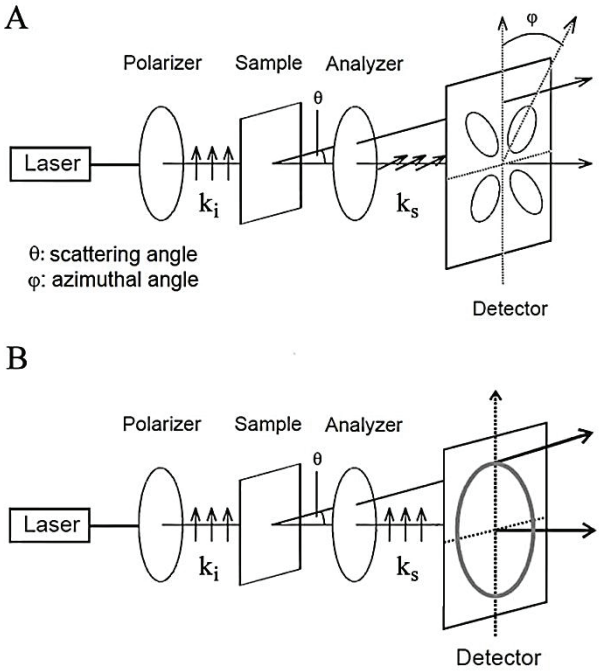

Figure 3.3.3: Different experimental setups for a SALS experiment. A) depolarized; B) polarized.

Without a polarizer, unpolarized scattering is observed, a superposition of both polarized and depolarized scattering.

The description of scattering from polarized SALS is not straightforward, since it depends on the difference of the radial polarizability of the scatterer and the polarizability of its environment. The latter is in most cases difficult to determine and small changes have drastic consequences for the calculated scattering pattern [168]. Depolarized small-angle light scattering is of particular use for the characterization of vesicles and a characteristic four-lobe cloverleaf pattern can be observed. This characteristic scattering pattern arises from the difference of the radial and tangential polarizabilities of the multilamellar vesicles MLVs. If the intensity distribution displays a maximum in the studied q-range, the size of the MLVs can be estimated by $R_{MLV} \approx 4.1/q_{max}$ [168, 169]. If these MLVs are sufficiently monodisperse they may arrange in a close packing and consequently a structure factor dominates the scattering. The size of the MLVs can very easily be extracted from the position of the first maximum of this structure factor by assuming that the MLV radius is half of the center to center distance. According to Braggs law $R = \pi/q_{max}$.

SALS can be used in combination with applied flow fields. However, a combination of a SALS setup with a rheometer (rheo-SALS) is more suitable for detailed investigations of complex fluid under shear flow [166, 167].

In this thesis rheo-SALS experiments were performed on the Anton Paar Physica MCR 301 with diode laser, supplying a wavelength of 658 nm. The beam passes through the cone-plate geometry along the gradient direction, thus yielding information in the flow-neutral-plane. An analyzer placed between the sample and the screen was used to obtain depolarized patterns. The setup is shown in Figure 3.3.4.

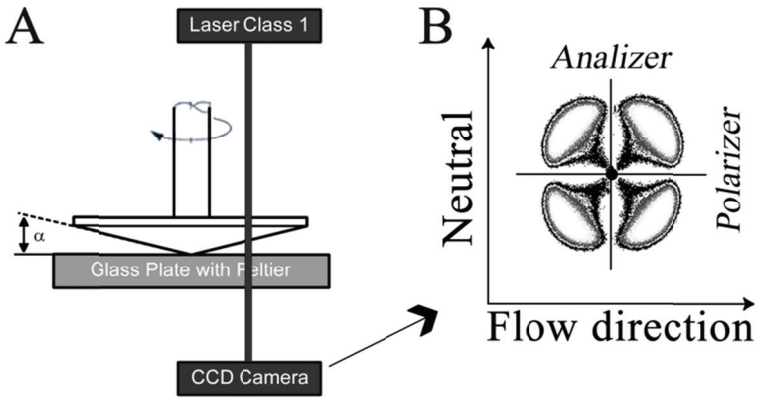

Figure 3.3.4: A) Schematic presentation of the rheo-SALS setup, with the cone-plate geometry. B) Example of MLVs SALS pattern recorded in the flow-neutral plane.

3.3.2 Rheo-Small Angle Neutron Scattering (SANS)

Small angle neutron scattering (SANS) is an ideal tool for studying the structure of materials in the mesoscopic size range between 1 and about 400 nm. Moreover SANS is a non-destructive method providing structural information averaged over all grains of different size with high statistical accuracy due to averaging over the whole sample volume.

The two main types of neutron sources are steady-state reactors and spallation sources. In steady-state sources neutrons are continuously produced by the fission processes. On the other hand, spallation sources provide a pulsed neutron beam and for this reason a time-of-flight method is used. The moderated neutrons at thermal energies have relatively short wavelength (< 1 Å). However, the neutron absorption cross-section varies relatively slowly with the neutron wavelength and neutron absorption in the

sample is usually not a problem. So in contrast to the situation for X-rays for which the absorption is very strong al long wavelengths, radiation with relatively large wavelengths (2-20 Å) can be used for neutrons far going to lower scattering vectors.

SANS experiments were performed at the SANS-I and SANS-II at Paul Scherrer Institut (PSI) in Villigen (Switzerland). The schematic representations of the instruments are shown in Figure 3.3.5.

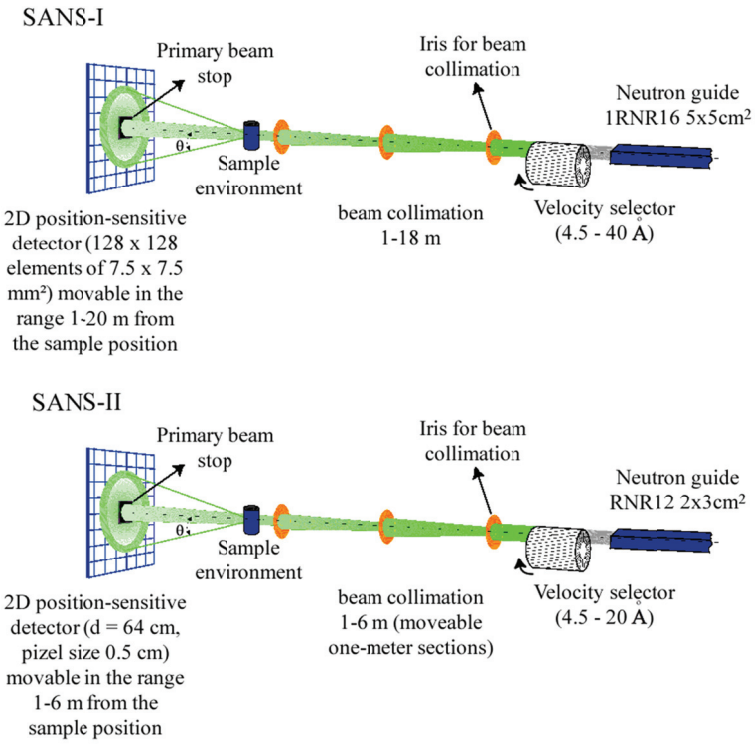

Figure 3.3.5: Schematic view of the SANS-I and SANS-II instruments at SINQ facility (PSI).

Different sample environments are available at SANS-I and SANS-II. In this thesis rheo-SANS experiments were performed using the Anton Paar Physica MCR 501 rheometer equipped with a Couette quartz cell (gap of 1 mm) at SANS-I. Moreover the rheometer was mounted on a table x-y-z-ω positioning. On the other hand a shear cell (gap of 1 mm) has been used at SANS-II. In both case the neutron beam is transmitted to the Couette radially, through the cylinder centers, i.e. the scattering is observed in the plan expanded by the flow and the neutral directions perpendicular to the shear-gradient, Figure 3.3.6.

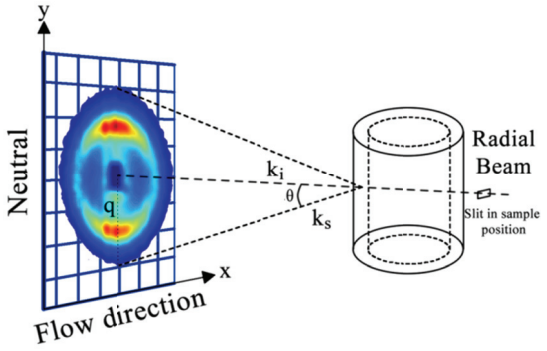

Figure 3.3.6: Schematic diagram of the rheo-SANS setup in the radial configuration.

The data have been corrected for background and empty cell scattering according to standard procedure. The background was determined using the method of a reference sample with no structure (e.g. a H_2O/D_2O mixture), that it should contain a mixture of ^1H and ^2H corresponding to the volume fractions Φ^1H and Φ^2H in the sample.

As mentioned in the Paragraph 2.1.1 it is possible to have different orientations of the lamellar phase under flow. The different orientations can be probed in situ by SANS technique using either radial (neutral-flow plane) or tangential (neutral-gradient plane) beam configurations. The three primary orientations have been labeled as "*a*", "*b*", and "*c*" based on the direction of the surface normal [51]. Literature data [73] report measurements made on planar lamellar phases under flow. In the radial beam position, the lamellae with a *c*-orientation do not contribute to the scattered intensity. In fact the intensity comes from the lamellar domains with *a*-orientation. To detect lamellae with the *c*-orientation, measurements in the tangential beam configuration should be performed. Hence the tangential beam is useful to distinguish between parallel and perpendicular orientations of the lamellae, Figure 3.3.7.

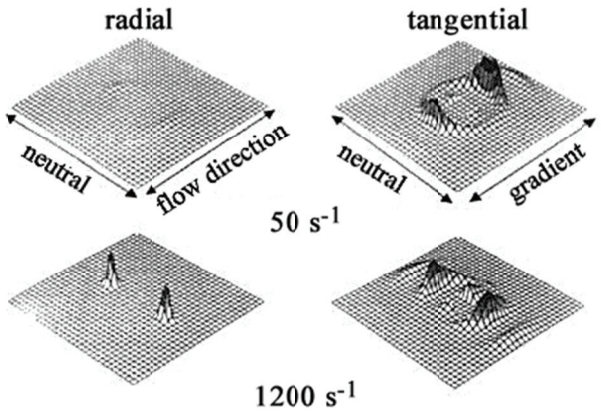

Figure 3.3.7: SANS patterns observed for a sample containing 30% of a polymer at shear rates of 50 s^{-1} (top) and 1200 s^{-1} (bottom). Left: radial beam, Right: tangential beam (from [170]).

On the other hand the radial beam is important for detecting the transition from lamellar to MLVs. The radial symmetry of the MLVs gives rise to an isotropic distribution of layer normal, as shown in Figure 3.3.8. Also, the SANS spectra showing symmetrical scattering could arise from either an isotropic solution or a powder crystalline phase. For this reason the rheo-SALS or rheo-NMR experiments can confirm the MLVs presence.

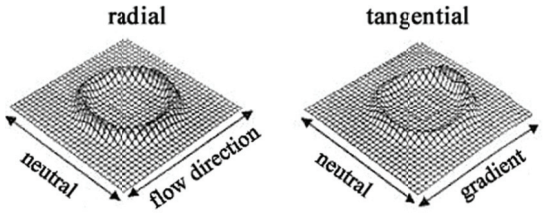

Figure 3.3.8: SANS patterns for a sample containing 21% of a polymer at a shear rate of 1 s^{-1}. Left, radial beam; right, tangential beam (from [170]).

4 RESULTS AND DISCUSSION

4.1 SHEAR EFFECTS IN C_nE_m SURFACTANT SOLUTIONS

The static phase diagrams of several nonionic surfactants in water have been studied by Mitchell et al. [106] and Jonströmer and Strey [110]. They show a fascinating variety of phase behavior (see Paragraph 2.4). In many nonionic surfactant systems of the C_nE_m type, a lamellar phase exists over a wide temperature and concentration range, which on its part hosts one region where MLVs can be formed by shear. Another region where shear causes a transition from MLVs to planar lamellae, is close to the upper temperature boundary and neighbored by the L_3 phase. This qualifies nonionic surfactants as model systems, since a reproducible initial state with a defined orientation can be obtained by simply shearing the sample close to the upper temperature phase boundary of the L_α phase. Moreover the simplicity of the binary mixture allows the correlation between the "static" phase (at rest) and the "dynamic" phase (under shear).

In this thesis the MLV formation has been investigated in three different C_nE_m/water systems. The knowledge about the lamellar-to-MLVs transition in these systems allows constructing a model that it is useful to understand what are the conditions under which the transition occurs. Moreover the thesis is focused on other phase transitions under shear flow, for instance the inverse transition MLVs-to-lamellar.

4.1.1 $C_{12}E_3/D_2O$ SYSTEM UNDER SHEAR FLOW

The system $C_{12}E_3/D_2O$ at the surfactant concentration of 50wt% shows a lamellar phase, Figure 2.4.2. Using a transient experiment (Paragraph 3.1.4) the typical transient viscosity behavior of MLV formation has been observed at the fixed shear rate of 10 s^{-1}, Figure 4.1.1. Depolarized SALS patterns (Paragraph 3.3.1) and rheological data have been recorded simultaneously. These results from a rheo-SALS experiment performed at 34°C are shown in

Figure 4.1.1. Initially the viscosity is low, as expected for a parallel orientation of planar layers, which is confirmed by the depolarized SALS pattern that also show a finger print of a lamellar phase [9]. The viscosity increases immediately and after about 700 s the slope of viscosity versus time changes and a small reproducible plateau is observed, as found for $C_{10}E_3$ at 300 s [7, 73]. At the plateau the SALS scattering intensity is mainly found in the neutral direction. This pattern in depolarized rheo-SALS set-up, suggests that there is a continuous structure in the flow direction, while the refractive index is modulated perpendicular to the flow. The same pattern has been already observed in previous studies by Zipfel et al. [7] and Nettesheim [9], who explained this scattering with multilamellar cylinders (MLCs) structure. After this intermediate plateau region, the viscosity continues to increase and the SALS pattern evolves into a four-lobe pattern (1700 s), a characteristic signature of MLVs [5, 73]. At 2500 s a strong structure factor intensity is observed indicating a narrow MLV size distribution [170, 171].

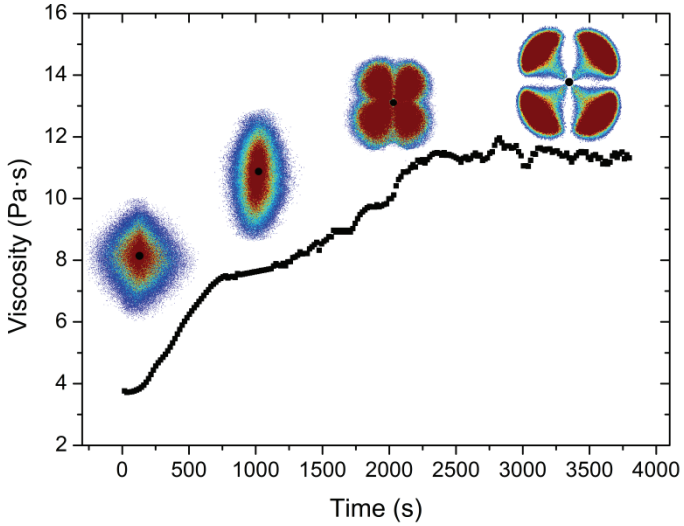

Figure 4.1.1: Transient viscosity vs. time during the MLV formation at 10 s^{-1}. Depolarized SALS patterns obtained at four different times are shown above the viscosity curve. The two-dimensional scattering pattern in the flow-neutral plane was visualized.

Figure 4.1.2 reports the steady-state viscosity and the shear stress as a function of the $\dot{\gamma}$ within 0.1–100 s^{-1} range at 34°C. The shear rate dependence of the viscosity has been divided into three regions. In region I, the first shear-thinning appears at lower shear rate. This regime corresponds to the orientation or alignment of the lamellar phase in the flow direction. In region II, a shear-thickening appears between 0.5 and 2.0 s^{-1}, while at high shear rates (region III) there is again a shear-thinning, which can be described by a

power law relation $\eta \propto \dot{\gamma}^{-0.75\pm0.05}$ or $\sigma \propto \dot{\gamma}^{0.26\pm0.05}$. Similar value of the exponent has been obtained by Fujii and Richtering [172]. Investigating the $C_{10}E_3/D_2O$ system, Fujii and Richtering [172] suggested that the MLVs in the shear thickening regime (region II) are "imperfect-MLVs" respect to densely packed-MLVs in the shear-thinning regime (region III). In present study, we observed similar rheological results for $C_{12}E_3/D_2O$ system, consequently the same interpretation of the experimental data can be used.

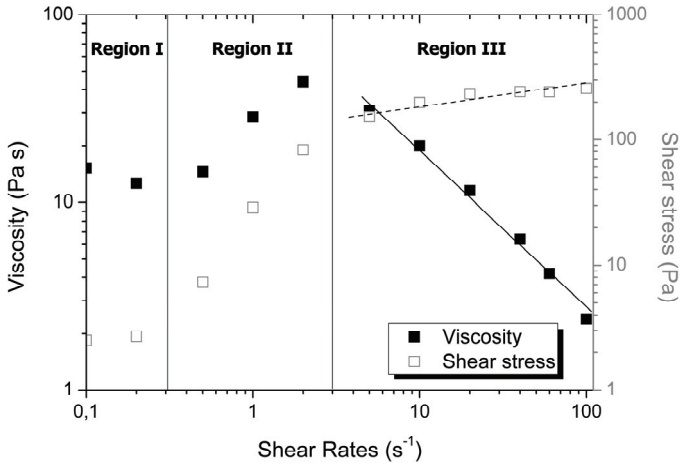

Figure 4.1.2: Log-log plot of the steady-state shear stress and viscosity as a function of the shear rate. The data are obtained using a Couette geometry. The solid and dotted lines show a power law relation.

The radii of the MLVs formed at 10, 20 and 40 s^{-1} can be estimated from the position of the maxima of the intensity distribution in the SALS patterns (Figure 4.1.3A). For the densely packed MLV state, the relative maximum intensity corresponds to a structure factor peak. Kosaka et al. [76] recently suggested a FCC packing of the MLVs and the observed structure factor peak would correspond to the strong 111 reflection, with which we obtain $R_{MLV} = 3.9/q_{MAX}$. R_{MLV} values, calculated by using this equation are plotted in Figure 4.1.3B as a function of the shear rate. Roux et al. [1, 90] have reported for different systems the following shear thinning law

$$R_{MLV} \simeq \sqrt{\frac{4\pi\left(2\kappa+\bar{\kappa}\right)}{\eta_s d\dot{\gamma}}} \approx c\dot{\gamma}^{-0.5} \qquad (4.1.1)$$

where η_s is the solvent viscosity and the others parameter are defined in the chapter 2. Figure 4.1.3B shows the shear thinning law

$R_{MLV} \approx c\dot{\gamma}^{-0.5} = 3.5 \cdot 10^{-6} \dot{\gamma}^{-0.5}$ (dashed line) which gives a reasonable description of the data.

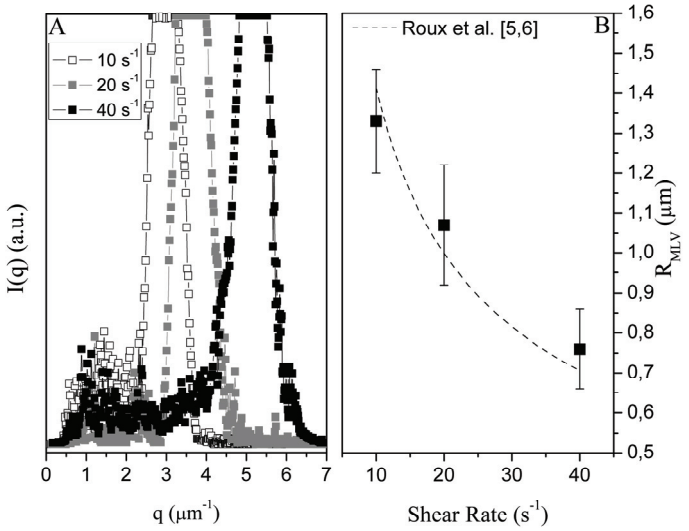

Figure 4.1.3: (A) Comparison of the radial intensity distribution of the scattering patterns recorded in depolarized SALS for shear rates of 10, 20 and 40 s^{-1}. All data are recorded at 30000 strain units. (B) The radii of the MLVs is plotted vs. shear rate, the dotted line represents the relation given by Roux et al. [1, 90].

Other details are given in the article "Rheological and Rheo-SALS investigation of the MLV formation in $C_{12}E_3/D_2O$ system" accepted by Journal Colloid and Interface Science (JCIS) as a communication (***Paper I***).

4.1.2 $C_{12}E_5/D_2O$ SYSTEM UNDER SHEAR FLOW

The system $C_{12}E_5/D_2O$ at the surfactant concentration of 40wt% shows a lamellar phase in a wide range of temperature, Figure 2.4.3. Figure 4.1.4 shows the typical transient viscosity behavior of MLV formation at 1 s^{-1}. SANS patterns and rheological data have not been recorded simultaneously. These scattering patterns come from rheo-SANS-II (PSI) and they are performed at 55°C using a shear cell (Paragraph 3.3.2). The observed peak structure factor at lower strain arises likely from a minor population of bilayers with *a*-orientation [51]. However according to the reference [72], the *a*-orientation is attributed to a metastable state and it is reasonable to affirm that part of the

bilayers is in *c*-orientation. The first plateau of viscosity in Figure 4.1.4 (after 600 s) is ascribed to elongated objects oriented along the flow in the steady state (typical oily streaks) as observed by C.-Y.D. Lu et al [174] for a 45wt% $C_{12}E_5$/water system.

The increase of viscosity in the region 0-600 s is due to the increase of density and size of defect loops in the steady-shear condition. The increased defects play a crucial role in shear-induced structural transformations, because a perfectly ordered and oriented lamellar state should not be able to store elastic energy, when sheared parallel to the bilayers [175, 176]. In fact the pronounced increase of viscosity due to MLV formation occurs within 1500-3000 s. The MLVs are formed after 3000 strain units. SANS patterns change from the anisotropic to the isotropic ring. These changes of scattering patterns demonstrate the formation of the isotropic onions. At γ = 6000 a steady state is reached.

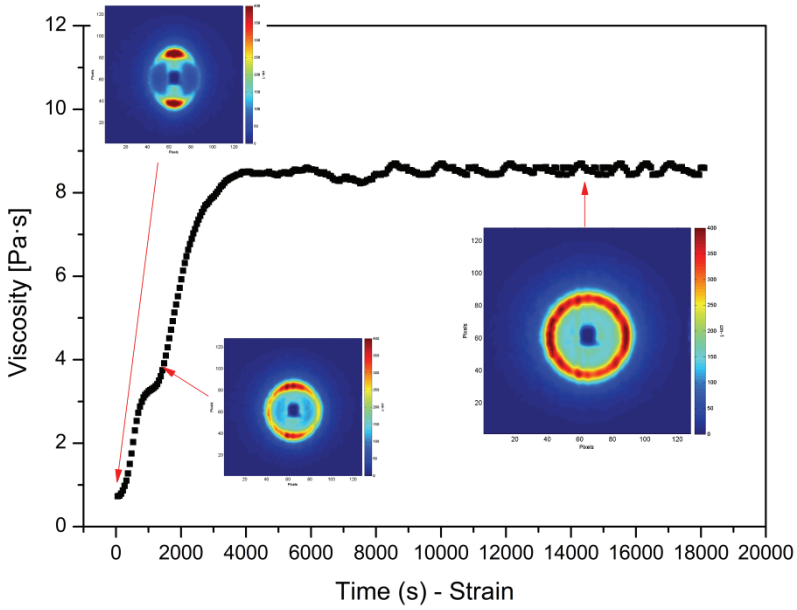

Figure 4.1.4: Time evolution of the transient viscosity at the shear rate of 1 s^{-1} (strain controlled instrument) and relative SANS patterns at 55°C. The transition from lamellar (0 s) to MLVs (3000 s) appears after a small plateau region that it is attributed to the elongated objects oriented along the flow in the steady state

As mentioned in the Paragraph 3.3.2, the SANS spectra showing symmetrical scattering could arise from either an isotropic solution or a powder crystalline phase. On the other hand a powder crystalline phase gives a powder pattern in ^{2}H-NMR spectrum (Paragraph 3.2.1). Consequently the MLV formation is confirmed by rheo-NMR experiments (Figure 4.1.5). In fact

the doublet of the planar lamellae turns into a broad single peak as a consequence of the MLVs presence [171].

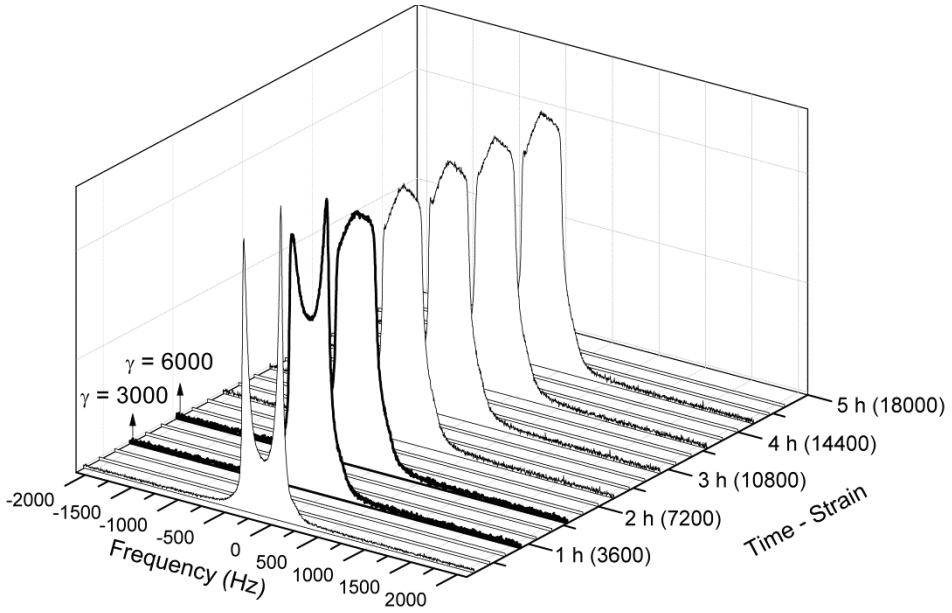

Figure 4.1.5: Time evolution of ^{2}H-NMR spectra during the MLV formation from planar lamellae at 55°C and a constant shear rate of 1 s^{-1}.

In general the shear rate promotes the formation of densely packed aggregates whose size is affected by the applied shear rate value. High shear induces small MLVs aggregates formation and consequently good stability of structure phase [177, 178]. It is worthy to note that the MLV phase in 40wt% $C_{12}E_5/D_2O$ at 55°C covers a narrow stability region between 1 to 10 s^{-1}. After 10 hours at 20 and 40 s^{-1}, a significant decrease in viscosity appears. This is due to the reverse transition from MLVs to planar lamellae as evidenced by rheo-^{2}H NMR. Figure 4.1.6 shows ^{2}H-NMR spectra under 40 s^{-1} shear rate as a function of time. A broad single peak typical of MLVs turns into the Pake doublet of the planar lamellae after 10 hours according to the rheological results.

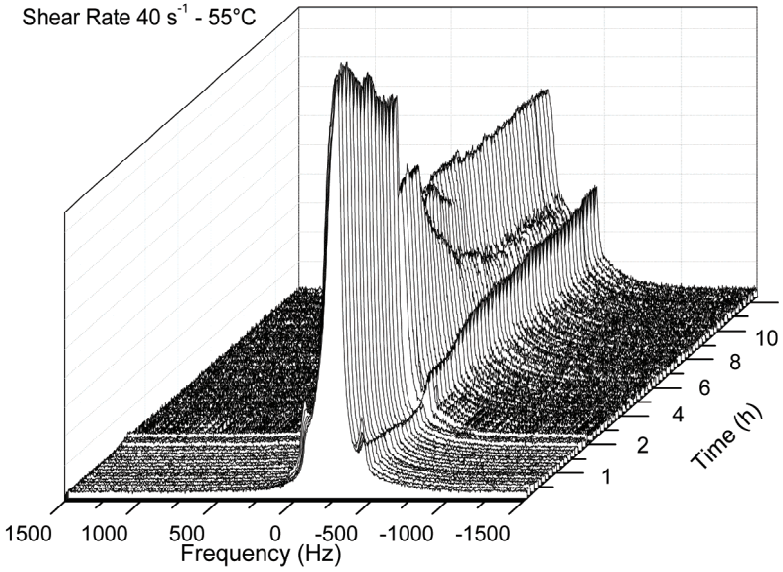

Figure 4.1.6: Time evolution of ^{2}H-NMR spectra during the transition from MLVs to planar lamellae at 55°C and at constant shear rate of 40 s^{-1}.

The shear-induced MLVs-to lamellar transition can qualitatively be described by a balance between shear rate and monolayer spontaneous curvature, H_0. The shear and the spontaneous curvature have competitive effects. In this case the shear effect overcomes the lower spontaneous curvature [179], leading to MLV formation. When the MLV aggregate reaches the critical size (at high shear rates), the closed bilayer structure is not retained anymore. Low viscous oriented lamellar structures are present when the layer is normal to the direction of the flow with low defect density (Figure 4.1.7).

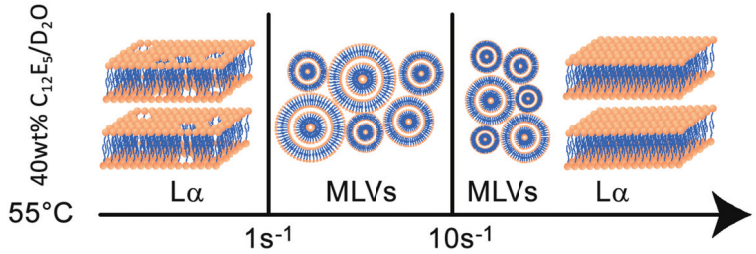

Figure 4.1.7: Isothermal dynamic phase diagram of a 40 wt% $C_{12}E_5/D_2O$ system at 55 °C.

At higher shear rate, 60 s^{-1}, a unusual transient viscosity of the system is observed. By using rheology, ^{2}H-rheo-NMR and rheo-SALS we related this atypical behavior to the instability of MLVs (Figure 4.1.8). The formed MLVs at low strain become unstable at higher strain. The SALS patterns and NMR

spectra sequences clearly show the following structural evolution: L_α-MLVs-L_α. Moreover the viscosity trends for Couette and cone plate geometries are similar. Figure 4.1.8 shows viscosity profile obtained by Couette geometry.

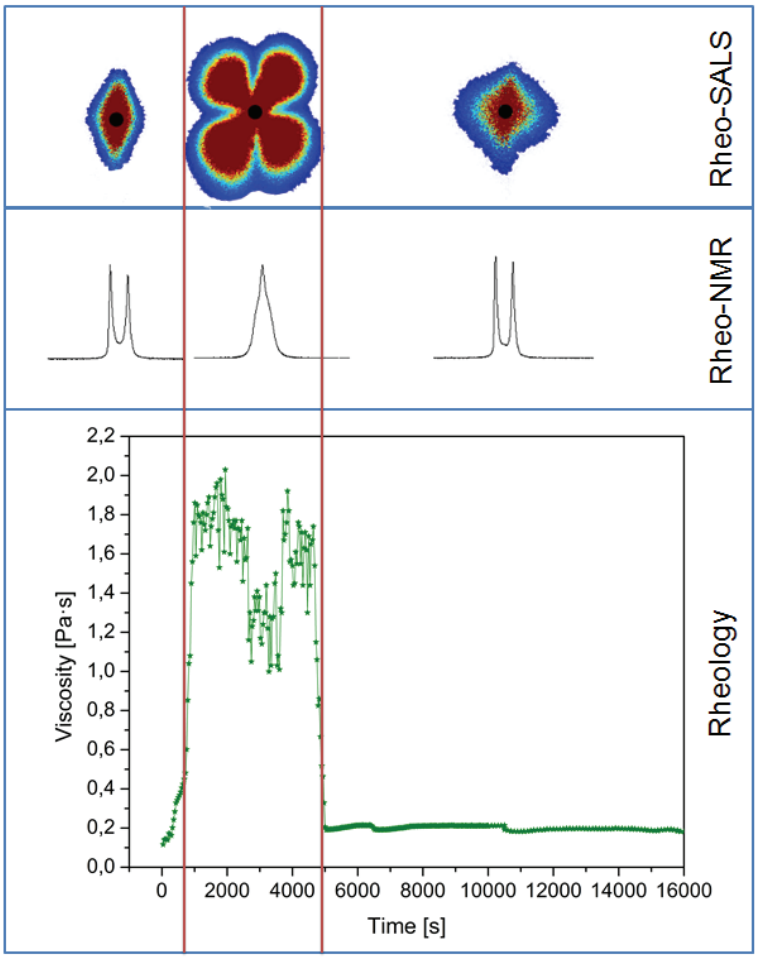

Figure 4.1.8: Time evolution of the transient viscosity at a shear rate of 60 s^{-1} and relative rheo-SALS patterns and rheo-^{2}H NMR spectra at 55°C.

Further details are given in the letter "Effect of the shear rates on the MLVs formation and MLVs stability region in $C_{12}E_5/D_2O$ system: Rheology, Rheo-NMR and Rheo-SANS experiments" Langmuir, 2011, 27, 2088–2092 (***Paper II***).

4.1.3 $C_{16}E_4/D_2O$ SYSTEM UNDER SHEAR FLOW

The system $C_{16}E_4/D_2O$ at the surfactant concentration of 40wt% shows a lamellar phase in the central of the phase diagram, Figure 2.4.4. Figure 4.1.9 shows the typical transient viscosity behavior of MLV formation at 0.5 s^{-1}. SANS patterns and rheological data have not been recorded simultaneously. These scattering patterns come from rheo-SANS-II (PSI) and they are performed at 55°C using a shear cell (Paragraph 3.3.2). The typical viscosity evolution of the complete MLV formation [75] is reported. The increase in viscosity over time is remarkable and it corresponds to a significant thickening behavior.

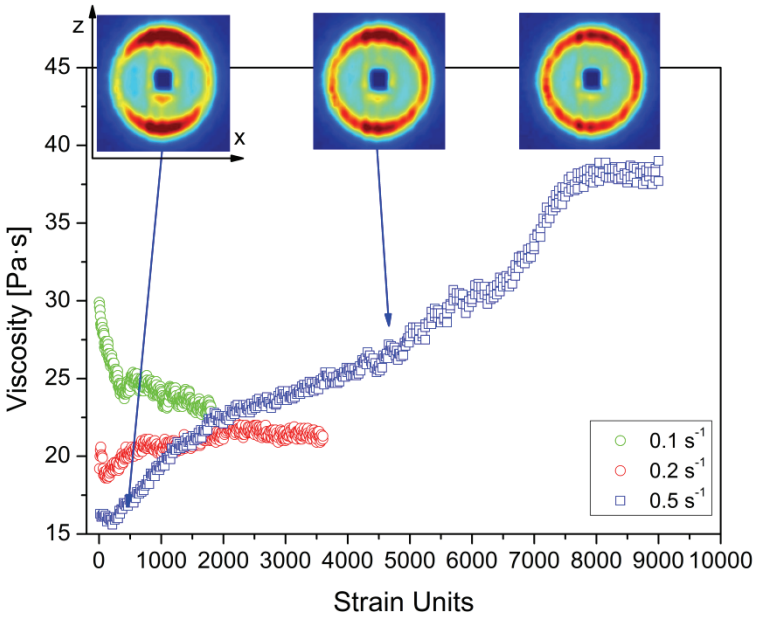

Figure 4.1.9: Transient viscosity under constant shear rates of 40 wt% $C_{16}E_4$ sample at 55°C and relative SANS patterns for the transient viscosity obtained at 0.5 s^{-1} at different times (strain units). Anisotropic 2D-scattering patterns have been recorded in vorticity-flow (z-x) plane.

SANS spectra in the radial direction have been recorded at intervals of 180 s with an acquisition time of 1 s. After 360 seconds (180 strain units) a pronounced anisotropic scattering is observed (Figure 4.1.9). SANS patterns change from the anisotropic pattern to the isotropic ring. These changes clearly demonstrate the formation of the isotropic MLVs. In fact the pronounced increase of viscosity due to the mechanism of MLV formation, occurs between 4000 and 9000 strain units. We consider the steady state reached at γ = 8000. SANS experiments have been performed at low shear rates within the q-range 0.02 $Å^{-1}$ < q < 0.15 $Å^{-1}$ where the first order Bragg

peak, observed at q ≈ 0.09 $Å^{-1}$, corresponds to the bilayer spacing (d) of 6.9 nm. On the other hand at 40°C a bilayer spacing of 7.2 nm is observed and this temperature dependence behavior of d-spacing is similar to the data on $C_{16}E_6/D_2O$ found by Penfold et al. [179].

In Figure 4.1.10 the ^2H NMR line shape of heavy water in MLV system at 55°C is analyzed quantitatively as reported in literature [73]. In first approximation the MLV radius can be determined from the line shape simulation and it is around 3 μm. A quadrupolar splitting of 480 Hz has been measured. The d-spacing of the bilayer is determined by SANS profile measured without shear rate, d = 6.9 nm. Taking into account the approximations introduced, further investigations are needed to determine the exact MLV radius.

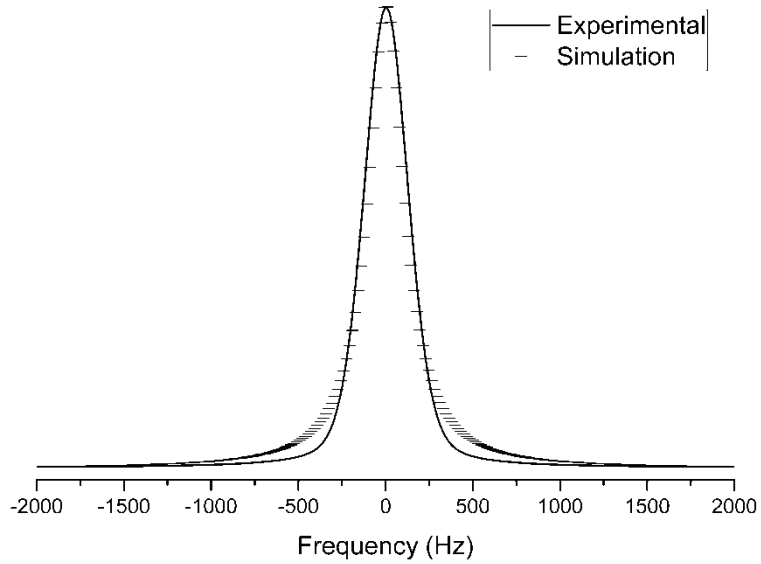

Figure 4.1.10: The Lorentzian line shape simulation on the broad NMR peak of the MLVs. The broad peak has been recorded at 8000 strain units (shear rate 0.5 s^{-1}).

The time-dependent transient viscosity for a 40wt% $C_{16}E_4/D_2O$ system measured at 40°C is shown in Figure 4.1.11. The viscosities have been measured applying different shear rates. It is remarkable to note: (i) high viscosities at low shear rates, in comparison with other C_nE_m surfactants [75]; (ii) a significant increase in viscosity is observed at shear rate of 0.5 s^{-1}.

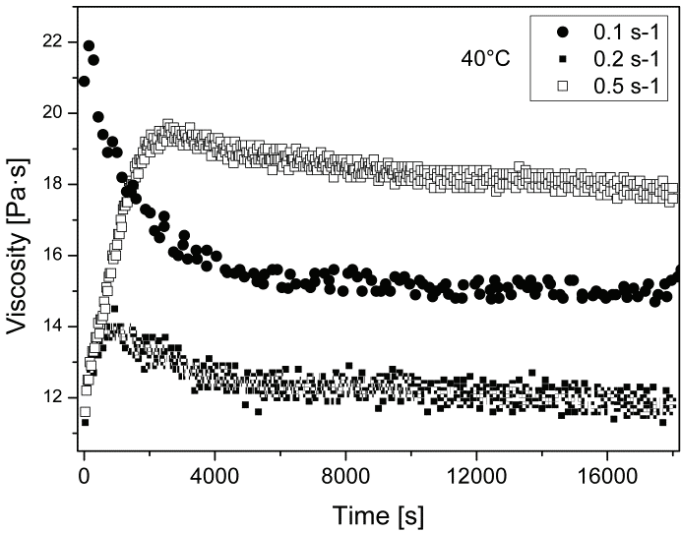

Figure 4.1.11: Transient viscosity under constant shear rates (0.1, 0.2 and 0.5 s^{-1}) of 40 wt% $C_{16}E_4/D_2O$ system at 40°C.

The small increase of viscosity may be interpreted in terms of coexistence of MLV and lamellar phases. The MLV formation is further confirmed by rheo-NMR experiments shown in Figure 4.1.12. In fact the characteristic "Pake" doublet of the planar lamellae turns into a broad single peak as a consequence of the MLVs presence [6, 171]. After 30000 s under shear rate of 0.5 s^{-1} no substantial modifications have been observed on the spectra as it is possible to see in the inset B in Figure 4.1.12. Moreover the NMR line shape of the spectra seems to confirm the MLV and lamellar phases coexistence.

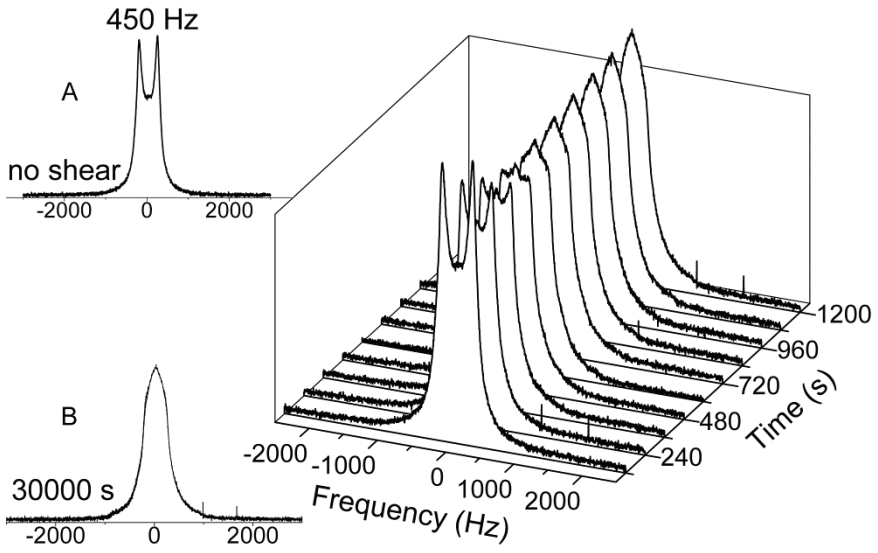

Figure 4.1.12: Time evolution of ^{2}H-NMR spectra during the MLV formation from planar lamellae at 40°C and at constant shear rate of 0.5 s^{-1}. The inset A shows the powder pattern of the lamellar phase with no shear applied. The inset B shows a broad peak attributed to MLV and lamellar phases coexistence after 30000 s under shear rate of 0.5 s^{-1}.

Depolarized small-angle light scattering were carried out simultaneously with viscosity measurements (Paragraph 3.3.1) at 40, 45 and 55°C. The scattering patterns were recorded after 20000 strain units of the transient experiments at 10, 20 and 40 s^{-1} (Figure 4.1.13), when the steady state was already reached. At 40°C there are patterns known as cloverleaf, corresponding to the form factor of MLVs [9]. This result suggests that the MLVs are not densely packed at 40°C. Depolarized scattering evolves at 45°C revealing a typical four-lobe structure factor [9]. The development of the structure factor is an indication that the MLV size distribution became narrow causing an increasing order [171]. By increasing the shear rate the maximum intensity in the four-lobe pattern is observed at higher q. This pinpoints the shear rate dependence of the MLV size, and confirms that the observed shear-thinning behavior is caused by a decrease in the MLV radius.

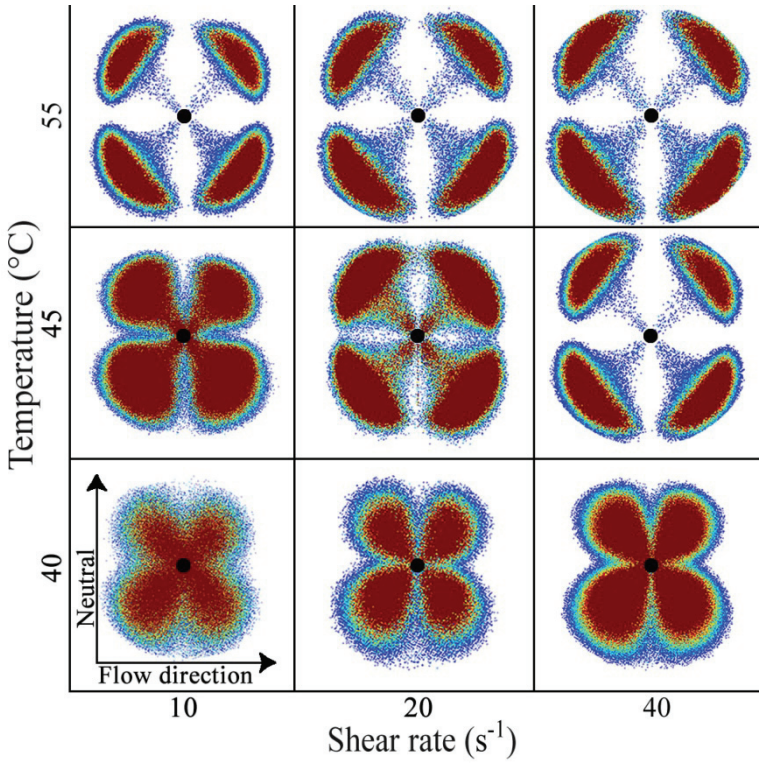

Figure 4.1.13: Comparison of the evolution of scattering patterns recorded in depolarized SALS for shear rates of 10, 20 and 40 s^{-1} and temperatures of 40, 45 and 55°C.

The Figure 4.1.14 reports the MLV size calculated from the rheo-SALS patterns. We have used two different relations in order to estimate the MLV radii. In the case of the form factor cloverleaf the MLV size was determined by the relation $R_{MLV} \approx 4.1/q_{MAX}$ [76], where q_{MAX} corresponds to q value where the scattered intensity reaches its maximum. This relation has been used in the

determination of spherulite sizes in films and semicrystalline polymers [169]. In the case of the four-lobe structure factor pattern, the radii of the MLVs were estimated according to the relation $R_{MLV} = 3.9/q_{MAX}$. By fitting the data, we obtained a deviation from $R_{MLV} \sim \dot{\gamma}^{-0.5}$, given by Roux et al. [90]. The deviation has been also reported for other systems [9]. In fact the calculated fitting gives the following relation $R_{MLV} \sim \dot{\gamma}^{-0.26}$.

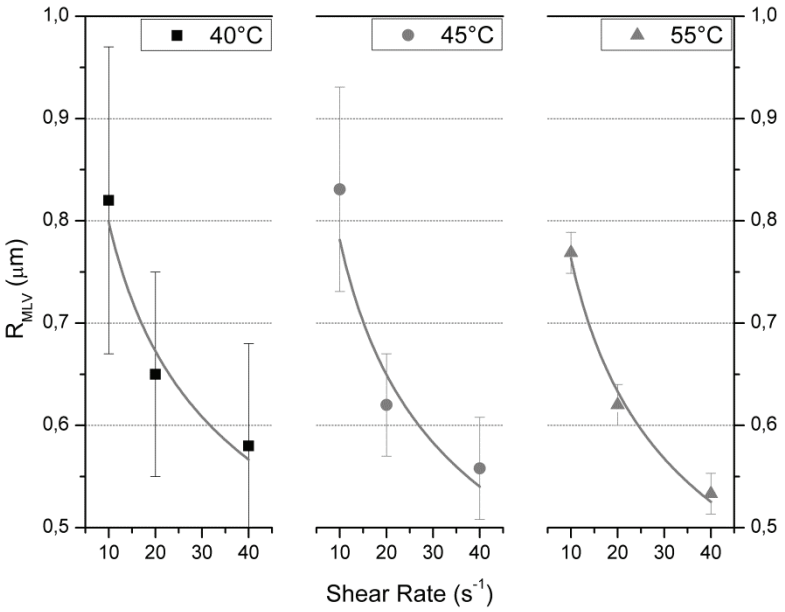

Figure 4.1.14: R_{MLV} obtained from the position of the intensity maximum of the depolarized SALS patterns is plotted vs shear rates.

Characteristic 2D-SANS patterns with radial beam configuration observed for a $C_{16}E_4/D_2O$ binary system are shown in Figure 4.1.15. Within the lamellar phase of the $C_{16}E_4/D_2O$ system (40 wt%), and through the use of the shear cell at the SANS-II instrument, we have mapped out the relative stability of MLVs and planar lamellae as a function of temperature and shear rate (Figure 4.1.15). One aspect that we would like to point out is that the MLV pattern at 45°C is not perfectly isotropic, but has a slight texture revealed by higher scattering intensities in the flow and neutral directions. More investigations will be needed in order to understand the nature of the MLV state. Anyway, it is reasonable to assume that they are densely-packed, maybe slightly deformed or partially ordered in a packing state, with some similarity to the $C_{12}E_4$ system, where a clear hexagonal packing of the MLVs has been observed [180].

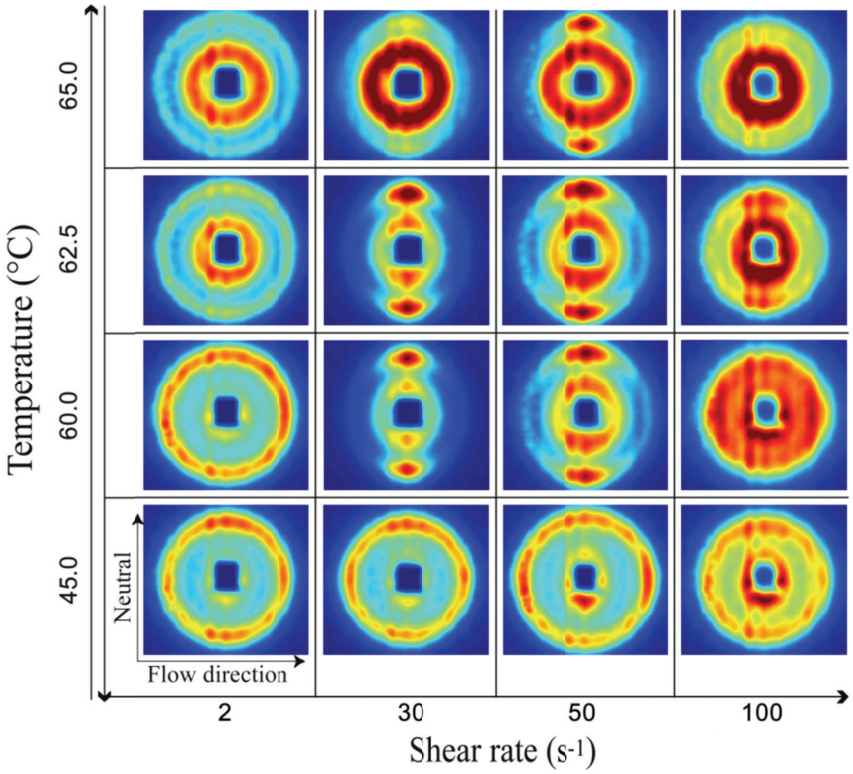

Figure 4.1.15: Steady-state scattering patterns as a function of temperature and shear-rate for 40 wt% $C_{16}E_4$ in D_2O.

In Figure 4.1.16 the most relevant patterns of the temperature scans under constant shear rate of 30 s^{-1} are shown. As the temperature is increased from 45 to 60°C, Figure 4.1.16A and 4.1.16B respectively, we observed the MLV to planar lamellae transition. At 60°C there is also a small peak at lower q that seems to indicate the formation of a second lamellar phase with a larger spacing (L_α^+) coexisting with the normal lamellar peak at larger q. The intensity of the L_α^+ peak increases at 62.5°C and 65°C at the initial time (until it turns into a L_3 phase), Figure 4.1.16C and Figure 4.1.16D respectively. Hence, the formation/nucleation of the L_3 phase induced by temperature and shear, seems to evolve through the formation of an intermediate lamellar phase of larger d spacing (L_α^+) in coexistence with the initial short d spacing (L_α). The coexistence between two equilibrium lamellar spacings in binary systems is a very rare phenomenon [181-183] as it implies a very fine balance between attractive and repulsive forces. By increasing temperature, the sponge phase is favored, Figure 4.1.16F. The L_α^+ would thus correspond to a sponge phase that is destroyed by the shear field. As the temperature keeps increasing, the bilayer curvature decrease, favoring a sponge phase again and this fine balance of curvature and shear field leads to our results.

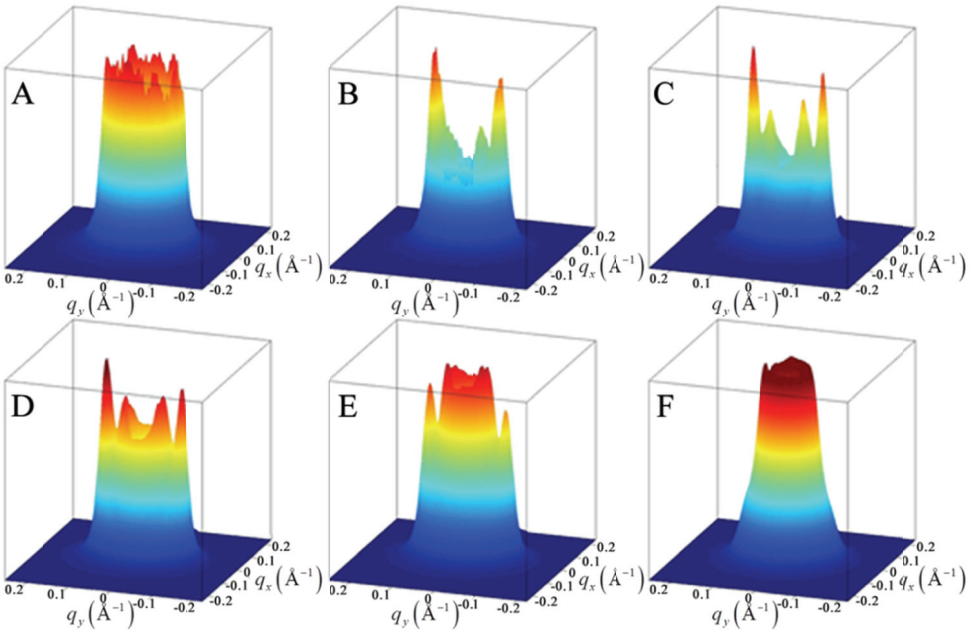

Figure 4.1.16: 3D-SANS patterns detected in the radial beam configuration during a temperature scan from 45°C to 65°C under constant shear rate of 30 s^{-1}. (A) T = 45°C; (B) T = 60°C; (C) T = 62.5°C; (D), (E) and (F) T = 65°C. The color scale gives the SANS intensity, I(q). All patterns have the same fixed color scale.

The same picture can be obtained at 50 s^{-1} as temperature is increased. Figure 4.1.17 shows the SANS data intensity along the flow (q_x) and neutral (q_y) directions. The superposition of the q-dependent scattered intensity provides clear evidence of symmetrical (isotropic) or asymmetrical scattering. In Figure 4.1.17A, the scattering curves in both directions overlap one another, giving a symmetrical scattering pattern due to the MLVs state. Figure 4.1.17B reveals two peaks in the neutral direction at low and high q, while there are no peaks in the flow direction. This scattering pattern is due to L_α^++ L_α coexistence. The sponge phase is started to be favored at 65°C, Figure 4.1.17C, but it is not a steady state. In fact Figure 4.1.17D reveals an isotropic structure factor peak at low q and in addition two peaks in the neutral direction at a low and high q. This corresponds to the two-phase coexistence where a L_3 phase (isotropic scattering) coexists with a lamellar phase.

Hence, at 50 s^{-1} the general observations taken from 30 s^{-1} are confirmed. Moreover, in this case the balance of curvature and shear field gives a L_3+L_α coexistence at 65°C, which means that increasing the shear rate the L_3 phase is not stable.

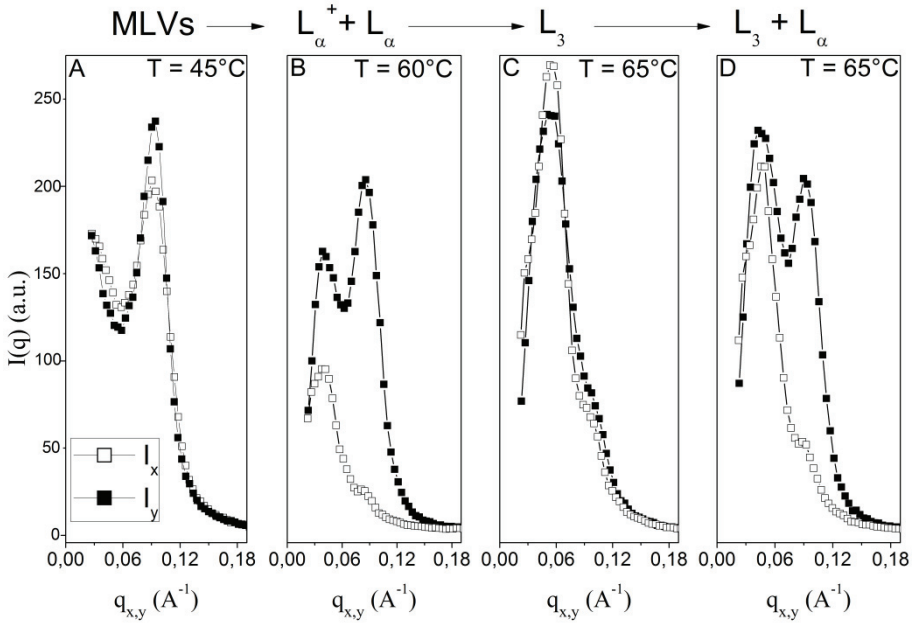

Figure 4.1.17: Representative SANS data collected during a temperature scan test between 45°C and 65°C. The data are from a 40wt% of $C_{16}E_4$ in D_2O sample measured under shear rate of $50s^{-1}$.

Figures 4.1.15, 16 and 17 show similar SANS patterns at 60°C, 30 and 50 s^{-1}. On the contrary a very different pattern is observed at 100 s^{-1} (Figure 4.1.15). An explanation of this interesting SANS pattern is the MLVs+L_3 phase coexistence. Considering the $L_\alpha^+ + L_\alpha$ coexistence at 30 and 50 s^{-1}, it is reasonable to affirm that the high shear rate of 100 s^{-1} induces the formation of the L_3 phase and at the same time keeps stable the MLVs (which are originated from L_α) at 60°C. Yasutaka Iwashita and Hajime Tanaka [184] have also reported a MLVs+L_3 coexistence for the $C_{10}E_3$/water system. Increasing the temperature the inverse transition MLVs-to-L_α is observed.

The final structure and deformation behavior of the 40% $C_{16}E_4$ in D_2O have been mapped out in a dynamic phase diagram as a function of temperature and shear rate, Figure 4.1.18. This dynamic phase diagram shows that the material undergoes three critical transitions: (i) lamellar–to-MLV transition wherein a densely packed MLV state can be formed; (ii) MLV-to-lamellar transition; (iii) lamellar-to-sponge transition and the relative competition with the reverse transition.

In the temperature range between 45°C and 60°C, at relatively low shear rates, a lamellar-to-MLV transition is observed. After 60°C the inverse MLV-to-lamellar transition appears under shear of 30 s^{-1}. At high shear rates and temperatures a competitive existence between lamellar and sponge phase is

observed. Finally a sponge phase is reached under shear, close to the boundary phase, between L_α+ L_3 and L_3 in the static diagram phase.

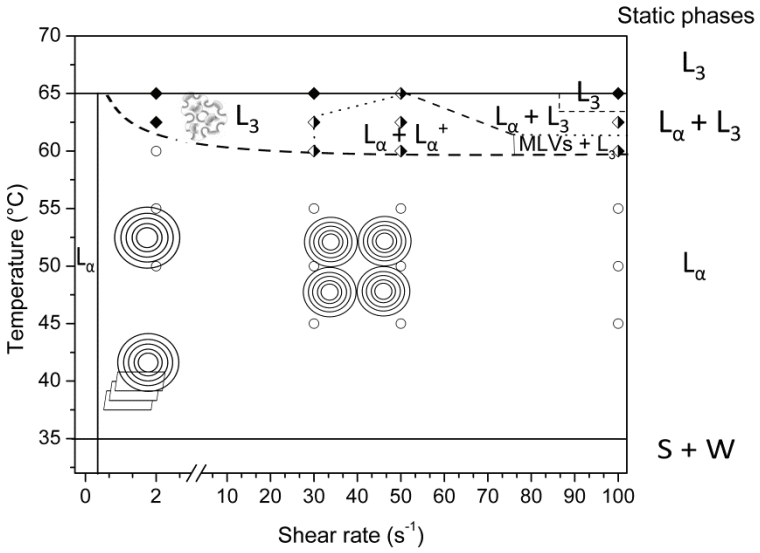

Figure 4.1.18: Dynamic phase diagram (temperature vs. shear rate) for 40 wt% $C_{16}E_4$ in D_2O.

Further details are given in the article "Multi-lamellar vesicle formation in a long-chain nonionic surfactant: $C_{16}E_4/D_2O$ system" Journal of Colloid and Interface Science, 2011, 362, 1–4 (***Paper III***) and the article "Structural Transitions Induced by Shear Flow and Temperature variation in a Nonionic Surfactant/Water System" submitted to Journal of Colloid and Interface Science (***Paper IV***).

4.1.4 VORTICITY BANDING AND VISCOSITY OSCILLATIONS

Figure 4.1.19 shows vorticity banding at 2 s^{-1} for a 40wt% $C_{16}E_4/D_2O$ system. SANS patterns and rheological data have been recorded simultaneously. These scattering patterns come from rheo-SANS-I (PSI) and they are performed at 40°C using a rheometer equipped with Couette quartz cell (Paragraph 3.3.2). In Figure 4.1.19 the vertical direction is scanned with SANS. Due to the transient nature of the bands, the shear flow was stopped. The bands were stable throughout the duration of the vertical scan (to avoid interfering with the shearing history, this scan was performed at the end of the experimental run). The scattering patterns indicate that the turbid bands consist of highly anisotropic patterns corresponding to essentially planar

lamellae, whereas the transparent bands correspond to a more isotropic pattern, indicating MLVs.

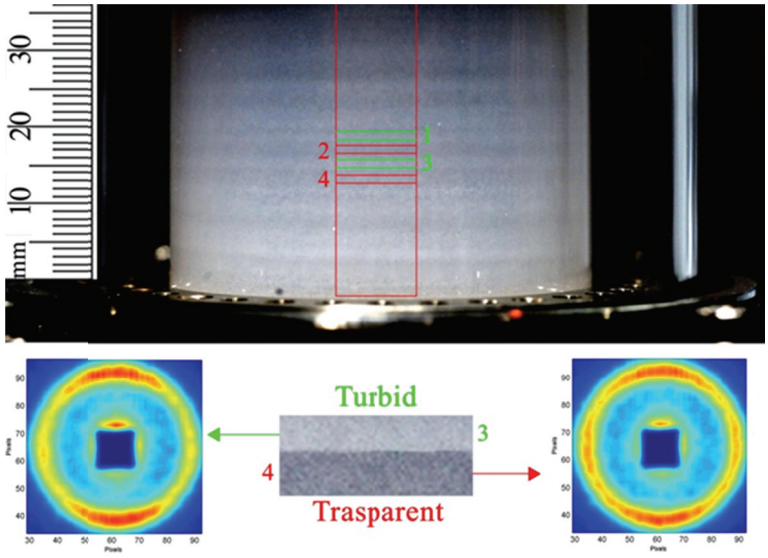

Figure 4.1.19: Photograph of the sample in the Couette without shear flow. The selected 2D SANS patterns correspond to the turbid and transparent bands, obtained through a horizontal scan. The transparent bands in the image represent the MLVs and the turbid bands the L_α phase.

The slit at the sample position is 1 mm height (3 mm wide), and therefore comparable with the size of the stripes, allowing a good spatial resolution. In Figure 4.1.20 the experiment prior to the vertical scan is shown. The rheometer is fixed in position, while the scattering patterns and the viscosity are recorded as a function of time. The oscillations in the apparent viscosity are plotted versus the neutron scattered intensity in the flow (x) and vorticity (y) directions. One can easily observe that the oscillations in viscosity are highly correlated with the scattered intensity in the flow direction, and to a lesser degree, to the intensity in the neutral direction. The well in the flow direction means that the pattern is more anisotropic, which suggests planar lamellae. The peak comes from the isotropic pattern, which suggests MLVs as previously indicated. The data on Figure 4.1.20 then suggests that we are either in the presence of an oscillatory transition between planar lamellae and MLVs, or that these structures are stable, but being displaced periodically along the y-direction.

One should keep in mind that the measured scattering oscillations in the flow direction are originated from one (or two at most) band, since the aperture slit is 1 mm height. The viscosity measured by the rheometer is a result of the sum of all the individual bands. Nevertheless, the period of the scattering

oscillation in the individual band is the same as the viscosity period on the whole sample. There is also a slight phase difference between both oscillations. This suggests that all the bands in the Couette have the same period (equal to the viscosity oscillations) but different phase, and the sum of all of these individual contributions results in the macroscopic measure of viscosity.

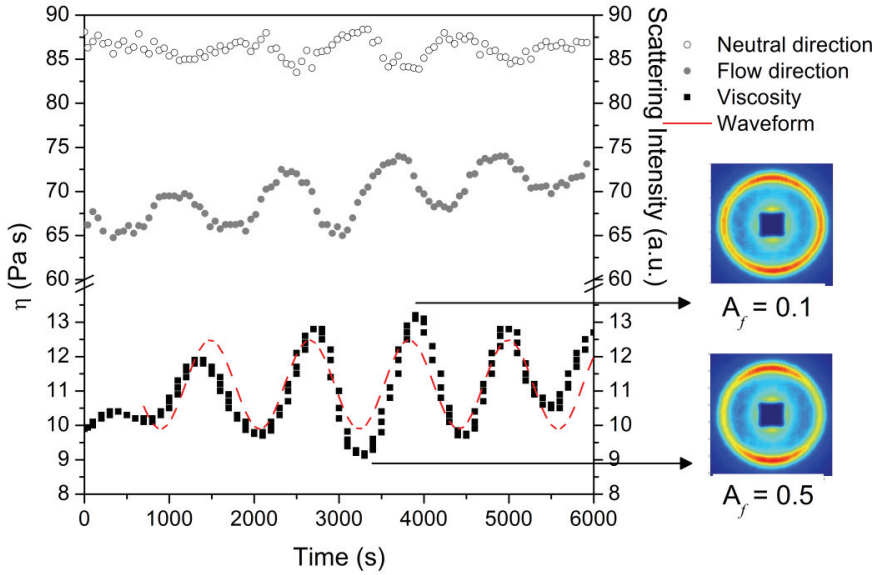

Figure 4.1.20: Evolutions of the apparent viscosity (η) and SANS Intensity, at the lamellar Bragg peak in the vorticity (y) and flow (x) directions in the radial beam. The shear rate is 2 s^{-1}, the composition is 40wt% $C_{16}E_4$ in D_2O at 40°C. On the right, selected SANS patterns at the same time of the peak and well of the viscosity are shown. In order to give a quantitative analysis, the anisotropic factor (A_f) has been calculated. It is defined as $A_f = [i_y - i_x]/i_y$ with $i_{x,y} = \int I_{x,y}(q)dq$ and $I_y(q)$ and $I_x(q)$ as intensity in the y and x directions, respectively. The anisotropic index decreases in the viscosity peak, while it increases in the well.

The sinusoidal fitting of the viscosity oscillations gives a period of about 13 minutes. It is possible to relate the viscosity period to the transient time of the vorticity bands. This correlation is important in order to understand how the flow instability of the shear bands influences the "bulk" viscosity.

With SANS patterns we were able to identify the transparent bands as MLVs and the turbid ones as planar lamellae (Figure 4.1.19). These bands with the lamellar phase in two different morphologies are stacked along the vorticity axis and have the same shear rate but different resistance to the flow (viscosity). Using a simple model [82] for the superposition of the viscosities in the two phases at coexistence, the oscillatory behavior along the plateau can be described as the resultant nucleation of MLVs out of the lamellar phase (or instability and subsequent slow growth).

$$\eta(\dot{\gamma}) = (\alpha)\eta_{L\alpha}(\dot{\gamma}) + (1-\alpha)\eta_{MLV}(\dot{\gamma}) \qquad (4.1.2)$$

where α is the fraction of material in the L_α state, and η_{MLV} and $\eta_{L\alpha}$ are the viscosities in the MLV and L_α state, respectively. If we assume that the volume fraction of the L_α and the MLV are oscillating in time with an angular frequency of $\omega = 5 \cdot 10^{-3}$, with a fraction α_0 as offset of the L_α state, Eq. 4.1.3.

$$\alpha(t) = \alpha_0 + \alpha_1 \sin(\omega t) \tag{4.1.3}$$

The resulting viscosity is also oscillating in time with the same angular frequency, Eq. 4.1.4.

$$\begin{aligned} \eta(\dot{\gamma}, t) = {} & \alpha_0 \eta_{L\alpha}(\dot{\gamma}) + (1 - \alpha_0)\eta_{MLV}(\dot{\gamma}) + \\ & + (\eta_{L\alpha}(\dot{\gamma}) - \eta_{MLV}(\dot{\gamma}))\alpha_1 \sin(\omega t) \end{aligned} \tag{4.1.4}$$

The phase of the oscillating viscosity depends on the phase of the oscillating volume fractions of the L_α and MLV, respectively.

Using our results we are able to confirm and expand the Wilkins and Olmsted [82] model and we are also able to give a reasonable explanation. Lamellar phases in shear flow are normally aligned in the "*c*" direction, with the exception of a minor population of lamellae aligned in the *a*-orientation. The *a*-orientation consists of a metastable state where a bilayer domain can be trapped because in this orientation there is no torque on the bilayers to orient them in the flow direction [72]. The observed structure factor peaks in the L_α patterns arise from a minor population of bilayers with *a*-orientation and from the MLVs. The *c*-orientation, where the majority of the bilayers are in, does not contribute to the scattering intensity, as the bilayers in this orientation are not in Bragg condition.

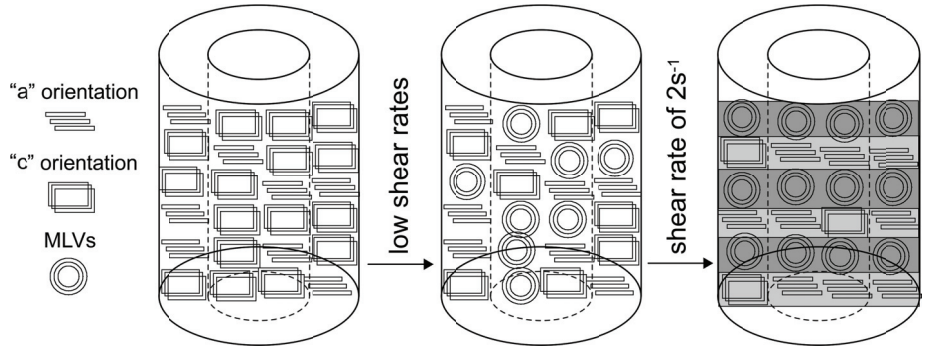

Figure 4.1.21: Schematic representation of the shear bands in the Couette geometry.

A possible mechanism that explains the oscillations could be that the lamellar phase domains in the *c*-orientation are transformed into MLV at low shear rates or low value at strain units of 2 s^{-1}, but at such low shear rate there is not enough energy to bend the lamellar phase in the *a*-orientation (α_0

fraction of the material). This would originate the coexistence of two bilayer states, which have different flow properties (different viscosities) and are segregated into two types of bands along the vorticity axis. At high temperature (55°C) a complete lamellar to MLV transition appears (Paragraph 4.1.3). It is reasonable to think that at such temperature, the energy required to transform the *a*-orientation in MLVs is lower than that required at 40°C, and the transition can be reached at shear rate of 2 s^{-1}.

The presence of lamellae in the *a*-orientation induces instabilities on the MLVs, which can result in the MLVs to be transformed again in planar lamellae, which periodically undergoes again the transition to MLVs with a timescale of c.a. 13 minutes. The period of the viscosity oscillation is equal to the period of the scattering modulation in the shear bands indicating that both phenomena are related. Nevertheless, the phase of both oscillations is different. This spatial transient behavior of shear bands with different structure and different viscosities, manifests itself in oscillations of the overall rheological signals.

In conclusion, by rheo-SANS experiments, we showed that the observed transparent and turbid optical appearance during a constant shear rate experiments is caused by different structural assembly of the lamellae (MLVs or lamellar phase). Furthermore we identified the vorticity bands as the flow instability causing the large oscillations in the apparent viscosity. The viscosity oscillations are due to the two different lamellar states (MLVs and classical lamellar phase) as these structural aggregations have a different resistance to flow. Typically the formation of a closed structure in a solution gives rise to a viscous gel, which is the reason of the shear thickening region. On the contrary in a "perfect" lamellar phase where MLVs are not formed only a shear thinning region will be present.

It is worthy to note that it is possible to exclude flow instability due to the Couette geometries. In fact according to the discussion reported in the Paragraph 3.1.6, applying the Equation 3.1.22 it is possible to calculate the *Ta number* and consequently the critical shear rate of the Taylor instability. Following Eq. 3.1.23 and using a mean viscosity of 22 Pas, density of 0.953 g/cm^3 (relative to the $C_{16}E_4$), R_i = 12.5 mm and δ_c = 1.08 (see Paragraphs 3.1.5/6), we calculated:

$$\omega_c = \frac{\left(41.2 \cdot 22\, Kg/sm\right)}{\left[953\, Kg/m^3 \cdot 1.25^2 \cdot 10^{-4} m^2 \left(0.08\right)^{3/2}\right]} \simeq 2.69 \cdot 10^5\, rad/s \qquad (4.1.5)$$

$$n_c = \frac{\left(60 \cdot 2.69 \cdot 10^5\, rad/s\right)}{\left[2 \cdot \pi\right]} \simeq 2.57 \cdot 10^6\, \mathrm{min}^{-1} \qquad (4.1.6)$$

$$\dot{\gamma}_c = 1.291 \cdot 2.57 \cdot 10^6\, \mathrm{min}^{-1} = 3.32 \cdot 10^6\, s^{-1} \qquad (4.1.7)$$

The shear rates applied on the sample are always lower than 10^6 s^{-1}, accordingly it is possible to exclude the Taylor instability.

Considering the Re numbers and consequently applying the Equations 3.1.26 and 27 the critical shear rates of the Reynolds turbulence are given

$$\omega_{c2} = \frac{\left(2 \cdot 22\, Kg/sm \cdot 1000\right)}{\left[953\, Kg/m^3 \cdot 1.25^2 \cdot 10^{-4} m^2 \left(\left(1.08\right)^2 - 1\right)\right]} \simeq 1.78 \cdot 10^6\, rad/s \qquad (4.1.8)$$

$$n_{c2} = \frac{\left(60 \cdot 1.78 \cdot 10^6\, rad/s\right)}{\left[2 \cdot \pi\right]} \simeq 1.70 \cdot 10^7\, \mathrm{min}^{-1} \qquad (4.1.9)$$

$$\dot{\gamma}_{c2} = 1.291 \cdot 1.70 \cdot 10^7\, \mathrm{min}^{-1} \simeq 2.19 \cdot 10^7\, s^{-1} \qquad (4.1.10)$$

$$\dot{\gamma}_{c1} = 1.291 \cdot 1.70 \cdot 10^4\, \mathrm{min}^{-1} \simeq 2.19 \cdot 10^4\, s^{-1} \qquad (4.1.11)$$

The shear rates applied on the sample are always lower than $2 \cdot 10^4$ s^{-1}, accordingly it is possible to exclude the Reynolds instability.

4.2 SHEAR EFFECTS IN APFN/D_2O SYSTEM

In order to explore better the structural changes induced by temperature, a temperature-sweep experiment has been performed on the sample. In this experiment the evolution of the storage and loss moduli is continuously monitored during a temperature ramp, at a constant heating rate (1°C/min) and frequency of 1 Hz, Figure 4.2.1. In the lower temperature range of the lamellar phase the sample behaves as a gel-like material since the storage modulus (G') is higher than the loss modulus (G''). Around 39°C a G'-G'' crossover is observed and both dynamic moduli decrease with increasing temperature being G''>G'. The crossover become visible in the Figure 4.2.1 is at a temperature lower than the nematic transition temperature observed by DSC. The sensitive decrease of dynamic moduli with the temperature increase accounts for the reduction of the smectic order in proximity of the lamellar-to-nematic transition. Such effect prevails on the increase of the defectivity of lamellae [122], and the result is a elasticity decrease with the temperature rise. All these results states that the defective lamellar phase can be distinguished in two regions: i) a low density defects phase at lower temperatures, L_α^{-d}; ii) a high density defects phase at higher temperatures, L_α^{+d}.

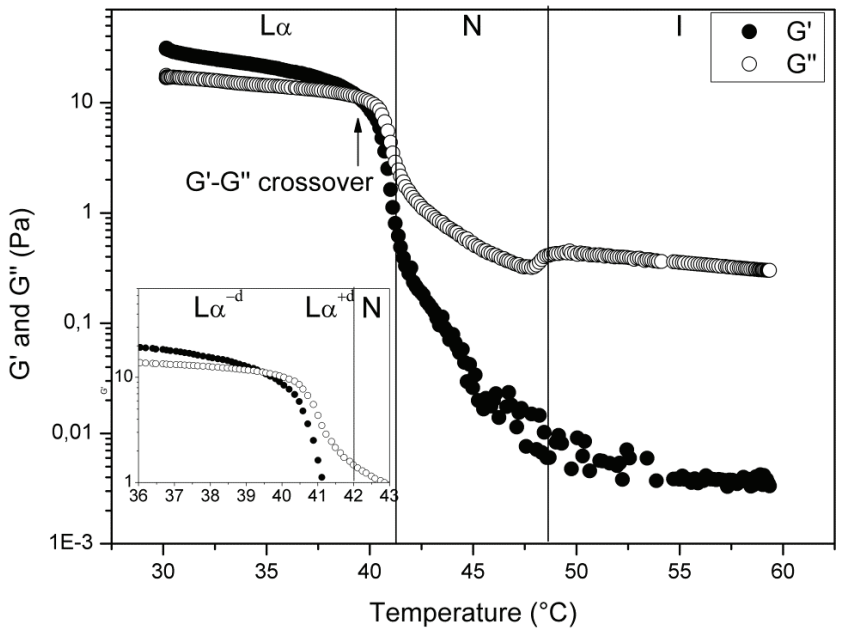

Figure 4.2.1: Time cure test at 1 Hz in the range 30-60°C. The two vertical lines are the transition temperature obtained by DSC. The inset shows a zoom in view of L_α region.

Figure 4.2.2 shows the transient viscosity for the mixture at 35°C in L_{α}^{-d} region after the inception of shear flow. For all shear rates reported in the figure (0.1, 1.0, 4.0 and 10 s^{-1}) the viscosity changes with time up to a steady state which is marked by a plateau in the curves. The time for reaching the steady state depends on the applied shear rate, and it takes longer time when the shear rate value is lower. The transient viscosity recorded at shear rates lower than 10 s^{-1} shows an evolution in agreement with the flow of a smectic lamellar systems as reported by Partal et al. [186]. The viscosity decrease together with increasing time and shear rate results in a shear-induced orientation of the lyotropic domains and leads to a aligned lamellar phase with the director perpendicular to the shear field [186].

The transient viscosity recorded at 10 s^{-1} shows an increase with the time and reaches a plateau value higher than that one obtained at lower shear. This trend seems to be reasonable with a gradual development of MLV, as observed in some recent studies conducted on $C_{10}E_3$/water mixtures [6-8]. It is important to mark that such plateau value is not too high, because of the lamellae and MLV coexistence [75, 188, 189].

Figure 4.2.2 shows also the ^2H NMR spectra of ^2H_2O for the sample at different shear rates. These spectra correspond to steady state structures under shearing. Similarly to viscosity measurements, the evolution of ^2H NMR spectra at 10 s^{-1} reflects the gradual formation of MLV in the system (coexistence of MLV and planar lamellae). In fact the Pake doublet of the planar lamellae turns into a broad peak as a consequence of the presence of multilamellar vesicles [9, 10, 145, 171, 190, 191].

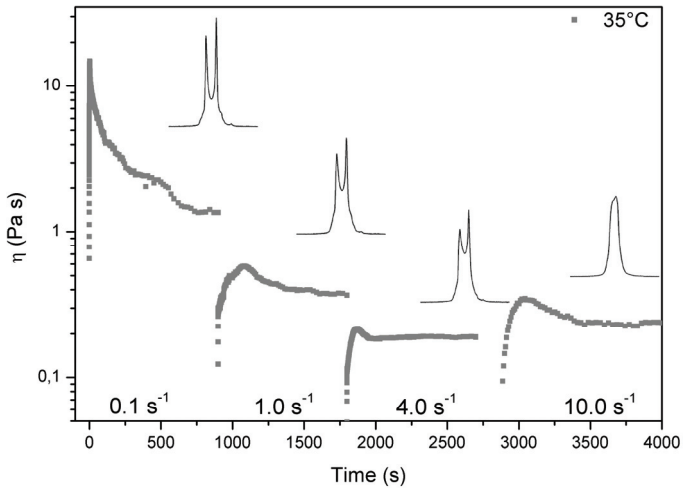

Figure 4.2.2: The viscosity as a function of time for fresh solutions (30wt% APFN) at different shear rate values (0.1, 1.0, 4.0 and 10 s^{-1}) at 35°C. For each shear rate, the Rheo-^2H NMR corresponds to the viscosity plateau region.

Figure 4.2.3 reports the ^{2}H-NMR spectra as a function of shear strain for the sample sheared at 10 s^{-1}, at 35°C. The initial spectrum is a powder pattern which is typical of non-oriented lamellar structures, while it becomes a broad singlet increasing the strain confirming the transformation from planar lamellae, of the L_{α}^{-d} region, to MLV (at 35°C and a constant shear rate of 10 s^{-1}). The broad singlet, after 18000 strain unit, can be due to a coexistence of MLV and planar lamellae.

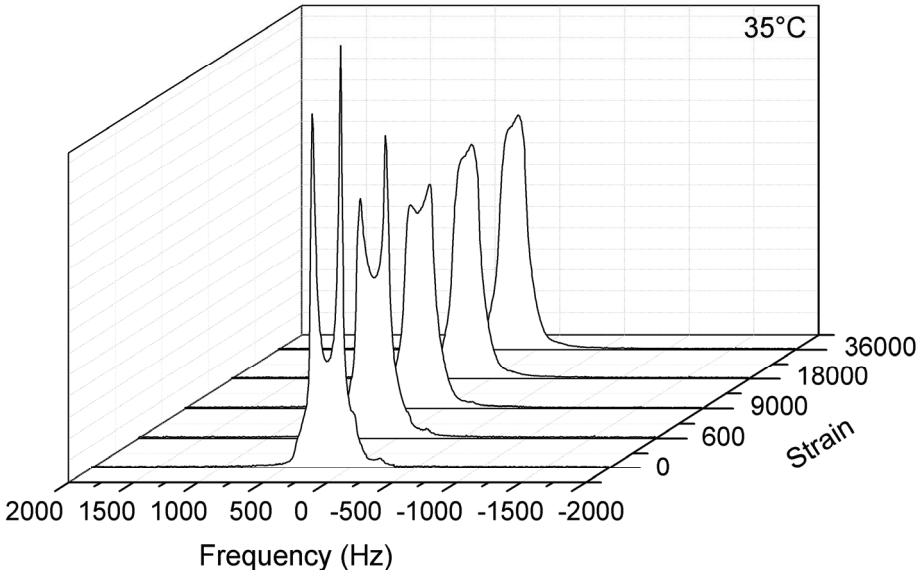

Figure 4.2.3: Strain evolution of spectra during the MLV formation from planar layers at 35°C and a constant shear rate of 10 s^{-1}.

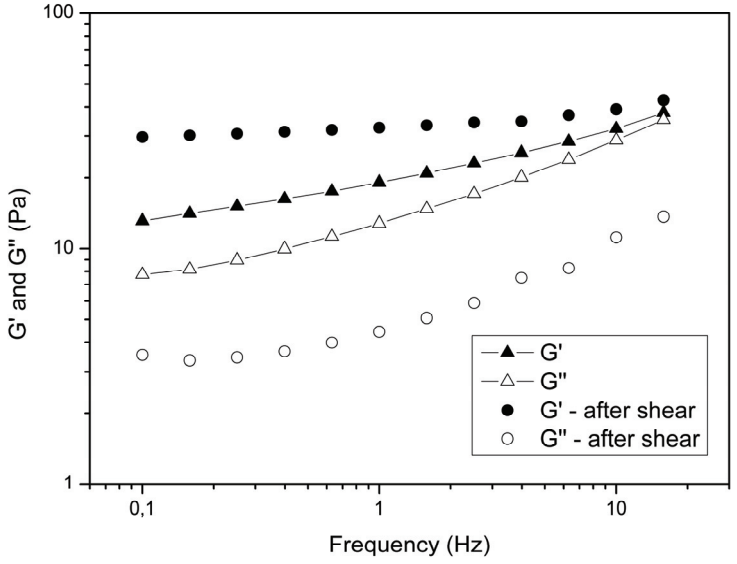

Figure 4.2.4: Storage modulus, G', and loss modulus, G'' as a function of the oscillatory frequency obtained before and after (1800 s) the transient viscosity measurement at 10 s^{-1} for the 30wt% APFN, T = 35°C.

In Figure 4.2.4 we report the viscoelasticity of the sample at 35°C, before and after the viscosity measurements. The storage modulus, G', before and after the shearing, is higher than the loss modulus, G'', in the frequency range from 0.07 to 15 Hz. In addition it is worth noting that G' dynamic modulus after the transient measurements becomes dominant. This is a characteristic feature of the MLV phase [178].

Figure 4.2.5 reports the transient viscosity and ^{2}H NMR spectra at different shear rates both for the L_α^{+d} region (40°C) and for the nematic phase (at 45°C). At 40 °C the ^{2}H NMR spectra show clearly the transformation of lamellae into MLV. The MLV formation begins at shear rate of 4 s^{-1}, while at shear rate of 10 s^{-1} MLV are formed with a smaller size, as suggested by the narrowing of the deuterium spectral line. As far as nematic phase is concerned, the ^{2}H NMR line shape does not change with increasing shear rate and the MLV formation can be excluded (Figure 4.2.5B). Quadrupolar splittings at the lamellar-to-nematic transition decreases with increasing the temperature and do not show any discontinuity.

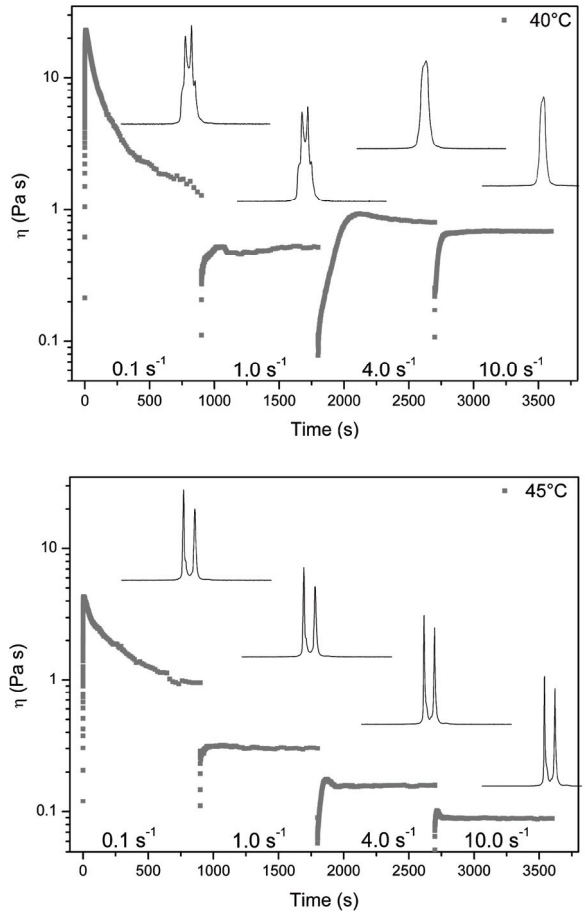

Figure 4.2.5: The viscosity as a function of time for various solutions at different shear rate values (0.1, 1.0, 4.0 and 10 s^{-1}) at 40 (a) and 45°C (b). For each shear rate, the Rheo-^{2}H NMR correspond to the plateau region on viscosity.

At this point we may conclude by the following analysis. Considering the effect of shear on the lamellar phase, it is worthy to note that the MLV formation occurs at ~7200 strain units at 40°C (Figure 4.2.5A, 4 s^{-1}), whilst it occurs at ~18000 strain units at 35°C (Figure 4.2.2, 10 s^{-1}). This effect can be ascribed to an increase of defects (i.e. pores) in the lamellar phase on heating. Using the water self-diffusion, Chidichimo et al. [122] already demonstrated that the density of defects raised with increasing the temperature, and the defect area of layers reaches a value of ca. 25% at the lamellar-nematic transition. Similar result have been obtained by many researchers studing other lamellar-to-nematic phase transitions [49, 192, 194].

Further details are given in the article "Evidence of Formation of Ammonium Perfluorononanoate/^2H_2O Multilamellar Vesicles: Morphological Analysis by Rheology and Rheo-^2H NMR Experiments" Langmuir, 2010, 26, 19060–19065 (***Paper V***).

4.3 SHEAR EFFECTS IN LECITHIN/CYCLOHEXANE/WATER SYSTEM

The reason of the popularity of wormlike micelles for physicists lies in their complex rheological behavior like shear banding and chaotic response, which are connected to the thinning (thickening) behavior of these systems. Much of the experimental study about the viscoelastic response of wormlike micelles subjected to shear flow in dilute, semi-dilute or concentrated solutions have been focused on the shear banding transitions (see reference [38]). In this thesis we present a first investigation on the non-linear flow properties and transient orientational order fluctuations. We observed the shear-thinning Lecithin-Water-Cyclohexane wormlike micellar system at a concentration near to the zero-shear Isotropic-Nematic phase transition [194], with a micellar volume fraction (φ) of 0.28 and water-to-Lecithin molar ratio (W_0) of 10 (see Paragraph 2.6.1).

The flow curve, $\eta(\dot{\gamma})$, and the corresponding $\sigma(\dot{\gamma})$ curve in Figure 4.3.1 have been built by overlapping rheological data obtained through both strain and stress controlled instruments. Very low shear rates have been determined through creep tests performed at imposed stresses σ_0 in the range 1 - 60 Pa. A stress plateau at σ_P = 50 ± 5 Pa extended from $\dot{\gamma}_1 = 4 \cdot 10^{-4}$ s^{-1} up to $\dot{\gamma}_2$ = 0.7 s^{-1}, corresponding to a drop in the effective viscosity by four orders of magnitude and approaching a slope close to -1, in agreement with the existence of a limiting stress σ_P. Such a plateau can be explained by the shear banding phenomenon [69]. Then the stress plateau is associated with unstable flow. At higher shear rates the aligned state can be identified as a nematic phase [195]. Moreover, it was shown that for $\dot{\gamma} > \dot{\gamma}_2$ the scattering patterns developed essentially only in the neutral direction, indicating micellar alignment in the flow direction [195].

The rheo-imaging NMR (for details to see Paragraph 3.2.4) results are consistent with this picture.

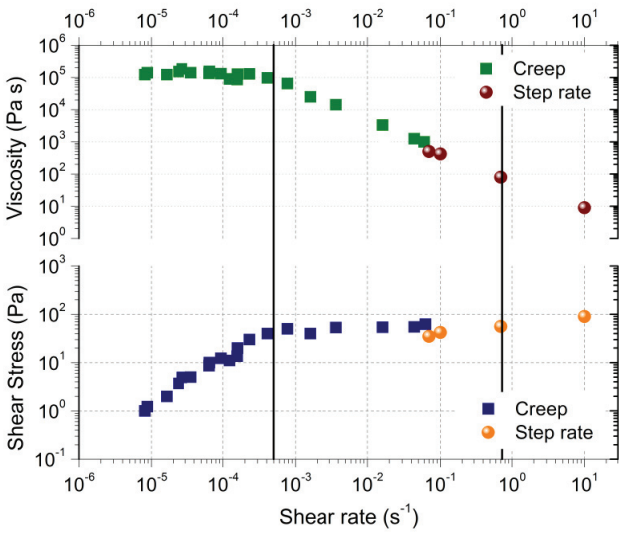

Figure 4.3.1: Experimental flow curve and the corresponding viscosity-shear rate curve, built by overlapping rheological data obtained by strain and stress-controlled instruments.

In fact by investigating the stress plateau using rheo-imaging NMR we observed (Figures 4.3.2 and 3) some flow-instabilities even though further investigations are needed to validate this assumption drawn using the experiments performed.

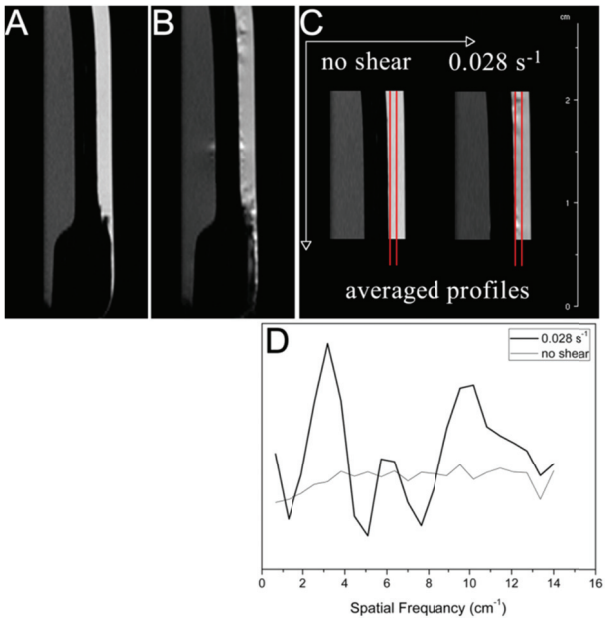

Figure 4.3.2: Two-dimensional slice ^{1}H-NMR GEFI images recorded at t = 16°C. a) rheological cell (Couette) loaded with the sample at rest after 25 min at equilibrium (light gray); the rotor was loaded with internal liquid reference, H_2O (60%) + D_2O (40%) shown as dark gray; vertical and horizontal arrows indicate the vorticity and shear flow directions, respectively. b) applied shear rate 0.028 s^{-1} : image collected after t = 25 min where axial heterogeneities are clearly visible. c) axial profiles (width = 15 mm) selected in the cell gap where the ^{1}H-NMR signal intensity has been averaged at rest (left) and for 2 h and 30 min (from t=5 min to t=2 h and 35 min) under shear rate 0.028 s^{-1} (right). d) Fourier transform of ^{1}H-NMR intensity averaged in the selected profiles as a function of the spatial frequency.

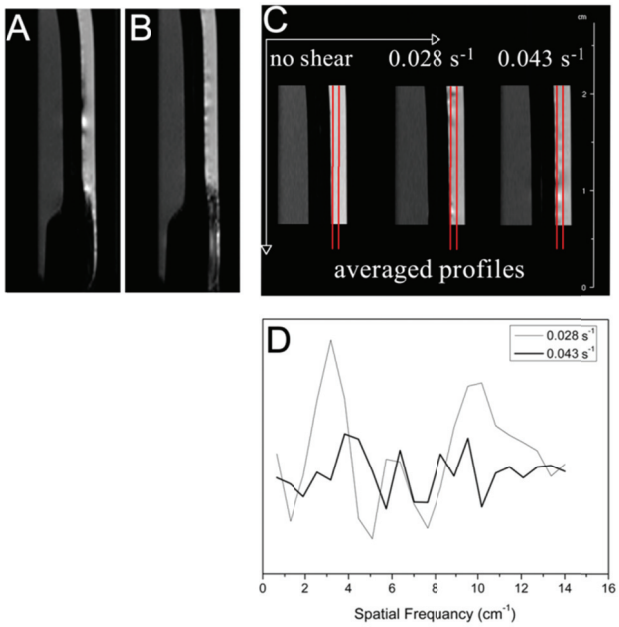

Figure 4.3.3: Two-dimensional slice ^{1}H-NMR GEFI images recorded at t = 16°C. Conditions: applied shear rate = 0.043 s^{-1}. a) image after t = 35 min. b) after t = 1 h and 25 min. c) selected axial profiles at $\dot{\gamma} = 0$ (left), $\dot{\gamma} = 0.028$ s^{-1} (middle) and $\dot{\gamma} = 0.043$ s^{-1} (right). d) Fourier transform of ^{1}H-NMR intensity averaged in the selected profiles as a function of the spatial frequency.

5 CONCLUSIONS

The shear flow effect on lyotropic phases is an interesting and fascinating topic. The main aim of this thesis is the lamellar-to-MLV transformation under shear and the relative MLV stability. In addition the lamellar-to-sponge and its reverse transition under shear have been studied.

For the first time the lamellar-to-MLV transformation under shear in the APFN/D_2O system has been observed. This result was unexpected because usually the lamellar phases of ionic surfactants have a high rigidity (bending rigidity). The shear effect must be overcome the bending rigidity in order to obtain the transition from the planar lamellae to the closed structure. In this case the MLV formation under shear is due to the increasing of defects of the planar lamellae with temperature increase. The evidence of the correlation between density defects and MLV formation is in agreement with the literature [196].

The lamellar-to-MLV transformation under shear has been also observed in $C_{12}E_3/D_2O$, $C_{12}E_5/D_2O$ and $C_{16}E_4/D_2O$ systems. The C_nE_m/D_2O systems represent a good model to understand the correlation between the MLV formation and the surfactant molecular structure. In fact using the Würger model (Paragraph 2.2) and our experimental results it is possible to calculate the bending rigidity κ by applying the Eq. 2.2.3.

The Table 5.1.1 shows our experimental results and literature data.

C_nE_m	δ	$\kappa(k_BT)$	Strain, concentration, T (°C)		
$C_{10}E_3$	27.6 Å [72]	3.4	6000	40wt%	25-38
$C_{12}E_3$	30.8 Å [197]	4.7	18000	50wt%	34
$C_{12}E_4$	31.1 Å [197]	4.2	10000 *	40wt%	25
$C_{12}E_5$	32.6 Å [197]	4.0	6000	40wt%	55
$C_{16}E_4$	36.6 Å	6.8	8000	40wt%	55

Table 5.1.1: Calculated bending rigidity for $C_{10}E_3$, $C_{12}E_3$, $C_{12}E_4$, $C_{12}E_5$ and $C_{16}E_4$ in deuterated water. The $C_{16}E_4$ bilayer thickness is obtained from the slope of the curve lamellar spacing vs the inverse surfactant volume fraction (data not shown) as reported for $C_{10}E_3$ [72]. * The value is not absolutely determined.

Bending rigidity, κ, and spladely modulus, $\bar{\kappa}$, are two parameters that control the transition from planar lamellae to MLVs. We focused our investigations on $C_{12}E_3$ which has a higher κ than $C_{12}E_4$ $C_{12}E_5$ and $C_{10}E_3$,

meaning that more energy is required to bend a $C_{12}E_3$ lamellae. This seems not true for $C_{16}E_4$, but in this case we have to take in account the temperature effect. The predominant temperature dependence is related to the monolayer spontaneous curvature H_0 consequently to the saddle-splay modulus $\bar{\kappa}$. We can conclude that greater energy is required when κ is higher. At the same time to reduce the energy required to bend the planar lamellae we can increase the temperature (in the range of MLV existence). This assumption is not always true, in fact the temperature effect can be opposed as in the case of $C_{16}E_7$ [76], which means that the relation between temperature and $\bar{\kappa}$ is complex.

Moreover we observed some flow instabilities in the $C_{16}E_4/D_2O$ system and in lecithin based system. In the case of $C_{16}E_4$ there were viscosity oscillations and shear banding phenomenon. For instance in the case of $C_{16}E_4$ the MLV are spatially ordered in bend and when the MLV fraction increase the viscosity increase and vice-versa giving oscillations phenomenon. As for lecithin instabilities maybe related to the shear induced structures or transformation, but this is still not completely clear.

ACKNOWLEDGMENTS

I would like to thank all the people I believe contributed to my studies, by telling a little story. Since I was a child I always had clear ideas on the next step of my life. However, when I was about to graduate from high school, I was really undecided to attend weather Physics or Chemistry major at University of Calabria. Then I met prof. Giuseppe Chidichimo who gave a lesson at the high school and clarified my thoughts to choose chemistry.

My first year at University of Calabria was not so encouraging and I was about to left Rende to go studying at another university. Then I met prof. Marcello Longeri. He made my curiosity for science to come back and I decided to continue my studies here in Calabria. Fruitful and funny years followed my decision, sharing great experiences with a lot of friends (Paolo, Filippo, Attilio, Sante, etc…). Afterwards I asked Prof. Giuseppe Antonio Ranieri to carry out the experimental part of my bachelor thesis in the Physical Chemistry Soft Matter Laboratory "Mario Terenzi" (PC_SM Mario Terenzi). Prof. Ranieri accepted and assigned Dr. Cesare Oliviero Rossi as to be my supervisor.

It began a weird and wonderful relationship with Cesare made of discussions, jokes etc., and this relationship went also through the master and PhD course. During the last period I knew better and appreciated the professionalism and competence of Prof. Luigi Coppola, Dr. Isabella Nicotera, Prof. Giuseppina De Luca, Prof. Lionello Pogliani, Prof. Nicola Uccella and Dr. Filipe E. Antunes.

During my PhD course one day Cesare told me that for my studies it would be great to go to Lund University (Sweden) where they have very good facilities and willingness to train young researchers. So I left Rende and I met Prof. Ulf Olsson. By using his energy and patience he followed me in an interesting science adventure. In this period I met a lot of new people (Prof. Karin Shiller, Wei, Alexandra, Giuseppe, etc…), but a particular mention goes to Prof. Kell Mortensen (University of Copenhagen) and Dr. Bruno B.F. Silva for the helpful scientific discussions. In the last year Dr. Luigi Filippelli join our laboratory and I also thank him for giving new perspectives and scientific ideas. Last but absolutely not the least I want to thank my parents Tina and Franco and my lovely girlfriend Rossella.

REFERENCES

1 Diat, O.; Roux, D.; Nallet, F. Effect of shear on a lyotropic lamellar phase. *J. Phys. II* **1993**, *3*, 1427-1452.

2 An, H.; Li, X.; Geng, Y.; Wang, Y.; Wang, X.; Li, L.; Li, Z.; Yang, C. Shear-induced conformational ordering, relaxation, and crystallization of isotactic polypropylene. *J. Phys. Chem. B* **2008**, *112*, 12256-12262.

3 Endoh, M.K.; Saito, S.; Hashimoto, T. Shear-induced structures in semidilute polystyrene solution: effect of solvent quality. *Macromolecules* **2002**, *35*, 7692-7699.

4 Gradzielski, M. Vesicles and vesicle gels - structure and dynamics of formation. *J. Phys.: Condens. Matter* **2003**, *15*, 655-697.

5 Bergenholtz, J.; Wagner, N.J. Formation of AOT/brine multilamellar vesicles. *Langmuir* **1996**, *12*, 3122-3126.

6 Medronho, B.; Shafaei, S.; Szopko, R.; Miguel, M.G.; Olsson, U.; Schmidt, C. Shear-induced transitions between a planar lamellar phase and multilamellar vesicles: continuous versus discontinuous transformation. *Langmuir* **2008**, *24*, 6480-6486.

7 Zipfel, J.; Nettesheim, F.; Lindner, P.; Le, T.D.; Olsson, U.; Richtering, W. Cylindrical intermediates in a shear-induced lamellar-tovesicle transition. *Europhys. Lett.* **2001**, *53*, 335-341.

8 Medronho, B.; Fujii, S.; Richtering, W.; Miguel, M.G.; Olsson, U. Reversible size of shear-induced multi-lamellar vesicles. *Colloid Polym. Sci.* **2005**, *284*, 317-321.

9 Nettesheim, F.; Zipfel, J.; Olsson, U.; Renth, F.; Lindner, P.; Richtering, W. Pathway of the shear-induced transition between planar lamellae and multilamellar vesicles as studied by time-resolved scattering techniques. *Langmuir* **2003**, *19*, 3603–3618.

10 Fujii, S.; Koschoreck, S.; Lindner, P.; Richtering, W. Influence of a triblock copolymer on phase behavior and shear-induced topologies of a surfactant lamellar phase. *Langmuir* **2009**, *25*, 5476-5483.

11 Nath, A.; Atkins, W.M.; Sligar, S.G. Applications of phospholipid bilayer nanodiscs in the study of membranes and membrane proteins. *Biochemistry* **2007**, *46*, 2059-2069.

12 Lagaly, G.; Richtering, W. Mesophases, polymers, and particles. Springer: New York, 2004.

13 Razumas, V.; Lindman, B.; Nylander, T. Surface and colloid science. Springer: New York, 2001.

14 Oda, R.; Panizza, P.; Schmutz, M.; Lequeux, F. Direct Evidence of the Shear-Induced Structure of Wormlike Micelles: Gemini Surfactant 12−2−12. *Langmuir* **1997**, *13*, 6407-6412.

15 Berret, J.-F.; Gamez-Corrales, Z.; Lerouge, S.; Decruppe, J.-P. Shear-thickening transition in surfactant solutions: New experimental features from rheology and flow birefringence. *Eur. Phys. J. E* **2000**, *2*, 343-350.

16 Berret, J.-F.; Lerouge, S.; Decruppe, J.-P. Kinetics of the Shear-Thickening Transition Observed in Dilute Surfactant Solutions and Investigated by Flow Birefringence. *Langmuir* **2002**, *18*, 7279-7286.

17 Berret, J.-F.; Porte, G. Metastable versus unstable transients at the onset of a shear-induced phase transition. *Phys Rev E* **1999**, *60*, 4268-4271.

18 Berret, J.-F.; Porte, G.; Decruppe, J.-P. Inhomogeneous shear flows of wormlike micelles: a master dynamic phase diagram. *Phys Rev E* **1997**, *55*, 1668-1676.

19 Berret, J-F.; Roux, D.C.; Lindner, P. Structure and rheology of concentrated wormlike micelles at the shear-induced isotropic-tonematic transition. *Eur Phys J B* **1998**, *5*, 67-77.

20 Boltenhagen, P.; Hu, Y.; Matthys, E.F.; Pine, D. J. Inhomogeneous structure formation and shear-thickening in worm-like micellar solutions. *Europhys. Lett.* **1997**, *38*, 389-394.

21 Hu, Y.T.; Boltenhagen, P.; Pine, D.J. *J. Rheol.* Shear thickening in low-concentration solutions of wormlike micelles. I. Direct visualization of transient behavior and phase transitions**. 1998**, *42*, 1185-1208.

22 Butler, P. Shear induced structures and transformations in complex fluids. *Curr. Opin. Colloid Interface Sci.* **1999**, *4*, 214-221.

23 Berret, J.-F. Rheology of Wormlike Micelles: Equilibrium Properties and Shear Banding Transition. Springer: Dordrecht, 2005.

24 Lerouge, S.; Decruppe, J.-P.; Humbert, C. Shear Banding in a Micellar Solution under Transient Flow. *Phys. Rev. Lett.* **1998**, *81*, 5457-5460.

25 Lerouge, S.; Decruppe, J.-P.; Olmstead, P. Birefringence Banding in a Micellar Solution or the Complexity of Heterogeneous Flows. *Langmuir* **2004**, *20*, 11355-11365.

26 Becu, L.; Manneville, S.; Colin, A. Spatiotemporal Dynamics of Wormlike Micelles under Shear. *Phys. Rev. Lett.* **2004**, *93*, 018301-018305.

27 Fischer, E.; Callaghan, P.T. Is a birefringence band a shear band? *Europhys Lett* **2000**, *50*, 803–809.

28 Fischer, E.; Callaghan, P.T. Shear banding and the isotropic-tonematic transition in wormlike micelles. *Phys Rev E* **2001**, *64*, 011501.

29 Lopez-Gonzalez, M.R.; Holmes, W.M.; Callaghan, P.T.; Photinos, P. Shear Banding Fluctuations and Nematic Order inWormlike Micelles. J. *Phys. Rev. Lett.* **2004**, *93*, 268302.

30 Britton, M.M.; Callaghan, P.T. Shear banding instability in wormlike micellar solutions. *Eur. Phys. J. B* **1999**, *7*, 237-249.

31 Decruppe, J.P.; Lerouge, S.; Berret, J.-F. Insight in shear banding under transient flow. *Phys. Rev. E* **2001**, *63*, 022501.

32 Decruppe, J.P.; Ponton, A. Flow birefringence, stress optical rule and rheology of four micellar solutions with the same low shear viscosity. *Eur. Phys. J. E* **2003**, *10*, 201-207.

33 Liu, C.H.; Pine, D.J. Shear-Induced Gelation and Fracture in Micellar Solutions. *Phys. Rev. Lett.* **1996**, *77*, 2121.

34 Kadoma, I.A.; Van-Egmond, J. W. Shear-Enhanced Orientation and Concentration Fluctuations in Wormlike Micelles: Effect of Salt *Langmuir* **1997**, *13*, 4551-4561.

35 Schubert, B.A.; Wagner, N.J.; Kaler, E. W.; Raghavan, S.R. Shear-Induced Phase Separation in Solutions of Wormlike Micelles *Langmuir* **2004**, *20*, 3564-3573.

36 Cappelaere, E.; Berret, J.-F.; Decruppe, J.P.; Cressely, R.; Lindner, P. Rheology, birefringence, and small-angle neutron scattering in a charged micellar system: Evidence of a shear-induced phase transition. *Phys. Rev. E* **1997**, *56*, 1869-1878.

37 Fielding, S. M.; Olmsted, P. D. Flow phase diagrams for concentration-coupled shear banding. *Eur. Phys. J. E* **2003**, *11*, 65-83.

38 Olmsted, P. D. Perspectives on shear banding in complex fluids. *Rheol. Acta* **2008**, *47*, 283-300.

39 Alami, E.; Almgren, M.; Brown, W.; Francois, J. Aggregation of Hydrophobically End-Capped Poly(ethylene oxide) in Aqueous Solutions. Fluorescence and Light-Scattering Studies *Macromolecules* **1996**, *29*, 2229-2243.

40 Tanford, C. The Hydrophobic Effect: Formation of Micelles and Biological Membranes. Wiley: New York, 1980.

41 Hartley, G. Aqueous solutions of paraffin-chain salts. Hermann & Cie.: Paris, 1936.

42 Chandler, D. Interfaces and the driving force of hydrophobic assembly. *Nature* **2005**, *437*, 640-647.

43 Holmberg, K.; Jönsson, B.; Kronbreg, B.; Lindman, B. Surfactants and polymers in aqueous solution. 2nd edition ed.; Wiley: Chichester, 2003.

44 Myers, D. Surfactant science and technology. Wiley-Interscience: Hoboken, 2006.

45 Evans, D.; Wennerström, H. The Colloidal Domain: Where Physics, Chemistry, and Biology Meet. Wiley-VCH: New York, 1999.

46 Ekwall, P. in "'Advances in Liquid Crystals" Vol. 1 (G. H. Brown, Ed.). Academic Press: New York, 1975.

47 Tiddy, T.G. Surfactant-water liquid crystal phases, *Phys. Rep.* **1980**, *57*, 1-46.

48 Lawson K.B.; Flautt, T.J. Magnetically oriented lyotropic luquid crystalline phases. *J. Am. Chem. Soc.* **1967**, *89*, 5489-5491. & Tolédano, P.; Figueiredo Neto, A. M. Phase transitions in complex fluids. World Scientific: Singapore, 1998.

49 Photinos, P.J.; Yu, L.J.; Saupe, A. Resistivity Measurements on Aligned Amphiphilic Liquid Crystalline States. *Mol. Cryst. Liq. Cryst.* **1981**, *67*, 227-281.

50 Alves, S.; Demouchy, G.; Bee, A.; Talbot, D.; Bourdon, A.; Figueiredo Neto, A.M. Investigation of the sign of the Soret coefficient in different ionic and surfacted magnetic colloids using forced Rayleigh scattering and single-beam Z -scan techniques. *Philos. Mag.* **2003**, *83*, 2059-2066.

51 Safinya, C.R.; Sirota, E.B.; Bruinsma, R.F.; Jeppesen, C.; Plano, R.J. Structure of Membrane Surfactant and Liquid Crystalline Smectic Lamellar Phases Under Flow. *Science* **1993**, *261*, 588-591.

52 Roux, D.; Coulon C.; Cates, M.E. Sponge phases in surfactant solutions. *J. Phys. Chem.* **1992**, *96*, 4174-4187.

53 Skouri, M.; Marignan, J.; Appel, J.; Porte, G. Fluid membranes in the "semi-rigid regime": scale invariance. *J. Phys. II* **1991**, *1*, 1121-1132.

54 Helfrich, W. Lyotropic lamellar phases. *J. Phys.: Condens. Matter* **1994**, *6*, A79-A92.

55 Helfrich, W. Elastic Properties of Lipid Bilayers—Theory and Possible Experiments. *Z. Naturforsch C.* **1973**, *28C*, 693-703

56 Würger, A. Bending Elasticity of Surfactant Films: The Role of the Hydrophobic Tails. *Phys Rev. Letter* **2000**, *85*,337-340.

57 Oostenbrink, C.; Villa, A.; Mark, A.E.; Van Gunsteren, W.F. A Biomolecular Force Field Based on the Free Enthalpy of Hydration and Solvation: The GROMOS Force-Field Parameter Sets 53A5 and 53A6. *J. Comput Chem* **2004**, *25*, 1656-1676.

58 Karlstrom, G. A new model for upper and lower critical solution temperatures in poly(ethylene oxide) solutions. *J. Phys. Chem*. **1985**, *89*, 4962-4964.

59 Olsson, U.; Wennerström, H. Globular and bicontinuous phases of nonionic surfactant films. *Adv.Colloid Interface Sci.* **1994**, *49*, 113-146.

60 Wennerström, H.; Lindman, B. Micelles. Physical chemistry of surfactant association. *Phys. Rep.* **1979**, *52*, 1–86.

61 Strey, R. Microemulsion microstructure and interfacial curvature. *Colloid Polym. Sci.* **1994**, *272*, 1005-1019.

62 Israelachvili, J.N. Intermolecular and surface forces. Academic Press: London, 2002.

63 Berret, J.F.; Roux, D.C.; Porte, G. J. Isotropic-to-nematic transition in wormlike micelles under shear. *Phys. II (France)* **1994**, *4*, 1261-1279.

64 Liu, C.; Pine, D.J. Shear-Induced Gelation and Fracture in Micellar Solutions. *Phys. Rev. Lett.* **1996**, *77*, 2121-2124.

65 Yamamoto, J.; Tanaka, H. Shear-Induced Sponge-to-Lamellar Transition in a Hyperswollen Lyotropic System. *Phys. Rev. Lett.* **1996**, *77*, 4390-4393.

66 Mahjoub, H.F.; Bourgaux, C.; Sergot, P.; Kléman, M. Evidence of a Sponge-to-Lamellar Phase Transition under Shear by X-Ray Scattering Experiments in a Couette Cell. *Phys. Rev. Lett.* **1998**, *81*, 2076-2079.

67 Diat, O.; Roux, D. Preparation of monodisperse multilayer vesicles of controlled size and high encapsulation ratio. *J. Phys. II (France)* **1993**, *3*, 9-14.

68 Yamamoto, J.; Tanaka, H. Shear Effects on Layer Undulation Fluctuations of a Hyperswollen Lamellar Phase. *Phys. Rev. Lett.* **1995**, *74*, 932-935.

69 Herle, V.; Kohlbrecher, J.; Pfister, B.; Fischer, P.; Windha, E. J. Alternating Vorticity Bands in a Solution of Wormlike Micelles. *Phys. Rev. Lett.* **2007**, *99*, 158302.

70 Waleffe, F. Three-Dimensional Coherent States in Plane Shear Flows. *Phys. Rev. Lett.* **1998**, *81*, 4140-4143.

71 Lillo, F.; Mantegna, R. N. Anomalous Spreading of Power-Law Quantum Wave Packets ??? *Phys. Rev. Lett.* **2000**, *84*, 1061-1065.

72 Le, T.D.; Olsson, U.; Mortensen, K.; Zipfel, J.; Richtering, W. Nonionic Amphiphilic Bilayer Structures under Shear. *Langmuir* **2001**, *17*, 999-1008.

73 Medronho, B.; Schmidt, C.; Olsson, U.; Miguel, M.G. Size Determination of Shear-Induced Multilamellar Vesicles by Rheo-NMR Spectroscopy. *Langmuir* **2010**, *26*, 1477-1481.

74 Weigel, R.; Läuger, J.; Richtering, W.; Lindner, P. Anisotropic small angle light and neutron scattering from a lyotropic lamellar phase under shear. *J. Phys. II* **1996**, *6*, 529-542.

75 Oliviero, C.; Coppola, L.; Gianferri, R.; Nicotera, I.; Olsson, U. Dynamic phase diagram and onion formation in the system $C_{10}E_3/D_2O$. *Colloids Surf. A* **2003**, *228*, 85-90.

76 Kosaka, Y.; Ito, M.; Kawabata, Y.; Kato, T. Lamellar-to-Onion Transition with Increasing Temperature under Shear Flow in a Nonionic Surfactant/Water System. *Langmuir* **2010**, *26*, 3835-3842.

77 Fischer, P. Time dependent flow in equimolar micellar solutions: transient behaviour of the shear stress and first normal stress difference in shear induced structures coupled with flow instabilities. *Rheol. Acta* **2000**, *39*, 234-240.

78 Wunenburger, A.S.; Colin, A.; Leng, J.; Arnéodo, A.; Roux D. Oscillating Viscosity in a Lyotropic Lamellar Phase under Shear Flow. *Phys. Rev. Lett.* **2001**, *86*, 1374-1377.

79 Meyer, C.; Asnacios, S.; Bourgaux, C.; Kleman, M. Effects of Shear on a Lyotropic Lamellar Phase Molecular Crystals and Liquid Crystals. *Mol. Cryst. Liq. Cryst.* **1999**, *332*, 531-538.

80 Lerouge, S.; Decruppe, J.-P.; Humbert, C. Shear Banding in a Micellar Solution under Transient Flow. *Phys. Rev. Lett.* **1998**, *81*, 5457-5460.

81 Bonn, D.; Meunier, J.; Greffier, O.; Al-Kahwaji, A.; Kellay, H. Bistability in non-Newtonian flow: Rheology of lyotropic liquid crystals. *Phys. Rev. E* **1998**, *58*, 2115-2118.

82 Wilkins, G.M.H.; Olmsted, P.D. Vorticity banding during the lamellar-to-onion transition in a lyotropic surfactant solution in shear flow. *Eur. Phys. J. E*, **2006**, *21*, 133-143.

83 Rehage, H.; Hoffmann, H. Viscoelastic surfactant solutions: model systems for rheological research. *Mol Phys.* **1991**, *74*, 933-973.

84 Fischer, P.; Rehage, H. Non-linear flow properties of viscoelastic surfactant solutions. *Rheol. Acta* **1997**, *36*, 13-27.

85 Xu, A.; Gonnella, G.; Lamura, A. Morphologies and flow patterns in quenching of lamellar systems with shear. *Physical Review E* **2006**, *74*, 011505.

86 Dhont, J.K.G.; Briels, W. J. Gradient and vorticity banding . *Rheol Acta* **2008**, *47*, 257-281.

87 Wheeler, E.K.; Fischer, P.; Fuller, G.G. Flow instabilities and shear induced phase transition in viscoelastic surfactant solutions. *J. Non- Newtonian Fluid Mech.* **1998**, *75*, 193-209.

88 Fischer, P.; Wheeler, E.K.; Fuller, G.G. Shear-banding structure orientated in the vorticity direction observed for equimolar micellar solution. *Rheol. Acta* **2002**, *41*, 35-44.

89 Herle, V.; Fischer, P.; Windhab, E.J. Stress driven shear bands and the effect of confinement on their structures - a rheological, flow visualization and rheo-SALS study. *Langmuir* **2005**, *21*, 9051-9057.

90 Roux, D.; Nallet, F.; Diat, O. Rheology of Lyotropic Lamellar Phases. *Europhys. Lett.* **1993**, *24*, 53-58.

91 Panizza, P.; Colin, A.; Coulon, C.; Roux, D. A dynamical study of onion phases under shear flow:size changes. *Eur. Phys. J. B* **1998**, *4*, 65-74.

92 Mahjoub, H.; McGrath, K.; Kléman, M. Phase Transition Induced by Shearing of a Sponge Phase. *Langmuir* **1996**, *12*, 3131-3138.

93 Britton, M.M.; Callaghan, P.T. Shear banding instability in wormlike micellar solutions. *Eur Phys J B* **1999**, *7*, 237-249.

94 Salmon, J-P.; Colin, A.; Manneville, S.; Molino, F. Velocity profiles in shear-banding worm-like micelles. *Phys Rev Lett* **2003**, *90*, 228303.

95 Herle, V.; Fischer, P.; Windhab, E.J. Stress driven shear bands and the effect of confinement on their structures—a rheological, flow visualization and rheo-SALS study. *Langmuir* **2005**, *21*, 9051-9057.

96 Hu, Y.T.; Lips, A. Kinetics and mechanism of shear banding in an entangled micellar solution. *J Rheol* **2005**, *49*, 1001-1027.

97 Liberato, M.W.; Nettesheim, F.; Wagner, N.J. Spatially resolved small-angle neutron scattering in the 1–2 plane: a study of shearinduced phase-separating wormlike micelles. *Phys Rev E* **2006**, *73*, 020504.

98 Yesilata, B.; Clasen, C.; McKinley, G.H. Nonlinear shear and extensional flow dynamics of wormlike surfactant solutions. *J Non-Newtonian Fluid Mech* **2006**, *133*, 73-90.

99 Miller, E.; Rothstein, J.P. Transient evolution of shear-banding wormlike micellar solutions. *J Non-Newtonian Fluid Mech* **2007**, *143*, 22-37.

100 Manneville, S.; Colin, A.; Waton, G.; Schosseler, F. Wall slip, shear banding, and instability in the flow of a triblock copolymer micellar solution. *Phys Rev E* **2007**, *75*, 061502.

101 Chen, L.B.; Zukoski, C.F.; Ackerson, B.J.; Hanley, H.J.M.; Straty, G.C.; Barker, J.; Glinka, C.J. Structural changes and orientational order in a sheared colloidal suspension. *Phys Rev Lett* **1992**, *69*, 688-691.

102 Dhont, J.K.G.; Briels, W.J. Viscoelasticity of suspensions of long, rigid rods. *Coll Surf A Physicochem Eng Aspects* **2003**, *213*, 131-156.

103 Kang, K.; Lettinga, M.P.; Dogic, Z.; Dhont, J.K.G. Vorticity banding in rodlike virus suspensions. *Phys Rev E* **2006**, *74*, 026307.

104 Lin-Gibson, S.; Pathak, J.A.; Grulke, E.A.; Wang, H.; Hobbie, E.K. Elastic flow instability in nanotube suspensions. *Phys Rev Lett* **2004**, *92*, 048302.

105 Bonn, D.; Meunier, J.; Greffier, O.; Al-Kahwaji, A.; Kellay, H. Bistability in non-Newtonian flow: rheology and lyotropic liquid crystals. *Phys Rev E* **1998**, *58*, 2115-2118.

106 Mitchell, D.J.; Tiddy, G.J.T.; A.N.D.; Waring, L.; Bostock, T.; Mcdonald, M.P. Phase behaviour of polyoxyethylene surfactants with water. Mesophase structures and partial miscibility (cloud points). *J.Chem. SOC., Faraday Trans. I* **1983**, *79*, 975-1000.

107 Laughlin, R.G. in Micelles, Microemulsions and Monolayer: Science and Technology. CRC Press: New York, 1998.

108 Ali, A.; Mulley, B.A. Formation of liquid crystal and other non-fluid phases in emulsions containing non-ionic surfactants . *J. Pharm. Pharmacol.* **1978**, *30*, 205-213.

109 Schambil, F.; Schwuger, M.J. CPS LG 315 Correlation between the phase behavior of ternary systems and removal of oil in the washing process. *Colloid Polym. Sci.* **1987**, *265*, 1009-1017.

110 Jonströmer, M.; Strey, R. Nonionic bilayers in dilute solutions: effect of additives. *J. Phys. Chem.* **1992**, *96*, 5993-6000.

111 Porte, G.; Appell, J.; Bassereau, P.; Marignan, J. Lα to L3 : a topology driven transition in phases of infinite fluid membranes. *J. Phys. (Paris)* **1989**, *50*, 1335-1347.

112 Anderson, D.; Wennerstrom, H.; Olsson, U. Isotropic bicontinuous solutions in surfactant-Solvent systems: the L3 phase. *J. Phys. Chem.* **1989**, *93*, 4243-4253.

113 Fontell, K.; Mandell, L.; Lehtinen, H.; Ekwall, P. 3-component system sodium caprylate-decanol-water.3.Structure of mesophases at 20 degrees C. *Acta Polytech. Scand. Chem. Metall. Ser.* **1968**, *74*, 1-14.

114 Stubenrauch, C.; Burauer, S.; Strey, R.; Schmidt, C. A new approach to lamellar phases (Lα) in water - non-ionic surfactant systems *Liq. Cryst.* **2004**, *31*, 39-53.

115 Strey, R.; Schomäcker, R.; Roux, D.; Nallet, F.; Olsson, U. Dilute Lamellar and L3-Phases in the Binary Water-$C_{12}E_5$ System. *J. Chem. Soc. Faraday T.* **1990**, *86*, 2253-2261.

116 Tlusty, T.; Safran, S.A. Entropic networks in colloidal self-assembly. *Philos.Trans. R. Soc. London, Ser. A* **2001**, *359*, 879-881.

117 Magid, L. l Structure and Dynamics by SmallAngle Neutron Scattering in Nonionic Surfactants Schick, M. l, Ed.; Marcel Dekker: New York, 1987.

118 Tiddy, G.J.T.; Rendall, K.; Galsworthy, P. Lyotropic Mesophase Behaviour of n-C16H33EO3 - Evidence for Two “V2” Phases. *Mol. Cryst. Liq. Cryst.* **1982**, *72*, 147-152.

119 Key, B.D.; Howell, R.D.; Criddle, C.S. Fluorinated organics in the biosphere. *Environ. Sci. Technol.* **1997**, *31*, 2445-2454.

120 Kissa, E. Fluorinated Surfactants: Synthesis, Properties, and Applications. Marcel Dekker: New York, 1994.

121 Porter, M.R. Handbook of Surfactants, 2nd ed.; Blackie Academic & Professional: London, 1994

122 Chidichimo, G.; Coppola, L.; La Mesa, C.; Ranieri, G.A.; Saupe, A. Structure of the lamellar lyo-mesophase in water/ammonium perfluorononanoate mixtures: PFG NMR and 2H-NMR investigations. *Chem. Phys. Lett.* **1988**, *145*, 85-89.

123 Angelico, R.; Ceglie, A.; Olsson, U.; Palazzo, G. Phase Diagram and Phase Properties of the System Lecithin−Water−Cyclohexane. *Langmuir* **2000**, *16*, 2124-2132.

124 Lindman, B.; Wennerströem, H. Nonionic micelles grow with increasing temperature. *J. Phys. Chem.* **1991**, *95*, 6053-6054.

125 Ravey, J.C. Lower consolute curve related to micellar structure of nonionic surfactants. *J. Coll. Interface Sci.* **1983**, *94*, 289-291.

126 Carale, T.R.; Blankschtein, D. Theoretical and experimental determinations of the crossover from dilute to semidilute regimes of micellar solutions. *J. Phys. Chem.* **1992**, *96*, 459-467.

127 Ferry, D.J. Viscoelastic Properties of Polymers. Wiley: New York, 1980.

128 Olafsen, J. Experimental and Computational Techniques in Soft Condensed Matter Physics. Cambridge University Press: Cambridge, 2010.

129 Maxwell, J.C. On the Dynamical Theory of Gases. *Phil. Trans. R. Soc., London* **1867**, *157*, 49-88.

130 Macosko, C.W. Rheology: Principles, Measurments, and Applications.Wiley-VCH: New York, 1994.

131 Chaikin, P.M.; Lubensky, T.C. Principles of Condensed Matter Physics. Cambridge University Press: Cambridge, 1995.

132 Chhabra, R.P.; Richardson, J.F. Non-Newtonian flow and applied rheology: engineering applications. Elsevier: Oxford, 2008.

133 Larson, R.G. Instabilities in viscoelastic flows. *Rheol. Acta* **1992**, *31*, 213-263.

134 Møller, P.C.F.; Rodts, S.; Michels, M.A. J.; Bonn, D. Shear banding and yield stress in soft glassy materials. *Phys. Rev. E* **2008**, *77*, 041507.

135 Tabuteau, H.; de Bruyn, J.R.; Coussot, P. Drag force on a sphere in steady motion through a yield-stress fluid. *J. Rheol.* **2007**, *51*, 125-137.

136 Yoshimura, A.; Prud'homme, R.K. Wall slip corrections for Couette and parallel disk viscometers. *J. Rheol.* **1988**, *32*, 53-67.

137 Taylor, G.I. Stability of a Viscous Liquid Contained Between Two Rotating Cylinders. *Philos. Trans. Roy. Soc. London A* **1923**, *223*, 289-343.

138 Taylor, G.I. Statistical Theory of Turbulence. V. Effect of turbulence on boundary layer. *Proc Roy Soc London A* **1936**, *156*, 307-317.

139 Mezger, T.G. The Rheology Handbook. Vincentz Network: Hannover, 2006.

140 Reynolds, O. An experimental investigation of the circumstances which determine whether the motion of water shall be direct or sinuous. *Proc Roy Soc London A* **1883**, *93*, 148-154.

141 Reynolds, O. The sub-mechanics of the universe. Cambridge university press: London, 1903.

142 Abragam, A. Principles of nuclear magnetism. Clarendon: Oxford, 1961.

143 Levitt, M.H. Spin dynamics: basics of nuclear magnetic resonance. Wiley: New York, 2008.

144 Saitô, H.; Ando, I.; Naito A. Solid state NMR spectroscopy for biopolymers: principles and applications. Springer: Dordrecht, 2006.

145 Douliez, J.P.; Bellocq, A.M.; Dufourc, E.J. Effect of vesicle size, polydispersity andmultilayering on solid state 31P- and 2H-NMR spectra. *J. Chim. Phys. Phys.-Chim. Biol.* **1994**, *91*, 874-880.

146 Auguste, F.; Douliez, J.-P.; Bellocq, A.-M.; Dufourc, E. J.; Gulik-Krzywicki, T. Evidence formultilamellar vesicles in the lamellar phase of an electrostatic lyotropic ternary system. A solid state 2H-NMR and freeze fracture electron microscopy study. *Langmuir* **1997**, *13*, 666-672.

147 Baciu, M.; Olsson, U.; Leaver, M.S.; Holmes, M.C. ^{2}HNMR evidence for the formation of random mesh phases in nonionic surfactant-water systems. *J. Phys. Chem. B* **2006**, *110*, 8184-8187.

148 Gotter, M.; Strey, R.; Olsson, U.; Wennerstr€om, H. Fusion and fission of fluid amphiphilic bilayers. *Faraday Discuss.* **2005**, *129*, 327-338.

149 Wennerström, H.; Lindblom, G.; Lindman, B. Theoretical aspects on the NMR of quadrupolar ionic nuclei in micellar solutions and amphiphilic liquid crystals. *Chem. Scr.* **1974**, *6*, 97-103.

150 Wennerström, H.; Lindman, B.; Soderman, O.; Drakenberg, T.; Rosenholm, J. B. Carbon-13 magnetic relaxation in micellar solutions. Influence of aggregate motion on T1. *J. Am. Chem. Soc.* **1979**, *101*, 6860-6864.

151 Halle, B.; Wennerstrom, H. Chemiemission from the cesium-oxygen surface reaction. *J. Chem. Phys.* **1981**, *75*, 1928-1936.

152 Klein, F.; Sommerfeld, A. Uber die Theorie des Kreisels. Teubner: Leipzig, 1910.

153 Kimmich, R. NMR Tomography, Diffusometry, Relaxometry. Springer: Berlin, 1997.

154 Emst, R.R.; Bodenhausen, G.; Wokaun, A. Principles of Nuclear Magnetic Resonance in One and Two Dimensions. Clarendon Press: Oxford, 1987.

155 Slichter, C.P. Principles of Magnetic Resonance, 3rd enlarged edn. Springer: Berlin, 1989.

156 Kumar, A.; Welti, D.; Ernst, R.R. NMR Fourier Zeugmatography. *J. Magn. Reson.* **1975**, *18*, 69-83.

157 Mansfield, P.; Grannell, R.K. "Diffraction" and microscopy in solids and liquids by NMR. *Phys. Rev B* **1975**, *12*, 3618-3634.

158 Callaghan, P.T. Principles of Nuclear Magnetic Resonance Microscopy. Clarendon Press: Oxford, 1991.

159 Caprihan, A.; Fukushima, E. Flow measurements by NMR. *Physics Reports* **1990**, *4*, 195-235.

160 Ljunggren, S. A simple graphical representation of Fourier- based imaging methods. *J. Magn. Reson.* **1983**, *54*, 338-343.

161 Mansfield, R; Grannell, P.K. NMR Diffraction in Solids. *J. Phys, C* **1973**, *6*, L422.

162 Callaghan, P.T. Pulsed Field Gradient Nuclear Magnetic Resonance as a Probe of Liquid State Molecular Organization. *Aust. J. Phys.* **1984**, *37*, 359-388.

163 Karczmar, G.S.; Twieg, D.B.; Lawry, T.J.; Matson, G.B.; Wiener, M.W. Detection of motion using B1 gradients. *Magn. Reson. Med* **1988**, *7*, 111-116.

164 Lindner, P. and Zemb, T. (eds.), Neutrons, X-rays and Light: Scattering Methods Applied to Soft Condensed Matter. Elsevier: Amsterdam, 2002.

165 Rawiso, M.; Duplessix, R.; Picot C. Scattering function of polystyrene. *Macromolecules* **1987**, *20*, 630-648.

166 Läuger, J.; Heyer, P. Rheo Small Angle Light Scattering (Rheo-SALS) and Rheo-Microscopy as tools for investigations of structure-property relations in complex fluids. *Ann. Trans. Nordic Rheology Society* **2006**, *14*, 193-196.

167 Läuger, J.; Heyer, P.; Pfeifer G. A new investigated Rheo Small Angle Light Scattering (Rheo-SALS) device. *Ann. Trans. Nordic Rheology Society* **2004**, *12*, 137-140.

168 Samuels, R.J. Small-angle light scattering from optically anisotropic spheres and disks. Theory and experimental verification. *J. Polym. Sci. Part A-2* **1971**, *9*, 2165-2246.

169 Stein, R.S.; Wilkes, G.L. Phisico-chemical approaches to the measurement of anisotropy. In Sructure and properties of oriented Polymers. Chapman & Hall: London, 1975.

170 Berghausen, J.; Zipfel, J.; Lindner, P.; Richtering, W. Shear-induced orientations in a lyotropic defective lamellar phase. *Europhys. Lett.* **1998**, *43*, 683-689.

171 Müller, S.; Börschig, C.; Gronski, W.; Schmidt, C. Shear-Induced States of Orientation of the Lamellar Phase of $C_{12}E_4$/Water. *Langmuir* **1999**, *15*, 7558-7564.

172 Gulik-krzywicki, T.; Dedieu, J.C.; Roux, D.; Deggert, C.; Laversanne, R. Freeze−Fracture Electron Microscopy of Sheared Lamellar Phase. *Langmuir* **1996**, *12*, 4668-4671.

173 Fujii, S.; Richtering, W. Size and viscoelasticity of spatially confined multilamellar vesicles. *Eur. Phys. J. E* **2006**, *19*, 139-148.

174 Lu, C.-Y. D.; Chen, P.; Ishii, Y.; Komura, S.; Kato T. Non-linear rheology of lamellar liquid crystals *Eur. Phys. J. E* **2008**, *25*, 91-101.

175 Medronho, B.; Rodrigues, M.; Miguel, M.G.; Olsson, U.; Schmidt, C. Shear-Induced Defect Formation in a Nonionic Lamellar Phase. *Langmuir* **2010**, *26*, 11304-11313.

176 Medronho, B.; Miguel, M.G.; Olsson, U. Viscoelasticity of a Nonionic Lamellar Phase. *Langmuir* **2007**, *23*, 5270-5274.

177 Filippelli, L.; Medronho, B.; Oliviero Rossi, C.; Miguel, M.G.; Olsson, U. Metastability of Multi-Lamellar Vesicles in a Nonionic System. *Mol. Cryst. & Liq. Cryst.* **2009**, *500*, 166-181.

178 Panizza, P.; Roux, D.; Vuillaume, V.; Lu, C.-Y.D.; Cates, M.E. Viscoelasticity of the Onion Phase. *Langmuir* **1996**, *12*, 248-252.

179 Roshan Deen, G.; Pedersen, J.S. Phase Behavior and Microstructure of $C_{12}E_5$ Nonionic Microemulsions with Chlorinated Oils. *Langmuir* **2008**, *24*, 3111-3117.

180 Penfold, J.; Staples, E.; Khan Lodhi, A.; Tucker, I.; Tiddy, G.J.T. Shear-Induced Transformations in the Lamellar Phase of Hexaethylene Glycol Monohexadecyl Ether. *J. Phys. Chem. B* **1997**, *101*, 66-72.

181 Suganuma, Y.; Imai, M.; Kato, T.; Olsson, U.; Takahashi, T. Order−Disorder Transition of Nonionic Onions under Shear Flow. *Langmuir* **2010**, *26*, 7988-7995.

182 Silva, B.F.B.; Marques, E.F.; Olsson, U. Aqueous phase behavior of salt-free catanionic surfactants: the influence of solubility mismatch on spontaneous curvature and balance of forces. *Soft Matter* **2011**, *7*, 225-236.

183 Noro, M. G.; Gelbart, W. M. Theory of lamellar–lamellar phase transitions in pure and mixed surfactant solutions. *J. Chem. Phys.* **1999**, *111*, 3733-3743.

184 Dubois, M.; Zemb, Th.; Fuller, N.; Rand, R.P.; Parsegian, V.A. Equation of state of a charged bilayer system: Measure of the entropy of the lamellar–lamellar transition in DDABr. *J. Chem. Phys.* **1998**, *108*, 7855-7869.

185 Iwashita, Y.; Tanaka H. Self-organization in phase separation of a lyotropic liquid crystal into cellular, network and droplet morphologies. *Nature Materials* **2006**, *5*, 147-152.

186 Partal, P.; Kowalski, A.J.; Machin, D.; Kiratzis, N.; Berni, M.G.; Lawrence, C.J. Rheology and Microstructural Transitions in the Lamellar Phase of a Cationic Surfactant. *Langmuir* **2001**, *17*, 1331-1337.

187 Koschoreck, S.; Fujii, S.; Lindner, P.; Richtering, W. Multilamellar vesicles ("onions") under shear quench: pathway of discontinuous size growth. *Rheologica Acta* **2009**, *48*, 231-240.

188 Coppola, L.; Nicotera, I.; Oliviero, C.; Ranieri, G.A. Indirect detection of structural changes on the pluronic Pe 6200/H2O system by rheological measurements. *Colloids and Surfaces A: Physicochem. Eng. Aspects* **2004**, *245*, 183–192.

189 Shahidzadeh, N.; Bonn, D.; Aguerre-Chariol, O.; Meunier, J. Large Deformations of Giant Floppy Vesicles in Shear Flow. *Phys. Rev. Lett.* **1998**, *81*, 4268-4271.

190 Lukaschek, M.; Müller; Hasennindl, A.; Schmidt, C.; Grabowski, D.A. Lamellar lyomesophases under shear as studied by deuterium nuclear magnetic resonance. *Colloid & Polymer Science* **1996**, *274*, 1-7.

191 Lutti, A.; Callaghan, P.T. Measurement of multilamellar onion dimensions under shear using frequency domain pulsed gradient NMR. *J. of Magn. Reson.* **2007**, *187*, 251-257.

192 Buhler, E.; Mendes, E.; Boltenhagen, P.; Munch, J. P.; Zana, R.; Candau, S. J. Phase Behavior of Aqueous Solutions of a Dimeric Surfactant. *Langmuir* **1997**, *13*, 3096-3102.

193 Fairhurst, C.E.; Holmes, M.C.; Leaver, M.S. Structure and Morphology of the Intermediate Phase Region in the Nonionic Surfactant $C_{16}EO_6$/Water System. *Langmuir* **1997**, *13*, 4964-4975.

194 Holmes, M.C.; Leaver, M.S.; Smith, A.M. Nematic and Disrupted Lamellar Phases in Cesium Pentadecafluorooctanoate/^2H_2O: A Small Angle Scattering Study. *Langmuir* **1995**, *11*, 356-365.

195 Spenley, N.A.; Cates, M.E.; McLeish, T.C.B. Nonlinear rheology of wormlike micelles. *Phys. Rev. Lett*. **1993**, *71*, 939-942.

196 Angelico, R.; Olsson, U.; Mortensen, K.; Ambrosone, L.; Palazzo, G.; Ceglie, A. Relaxation of Shear-Aligned Wormlike Micelles. *J. Phys. Chem. B* **2002**, *106*, 2426-2428.

197 Dhez, O.; Nallet, F.; Diat, O. Influence of screw dislocations on the orientation of a sheared lamellar phase. *Europhys. Lett.* **2001**, *55*, 821-826.

198 Kurtisovski, E.; Taulier, N.; Ober, R.; Waks, M.; Urbach, W. Molecular Origin of Model Membrane Bending Rigidity. *Phys. Rev. Lett.* **2007**, *98*, 258103.

DIN 53018/1976. Measurement of the Dynamic Viscosity of Newtonian Fluids with Rotational Viscometers.

DIN 53019/2008. Measurement of Viscosities and Flow Curves by means of Rotational Viscometers.

ISO 3219/1993. Plastics, Polymers/resins in the liquid state or as emulsions or dispersions -- Determination of viscosity using a rotational viscometer with defined shear rate.

I

Rheological and rheo-SALS investigation of the multi-lamellar vesicle formation in the $C_{12}E_3/D_2O$ system

L. Gentile, C. Oliviero Rossi and U. Olsson

Journal of Colloid Interface Science

http://dx.doi.org/10.1016/j.jcis.2011.10.057

II

Effect of Shear Rates on the MLV Formation and MLV Stability Region in the $C_{12}E_5/D_2O$ System: Rheology and Rheo-NMR and Rheo-SANS Experiments

L. Gentile, C. Oliviero Rossi, U. Olsson and G.A. Ranieri

Langmuir

http://dx.doi.org/10.1021/la1046047

III

Multi-lamellar vesicle formation in a long-chain nonionic surfactant: $C_{16}E_4/D_2O$ system

L. Gentile, K. Mortensen, C. Oliviero Rossi, U. Olsson and G.A. Ranieri

Journal of Colloid Interface Science

http://dx.doi.org/10.1016/j.jcis.2011.06.053

IV

Structural Transitions Induced by Shear Flow and Temperature variation in a Nonionic Surfactant/Water System

L. Gentile, B.F.B. Silva, S. Balog, K. Mortensen and U. Olsson

Submitted to Journal of Colloid Interface Science

V

Evidence of Formation of Ammonium Perfluorononanoate/^2H_2O Multilamellar Vesicles: Morphological Analysis by Rheology and Rheo-^2H NMR Experiments

L. Coppola, L. Gentile, I. Nicotera, C. Oliviero Rossi and G.A. Ranieri

Langmuir

http://dx.doi.org/10.1021/la102887e